An analytical and experimental study on 3D-printed custom surfaces for benthic algal biofilms

by

Kamran Kardel

A dissertation submitted to the Graduate Faculty of
Auburn University
in partial fulfillment of the
requirements for the Degree of
Doctor of Philosophy

Auburn, Alabama
August 6, 2016

Keywords: Additive Manufacturing, Benthic Algae, Surface Topography, 3D printing, Collision

Approved by

Andres L. Carrano, Chair, Associate Professor of Industrial and Systems Engineering
David M. Blersch, Assistant Professor of Biosystems Engineering
Jeffrey S. Smith, Professor of Industrial and Systems Engineering
Dan B. Marghitu, Professor of Mechanical Engineering

Abstract

Due to their fast growing rates and regeneration, algae are a promising avenue for biofuels, aquatic pollution recovery, and a source of protein nutrients, among others. Cultivation of benthic algal communities, in particular, show promise for these functions, yet control quality and yield is strongly dependent on substrata characteristics that affect algal attachment and growth. No previous research efforts seem to have taken advantage of the recent developments in additive technology to support algal attachment and colonization. Additive manufacturing can allow for the design and control of surface features and provide a platform for developing substrata with customized surface topographies for algal colonization. This study seeks to, first, establish the feasibility of colonizing 3D-printed custom substrata with algal biomass. Then, using 3D printing, potential approaches of controlling species composition in cultivation systems through design of substratum characteristics to select for species in colonization were investigated. It was done by designing and 3D printing substratum topographic sections to test for selectivity of colonization of periphyton algae in natural streams. In another effort, relationship between surface topographic features with attachment and colonization of benthic algal species were studied. 3D-printed pattern s were used as molds for making growth plates with clay. The clay-made plates were then placed in a laboratory-based bench scale bio-cultivator exposed to a culture of benthic algae for three weeks for each replicate for a total three replicates. After collection, the biomass was carefully harvested in each section and oven dried and then weighed to find the exact amount of algae biomass per each section. Finally, the performance of 3D-printed materials (polymers) in such custom surfaces under collisions was characterized to better design for different applications.

Based on the results, the preliminary work seems to indicate that: (*i*) 3D printed substrata can be successfully colonized by algal communities; (*ii*) there is a roughness effect on the colonization rate of benthic algae; (*iii*) substratum roughness can be designed for optimal interstitial spacing between surface asperities, and (*iv*) increased efficiencies in the packing of biomass can be achieved by complex 3D-printed geometries that provide very high surface area in compact volumes. Also, in research on preferences of algal species from natural streams, twelve species of periphyton algae in four divisions were identified across all topographic sections, and the distribution of these twelve species and relative abundance varied as a function of topographic feature size, with the greatest diversity observed on the surfaces with topographic feature sizes of 500 μm. Of the twelve identified species, two showed abundance patterns as a function of topographic feature size that were significant. *Microspora wileana* displayed a preference for surfaces with topographic feature sizes less than 500 μm, and *Stigeoclonium tenue* displayed a preference for surfaces with topographic feature sizes less than or equal to 100 μm and greater than or equal to 1500 μm. These results suggest that substratum design using 3D printing or other technologies may be useful to influence species composition and dominance relationships in mixed communities in engineered periphyton cultivation systems.

The behavior of five different 3D-printed polymers have been analyzed theoretically and experimentally under low speed collision. Impact of a rigid rod on a flat made of 3D-printed materials has been analyzed. An experimental setup has been designed in order to capture the motion of the rod during the impact using a high speed camera. Image processing is developed to estimate the velocity before and after the impact as well as coefficient of restitution. Permanent deformations after the impact have been scanned with an optical profilometer. A theoretical formulation for the contact force during the impact has been proposed. The impact has been

divided into two phases: compression and restitution. For the compression phase the materials considered elasticplastic and the restitution phase has been considered to be fully elastic. The experimental results have been used to measure the damping coefficient. Results indicate that the proposed formulation for the contact force matches the materials behavior.

Acknowledgments

I would like to acknowledge everyone who assisted me throughout my doctoral studies over the years. First and foremost, I like to thank and dedicate all my success to my lovely wife. Her everyday love, support and encouragement was what made my doctoral studies and this dissertation possible.

I would like to acknowledge my advisor, Dr. Andres Carrano for his enthusiastic support and guidance which made my doctoral studies a very rewarding experience. Also, my great appreciation is expressed to Dr. David Blersch for his support and great advice during my studies. Many thanks to Ms. Manjinder Kaur, Mr. Ali Khoshkhoo, Mr. Gabriel Proano, and Mr. Joseph Ekong of Auburn University for helping with the experiments. My special thanks are due to Mr. Hamid Ghaednia, my friend and partner in impact experiments, for all his help and support. Also, I should express many thanks to Dr. Dan Maghitu for offering his impact lab for experiments and his advice. My dissertation committee members for all of their guidance through the process.

Appreciation is expressed to Dr. Gary Wagoner of Auburn University's Art Department for providing the clay plates. Many thanks are due to Dr. Brian Thorn of the Rochester Institute of Technology for great help in statistical designs.

Last but not least, I like to thank my caring parents for their continuous support and inspiration. My brothers for their everyday encouragement and help. Many thanks are expressed to my parents-in-law for their unhesitating support.

Table of Contents

List of Tables

List of Figures

1. Introduction

Additive Manufacturing (AM) or 3D printing technologies are mostly associated with applications in product design and development and small batch manufacturing. Due to the ability to produce complex geometries at relatively high speeds, AM technologies are increasingly being employed in various non-manufacturing applications. Applications in domains such as tissue engineering and osteopathy have been actively researched in recent years[1]. The extension of AM into environmental engineering applications has been very limited, however, despite many potential applications involving mass transfer and biological growth processes that are mediated by spatial and topological relationships. A primary environmental application that might be suitable for AM technologies is the manufacture of designer surface topographies for phototrophic biofilm production.

Algae are heterogeneous assemblage of organisms that size from single cells to large sea weeds and belong to diverse evolutionary lineage[2] (Figure 1). Periphytic biofilms are composed of benthic algae and bacteria that attach to solid substrata surfaces in a flow environment[3]. Naturally occurring in all fresh and marine water flow environments, phototrophic biofilms have been investigated under controlled cultivation scenarios for various environmental engineering applications. Benthic algal biofilm cultivation has been investigated for aquatic pollution recovery from natural waters and wastewaters, water quality improvements in natural waters and groundwaters, as well as biomass production for various economic uses including protein production and biofuels feedstocks[4–7] . Bioreactors can be engineered and designed based for water treatments using benthic (filamentous) algae and planktonic (suspended) algae (figure 2).

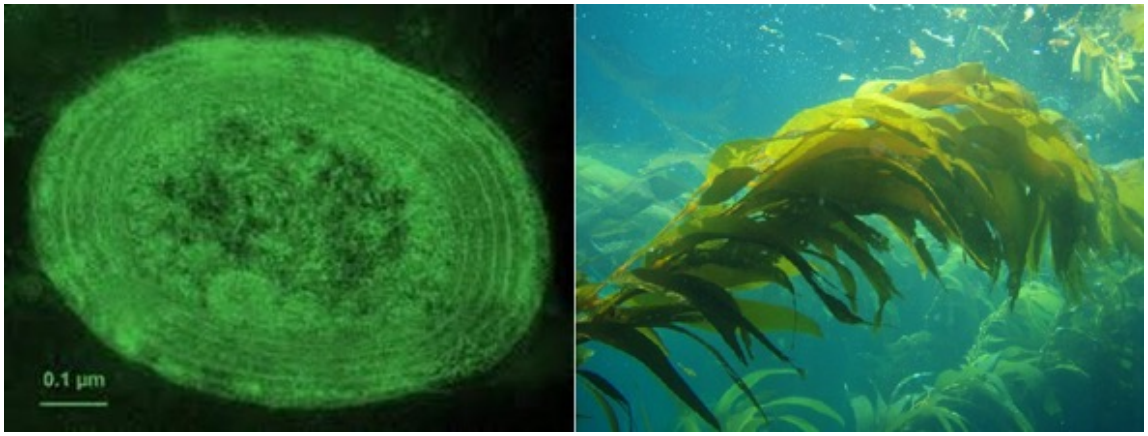

(a) **(b)**

Figure 1. Different sizes of algal species: (a) *Chlorella* and (b) Sea weed (Giant kelp)[8]

At-scale applications are typically open systems subject to mixed algal communities, and the types and abundance of various attached algal species that colonize a particular surface substratum determines, to a degree, the overall yield of the particular biotic process or product of interest. Control of the colonization and growth process through operational parameters such as substratum topography (e.g. feature and texture design) can be an important determinant to overall system performance.

(a) **(b)**

Figure 2. Acres of bioreactors based on (a) filamentous benthic algae[9] **and (b) planktonic (suspended) algae**[10] **for water treatments**

In natural flow environments such as streams, the topographical characteristics of the substratum can be a controlling factor in the development of a colonizing biofilm[2]. Heterogeneity of the substratum morphology determines the flow turbulence characteristics within the fluid boundary layer, affecting the kinetics of cell colonization, growth, and metabolism. Boundary layer flow characteristics also affect advection and diffusion of limiting nutrients to colonizing biofilms, which can strongly influence growth kinetics. Therefore, it is hypothesized that manipulation of the substratum topography characteristics can be used to control the structural and functional characteristics of the colonizing algal biofilm.

To date, no research effort has taken advantage of using custom designed 3D-printed surface to investigate the attachment preferences of certain periphyton species towards substrata topography. This work intends to prove feasibility of the idea of using 3D-printed surface topographies to support biofilm growth. It also intends to lay the foundational work to establish initial relationships between surface topography and species diversity and biomass. Finally, it intends to characterize the performance of 3D-printed materials in such custom surfaces under collisions that might occur in natural environments.

2. Literature Review

There has been much interest in controlled cultivation of periphyton for various applications in aquatic pollutant recovery and biomass production[6,11–14]. Periphyton comprises mixed microbial communities dominated by algae that grow while attached to a surface or substratum in a fluid environment, typically occurring in shallow aquatic environments where light and water flow are available[15]. While the advantages of periphyton cultivation for aquatic pollutant recovery stem from the ease of operation and biomass recovery, the open configuration of cultivation typically found at the large scale leaves the community subject to competitive pressures among the indigenous species of the local water source, affecting the quality of the resulting biomass for downstream economic use[16,17]. Approaches for controlling species selection in colonization and competitions are desirable for ultimate economic use of periphytic biomass.

In-situ studies in streams and laboratory investigations have shown that the ecological characteristics of a colonizing algal biofilm can be influenced by the physical and chemical characteristics of the substratum[2]. Physically, the heterogeneity of roughness characteristics of a substratum affects the colonization, attachment, and growth characteristics of viable microbial spores or cells that act as seed colonizers for biofilm establishment[18–20]. Typically, the mechanisms of substratum control over the biofilm characteristics have been investigated only at the macroscopic level for the design of reactors around a process or function, employing a uniform substratum characteristic across an entire reactor bed[17].

Because of boundary layer effects, substratum surface topographic texture affects the rate of retention of microorganisms on that surface. However, this effect appeared to be observed only for certain roughness feature dimensions. If features are considerably larger than the microbial cells, then cell retention is not significant, whereas if features are on the order of microbial dimensions, then cell retention can increase[21]. Also, a set of topographical parameters has been proposed as a

standard for surface roughness characterization in bacterial adhesion studies to improve the likelihood of identifying direct relationships between substratum topography and bacterial adhesion[22]. These proposed parameters are root mean square surface roughness (S_q), summit density (S_{ds}), developed area ratio (S_{dr}), the ten-point average roughness (S_z), skewness (S_{sk}), texture aspect ratio (S_{tr}), and bearing ratio (t_p) and using them should enable more accurate prediction of bacterial cell adhesion. It has also been shown that smooth substrata are the least favorable for propagule settlement, and that increased settlement on substrata would occur if surface relief were increased up to an optimum roughness with an average depression depth of 800 µm[23].

While it is generally acknowledged that an increased substratum surface roughness affects the retention of microorganisms on that surface, this premise is only valid for certain feature dimensions. If the features are considerably larger than the microbial cells, then retention is not significant and if the features are of microbial dimensions, then retention may become a problem[21]. With regards to benthic algae, the influence of physical substrata features encompasses a long-standing topic of research. It was found that substrata topographies with netlike or weblike configuration reduce local fluid velocities and enable high rates of algal cell settling and attachment[24]. Similarly, substrata with heterogeneous surface microrelief, such as microcrevices in rock, provide depressions where velocities are low and spores can settle[18,19]. Definitive experimental research focusing on the spores of marine macroalgae has demonstrated the importance of microtopography in algal settlement and germination[23,25,26]. It was concluded that interstitial space may be the most important factor regulating algal population on proposed substrata.

Recent research efforts to design surfaces for algal and single-cell/spore attachment have been pursued, and various methods have been employed to produce designed surfaces. Settlement and adhesion of zoospores from the green algae *Ulva linza* were investigated within defined topographies[27]. In this research, four topographic size scales (R_z peak-to-valley varying between 25-100 μm) were manufactured by molding a plankton net between two PMMA microscope slides in a press while applying heat. The topographic scales produce a texture similar to that of natural substrata and antifouling coatings. Spores then were removed from the surfaces by a calibrated water jet. It was found that fewer spores were removed from the smallest topographic structure tested (R_z: 25 μm) than from the larger ones. Also, zoospores that settled in hollows were less likely to be removed compared to spores on the ridges. Other efforts showed that algae growth on a textured surface is several times higher than that on a smooth surface[28].

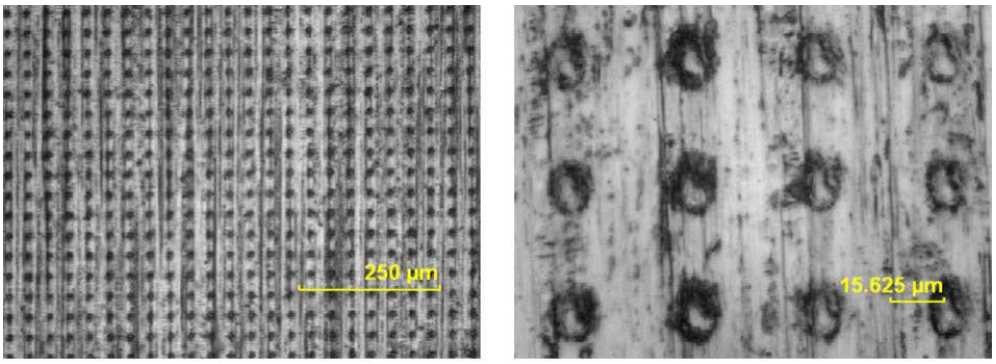

(a) **(b)**

Figure 3: Sample laser textured surface[28]

The surface texturing was accomplished by a Nd:YVO_4 laser which created dimple features of 6-8 μm in diameter, 2-3 μm in depth and spaced every 40 μm on stainless steel. Research work has also been pursued to investigate the effects of surface roughness and shear on the attachment of *Oscillatoria* sp. algal filaments onto stainless steel coupons in a spinning cylindrical environment[29]. The surfaces in this study were manufactured with traditional abrasive processes.

Six coupons with average roughness (Ra) increasing from 0.801 µm to 1.309 µm were utilized. It was found that the amount of algae strands deposited in the coupons increased with the average roughness. More recently, the impact of surface texture on microalgal cell attachment to solid nylon and polycarbonate carriers with ridges, pillars and groove features was investigated[30]. These features and textures were produced with laser and micro-milling methods. It was found that, for smooth surfaces, nylon had a better attachment than polycarbonate for algal species used in their research. Also, it was mentioned that attachment of algal cells to textured surfaces was strongly related to the size of cells and the surface features. Their results showed that, generally, groove had a better attachment than ridges and pillars for algal species in their research. It was also found that, algal cells could fully penetrate in to the designed textures, but the adhesion behavior would be dependent on the size and shape of the cell. It was also mentioned that larger and smaller feature dimensions had the potential to reduce cellular attachment.

Mechanical properties of rapidly evolving 3D-printed polymers are, to some extent, limited and would be outdated quickly. There are several, simultaneously, important properties of 3D-printed polymers which has been worked on many times. But, in this effort, dynamic behavior of these materials used in AM during collision with a rigid body has been studied.

There are many research efforts on testing 3D-printed plastics in terms of mechanical properties[31–35]. Tensile strength of 3D-printed polylactic acid (PLA) bars for bone fixation and reconstruction were tested[36]. Test bars were fabricated from low and high molecular weight PLA powders with chloroform used as a binder. The maximum tensile strength measured for high molecular weight PLA was reported 15.94 ±1.50 MPa and for low molecular weight was 17.40 ±0.71 MPa. More recently, research on the influence of print density on microstructure and mechanical properties of nylon parts in High Speed Sintering (HSS) showed that mechanical properties are related to

crystallinity[37]. Results showed that crystallinity decreased as print density increased. This was reflected by mechanical properties which showed stiffness and tensile strength increased with crystallinity. Acrylonitrile butadiene styrene (ABS) parts fabricated by Stratasys Fused Deposition Modeling (FDM) machine were also studied to measure and compare tensile and compressive strengths[38]. It was found that, for FDM parts made with 0.003 inch overlap between roads, tensile strength ranged between 65-72% of the strength of identical parts made with injection molded ABS. In other efforts, mechanical properties, surface roughness, geometric and dimensional accuracy, and material costs of various kinds of additive manufactured materials with different types of 3D printing machines such as stereo-lithography (SL), FDM, SLS, laminated object manufacturing (LOM), and Poly-jet were tested and compared[39].

Other archival literature on fatigue behavior of laser-sintered nylon (PA12) showed that PA12 specimens under rotating-bending experiment will fail in fatigue[40]. It was suggested that, although high frequency loading will cause a heat build-up in the specimen (temperature stabilized between 20-30 ^{o}C), but rotating-bending at frequencies of up to 50 Hz is a valid way of determining the fatigue behavior of laser-sintered PA12 specimens. Parts made by stereo-lithography (SLA) process were investigated to find influence of layer thickness on mechanical properties of produced parts[41]. Results showed that when layer thickness decreases, strength of parts made by SLA will increase. Another effort has been done on effects of electroplating on polymer parts made by SLA process[42]. A series of tests were conducted on coated samples with copper and nickel with varying thickness. Physical tests confirmed that thicker coating (120 μm) increased the impact energy and Young's modulus but had a minimal effect on ductility of parts, in which thinner coating (20 μm) resulted in smoother surface finish than thicker one. A computer aided characterization approach has also been used to evaluate the effective mechanical properties of porous biodegradable

polyesters tissue scaffold[43]. An approach for design and 3D-printing of porous tissue scaffold and characterization of the effective mechanical properties of extruded porous poly-ε-caprolactone scaffold was presented.

In addition, there are also some efforts on mechanical properties of additive manufactured metals available in literature. They have been tested and simulated for fracture criteria, fatigue, tensile strength, etc[44–51]. Behavior of parts produced by Selective Laser Melting (SLM) has been compared to conventionally produced products for traction, compression and flexure test[52]. Additive manufactured AlSi10Mg using SLM was studied in terms of microstructure, high cycle fatigue, and fracture behavior[53]. For approximating flexural properties of bone, open cellular structures fabricated in Ti6Al4V using the Electron Beam Melting (EBM) have been proposed for tissue scaffold and low stiffness implants[54]. In another study, the effect of build orientation selection and heat treatment on the mechanical properties of Selective Laser Melted (SLM) Ti6Al4V lattice structures was investigated[55]. Different binding mechanisms were also investigated in Selective Laser Sintering (SLS) and Selective Laser Melting (SLM) with metal powder to compare the mechanical properties and also improve understanding of these processes[56].

The studies on the dynamic behavior of the 3D printed materials especially during collision are limited and not current given the increased use of AM parts in industry. Simulation of impact can be divided into two phases, compression and restitution[57]. The contact force between the objects during each of these phases is the most important factor needed to simulate the impact. The contact force itself can be divided into three phases, fully elastic, elastic-plastic and fully plastic phases. The fully elastic and fully plastic phases can be solved analytically. Hertzian theory has been commonly used for fully elastic phase. Also for the fully plastic phase there are few alternative approaches that can be found in available literature[58,59].

Unfortunately, to date, the elastic-plastic phase is not amenable to closed-form analytical solution. Arguably, for the collision problems the elastic-plastic phase plays the most important role. Many efforts have been pursued to predict the elastic-plastic contact forces for homogeneous metal materials[58–61]. A comprehensive comparison between different contact models for collision problems can also be found in literature[62]. However, these contact models have been developed for quasi static contacts, they have often been used for collision problems[63–69].

3. Research Questions

The hypotheses in this work are related to the interaction between 3D-printed surfaces and periphytic communities under conditions found in both natural and laboratory-based settings. Also the investigation of properties and behavior of 3D-printed polymers under collision targets to provide a better understanding of the behavior of such surfaces under dynamic contacts in real world situations.

- Do periphyton species have attachment preferences using custom designed 3D-printed surfaces towards certain substrata topography in natural settings?
- Do surface roughness profile height and interstitial space have impact on total biomass of benthic algal communities in laboratory-based environment?
- How is the behavior of 3D-printed polymers, both theoretically and experimentally, under low speed collision? Also, what would be the formulation for contact force models of these materials to match these polymers behavior?

4. Preliminary work

The general idea of the preliminary work was two-fold: (i) to demonstrate the feasibility of using AM technologies to engineer substratum surface textures that are suitable for colonization of algal biofilms[70]; and (2) to develop and refine the experimental methods for growth plate design and manufacturing, surface topography measurement, microscopy methods, and harvesting/sampling techniques. The specific objectives for preliminary phase were as follows: (i) to demonstrate that algal biofilms can colonize 3D printed substrata both in laboratory-based bioreactors as well as in natural settings; (ii) to draw preliminary observations on the influence of 3D-printed surface topography on the rates of attachment and growth of algal biofilms.

Three separate experiments were conducted to demonstrate the potential of using 3D-printed technologies for the production of surfaces for algal biofilm colonization under a variety of conditions. For these experiments, various surfaces were designed and fabricated in an Objet 30 machine (Stratasys® Ltd., Eden Prairie, Minnesota), which uses a polyjet technology to deposit a layer (28 µm thick) of UV-light cured acrylic polymer. In general, these designs were subjected to various conditions of algal culture and investigated for rate of colonization and growth of algae.

4.1 Growth feasibility on 3D-printed surfaces in controlled bioreactor cultivators

The first preliminary experiment involved designing, fabricating and placing two different growth plates in a laboratory bioreactor cultivator. The purpose of this experiment was to demonstrate that algal biofilms can indeed attach to and colonize 3D printed polymer surfaces and to investigate the feasibility of using surface feature sizes to support regenerative harvesting.

The growth plates were designed in Solidworks® (Dassault Systèmes SolidWorks Corp., Waltham, Massachusetts) and fabricated in the Objet 30 printer. A rectangular plate (90 mm x 100 mm) with four parallel channels and 5 mm collimating walls was designed with hemispherical

surface features of increasing scale. The first channel was ideally smooth (Ra=0.198 µm), while the remaining three channels had a pattern of adjacent hemispheres of diameters 500 µm, 1000 µm, and 2000 µm. The second plate was circular in shape (diameter of 100 mm) with each quadrant containing the same scale of features as in the rectangular plate. Anchor points were designed into the plates for ease of attachment to the bottom mesh in the bioreactors. Figure 4 shows the computer models with the corresponding fabricated versions of the two different growth plates used in this experiment.

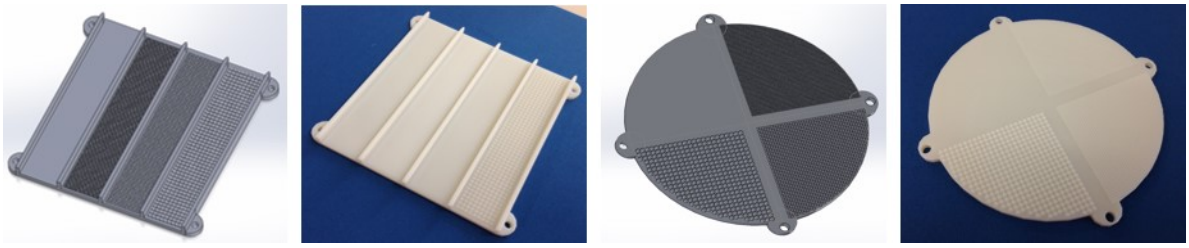

Figure 4: CAD models and 3D printed (rectangular and circular) growth plates

The plates were placed in a bench-scale benthic algal cultivator in the laboratory[71] (figure 5). The cultivator is a shallow trough in which attached benthic filamentous algae are typically grown on polypropylene screen substratum placed at the bottom of the trough. Water pumped from a reservoir continuously flows over the substratum in a thin layer (1-2 cm deep) and returns to the reservoir where a submersible pump recirculates it. A tipping bucket mechanism provides a periodic wave surge that helps stimulate the growth of benthic algae and disperse the nutrients. The cultivator was operated continuously at a flow rate of 45 L min^{-1} with a tipping frequency of 4 min^{-1}. Lighting was provided continuously by two 400 W metal halide grow lamps (Virtual Sun®, La Verne, California) located directly above the center of the cultivator. The plates were fixed to the substratum screen at the anchor points and remained in place for 45 days.

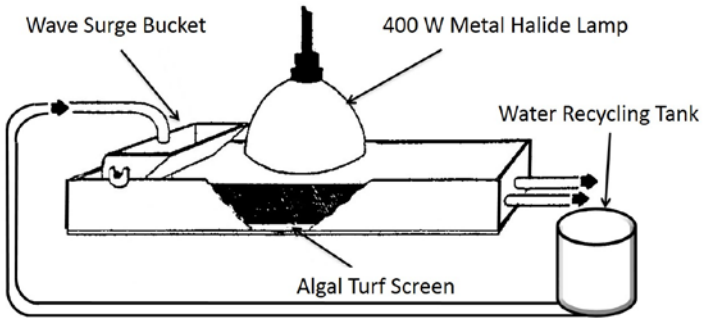

Figure 5: Schematic view of benthic algal cultivator

The cultivator was inoculated with a mixed algal community sampled from local streams that was dominated by *Spirogyra communis*. The cultivator was dosed daily with commercial F/2 media (Pentair Co., Apopka, Florida) at the recommended loading concentration rate (1 ml nutrient per 1 gallon of water). Following colonization, tiles were removed and imaged using optical microscopy at low magnification (10X to 40X for topographical attachment) and higher magnification (100X for algal species identification). Biomass was sampled at 3 locations from each channel and quadrant respectively, mixed and homogenized, and subsampled for species identification using optical microscopy. Biomass was then sacrificially harvested from the plates using mechanical scraping, washing and vacuuming. The wash eluent was vacuum-filtered using Whatman GF/C glass fiber filters. Biomass dry weight was analyzed via filtration of 20 mL subsamples with a drying oven at 105 °C and averaged.[72] The surfaces of the two plates were scanned with 3D axial chromatic (non-contact) profilometer (Nanovea® ST400, Irvine, California). The optical pen provided a 1.4 mm Z-range with 20-nanometer resolution and over an area of 150 mm x 150 mm. Roughness measurements were collected from the new plates (before placement in the cultivators) and after vacuum harvesting.

The results after harvesting demonstrated that the algal biofilm attached firmly to the printed surface in certain locations, resulting in patches of bare and colonized zones. The amount of

residual biomass following harvest was related to the significant length of the surface features, with more biomass remaining for the larger diameter (1000 and 2000 µm) features.

4.2 Feasibility of natural environment species recruitment on 3D printed growth surfaces

The second preliminary experiment focused on investigating the recruitment of colonizing algal species from natural freshwater environments. In order to accomplish this, multiple sets of 48 by 48 mm 3D printed tiles and paired unglazed ceramic tiles (to serve as experimental controls) were deployed in several local rivers and streams in eastern Alabama. All printed tiles were manufactured as smooth as possible with Ra values ranging from 0.198 µm to 0.932 µm. The ceramic tiles used in the experiment had a measured average roughness (Ra) ranging from 1.144 µm to 1.855 µm. Figure 6 shows the tile arrangement on plastic mesh mats as well as the location in one of the natural streams.

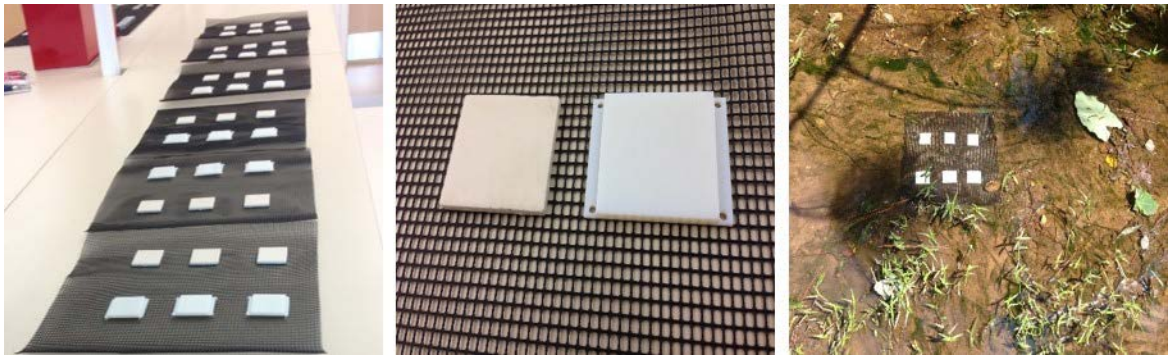

(a) **(b)** **(c)**

Figure 6: (a) Mesh mats with tiles, (b) Close-up view of ceramic and printed tiles, and (c) placement in one of the streams

The tiles were placed in three different streams and monitored on a weekly basis for integrity and algal growth. The tiles were left on location for 30 days and then removed for measurement and

analysis in the laboratory. After removal, tiles were imaged at low magnification (10X to 40X) via digital microscopy. Also, the biofilm was subsampled at three locations, and subsamples were mixed and stored in 10% buffered formalin solution for species identification using optical microscopy.

Results appear to indicate that, in many cases, algae from the stream colonized printed tiles at densities greater than those found on ceramic control tiles (Figure 7a). In some instances, the biofilm coverage on 3D printed tiles covered across the entire surface (Figure 7b). Micrograph analysis of the biofilm displayed a diversity of algal types and morphologies (Figure 7c), with filamentous and prostrate varieties often dominant.

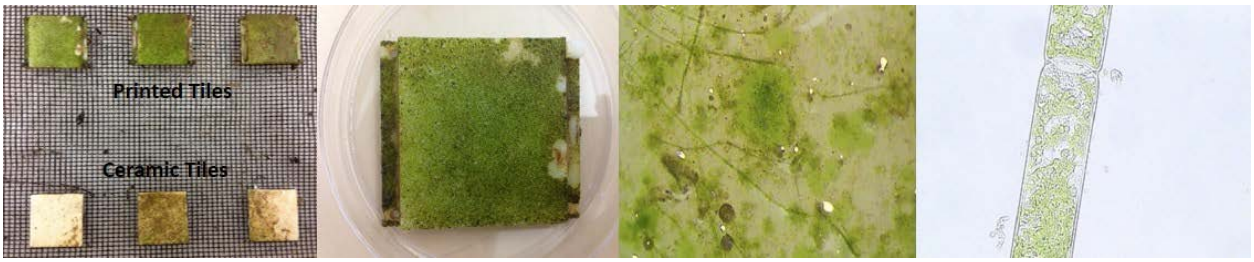

(a) **(b)** **(c)** **(d)**

Figure 7: Mesh mats from natural streams with ceramic and 3D printed tiles: (a) after removal on day 30; (b) photograph of biofilm covering 3D printed tile; (c) micrograph at 40X of biofilm colonizing 3D printed tile; (d) micrograph 400X of *Spirogyra*

4.3 Algal colonization feasibility on complex scaffold geometries

The third preliminary experiment involved the design and manufacture of 3D printed cube scaffolds that presented very high surface area for attachment and colonization and that are impossible to manufacture other than using additive methods. The structures were based on a mathematical model for a gyroid, a special case of a triply periodic minimal surface (Figure 8). The gyroid surface can be described by this equation:

$$\sin x * \cos y + \sin y * \cos z + \sin z * \cos x = 0 \quad (1)$$

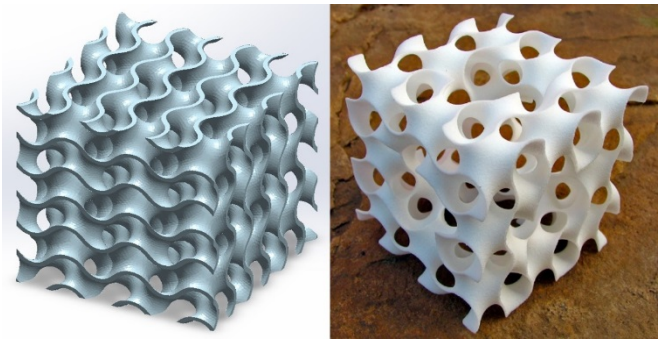

Figure 8: Designed model with Solidworks (left), and 3D-printed model (right)

The dimensions of the gyroid cube were 20 mm by 20 mm with a calculated surface area of 8127 mm^2, over three times that available from an identical sized cube with solid facets and over 19 times that of a square tile of similar base footprint. The gyroid cube was placed in a beaker and immersed in a mixed algal culture inoculated from collections from a local stream dominated by *Spirogyra communis*. The gyroid was cultured in commercial F/2 media at ambient laboratory temperature under fluorescent full spectrum grow lights (EnviroGro FLT22, Hydrofarm, Petaluma, California). Culture agitation was supplied by a rocking platform table (VWR International, Radnor, Pennsylvania), which was set to 20 oscillations per minute. Culture media was added every week to replace evaporative losses.

For analysis following culturing, the gyroid was removed from the culture after 15 and 30 days and imaged at multiple magnifications. At the 30-day removal, the biofilm was subsampled at three locations, and subsamples were mixed and stored in 10% buffered formalin solution for species identification using optical microscopy. The wet gyroid structure with biofilm was weighed and recorded. The dry weight of the biofilm biomass was estimated by drying the gyroid structure at 50 °C for greater than 48 hours, after which repeated measures of weight were taken every 24 hours until no change between subsequent measurement was observed. A set of five

control gyroid structures were placed in the same oven and weighing procedure as a control to measure mass loss during drying from the polymer material. The biomass dry weight was estimated by subtracting the dry weight of the control gyroid from the dry weight of the experimental gyroid. Preliminary data on weight of dry biomass showed a big difference between algae attached to gyroid cubes removed after 30 days than others.

Figure 9 shows the progressive colonization of the gyroid surfaces over a period of 30 days. The high surface area clearly provides ample opportunity for the algae spores to settle and anchor to initiate colonization. Simple observation indicates that colonization took place in every leaf deep inside the gyroid, indicating that the delivery of nutrients by flow was appropriate. No bare areas or spots were noticeable anywhere on the gyroid structure.

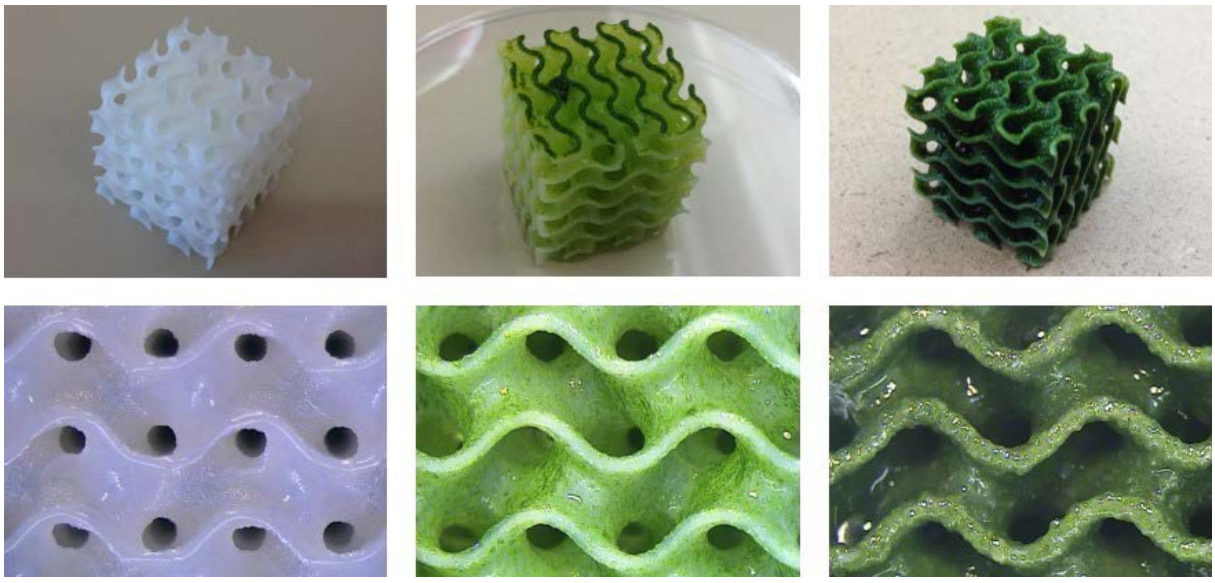

(a) **(b)** **(c)**

Figure 9: Photographs (top row) and micrographs (10X bottom row) of the gyroid cube at (a) time of manufacture; (b) 15 days, (c) 30 days

This preliminary work sought to establish the feasibility of colonization of printed surfaces for

enhanced algal biomass production. The following hypotheses were teased out of the experiments and are the subject of ongoing research: (i) there is a topography effect on the colonization rate of benthic algae and optimal values of certain surface texture parameters exist; (ii) substratum textures can be designed for optimal interstitial spacing between surface asperities and micro-replicated features to shorten the lifecycle of the next algae crop, and (iii) increased efficiencies in the packing of biomass can be achieved by complex geometries that provide very high surface area in compact volumes.

Based on the observations of preliminary efforts, three experiments were designed to study on improving algal cell density attached to surface by knowing different species attachment preferences and understand surface characterization to increase algal biomass. These experiments were designed to demonstrate important role of surface texture in algal attachment by changing area of contact between the algal cells and solid carrier surface as well as the potential for increasing the yield and productivity of algal biosystems because of their application in aquatic pollution recovery, water quality improvements, as well as biomass production for various economic uses including protein production and biofuels.

5. Experiment#1: Impact of substrata topography on the attachment preferences of periphyton communities in natural streams

The primary objective of this study is to investigate the effect of surface topography features on the differential attachment and colonization dynamics of benthic algal species in a mixed community in a natural stream. A secondary objective is to demonstrate the use of 3D printing technologies to design and fabricate replicated platforms needed to test selective behavior of species attachment.

The overall methodology consisted of designing and fabricating twelve growth plates, each with six regions presenting different surface textures, using polyjet-based 3D printer. The plates were then placed in two different locations in a creek and left exposed to the natural conditions over a period of 33 days. After collection, the biomass was carefully harvested in each region and studied microscopically for species identification. Non-parametric statistical analyses were conducted to confirm the effects of surface topography on attachment and growth. This section provides details in each of the steps in the methods.

5.1. Materials and Methods

Broadly, the methodology for this experiment consisted of designing and fabricating twelve growth plates, each with six regions with different surface textures, using polyjet-based 3D printing. The plates were then placed at two different locations in the riverbed of a local creek and left exposed to the natural conditions over a period of 33 days. After collection, the biomass was carefully harvested in each region and studied microscopically for species identification. Non-parametric statistical analyses were conducted to confirm the effects of surface topography on attachment and growth.

Acrylic polymer growth plates were designed in Solidworks® and fabricated with a Stratasys®

Objet30 3D printer with a 28 µm layer thickness. Twelve rectangular plates (55mm × 74mm × 4mm) with four anchor points on corners were designed and printed. Anchor points were designed for ease of attachment to a plastic mesh for placement in the stream. Each printed tile represented six topography sections with hemispherical surface features of increasing radius. The sections included an ideally smooth area (area roughness average of Sa=1.19 µm), and five sections with a pattern of adjacent hemispheres of average area peak-to-valley height (Rz) of 100, 500, 1000, 1500, and 2000 µm respectively (Figure 10).

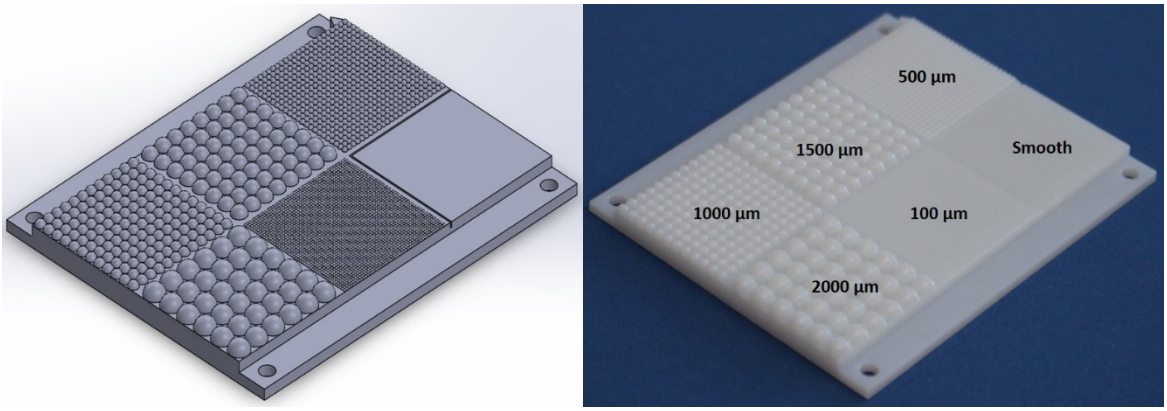

Figure 10: Computer Model (left) and fabricated growth plate (right)

The accuracy of the build was confirmed with optical methods using a confocal white-light profilometer (Nanovea ST-400) with 20 nanometer resolution in the Z axis. Figure 11 shows the aerial map and the 2D line scan of the surface topography for the 500 µm section. The fabrication dimensional error was less than 1% for the areas with radii 500, 1000, 1500 and 2000 µm. For the section with radius size of 100 µm, the dimensional error was of the order of 20% with most radius sizes in this section, thus interstitial space, falling in the range of 77 µm –100 µm. This is attributed to the feature size approaching the fabrication capability limit of printer in the lateral direction.

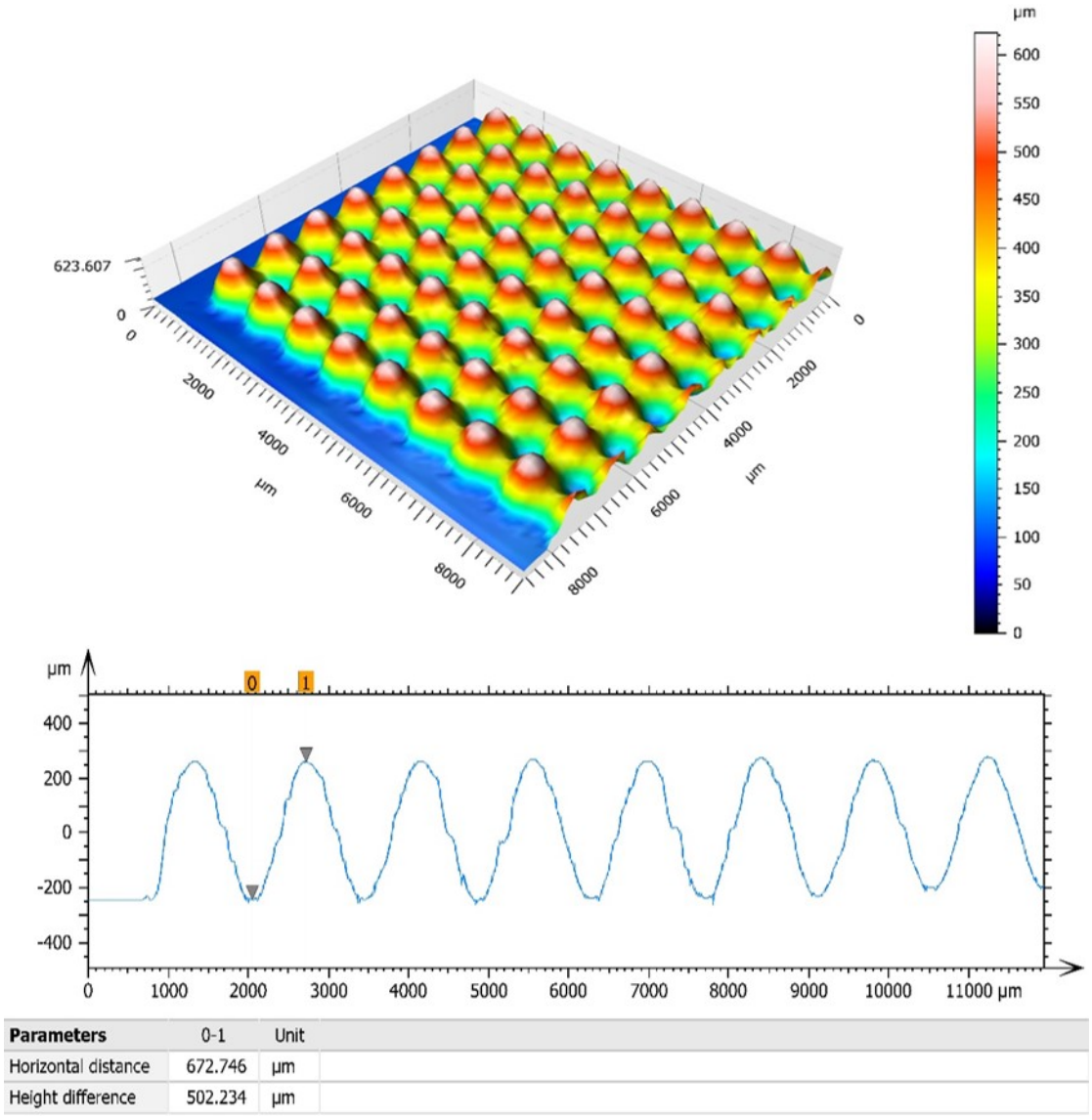

Parameters	0-1	Unit
Horizontal distance	672.746	µm
Height difference	502.234	µm

Figure 11: Aerial height map and 2D profile of 500 µm section

The growth plates were attached to two polypropylene screen mats in an alternating order such that different sections on tiles faced upstream/downstream configuration. These mats were placed in adjacent locations in the creek and left exposed for a period of 33 consecutive days. The sites selected for these deployments were in Chewacla Creek, located in Chewacla State Park, Auburn, Alabama (32°32'51.0"N 85°28'53.7"W). The stream had continuous flow without curve in almost 150 m up stream (Figure 12) and with mostly large cobbles in stream bed close to the experimental

mats location. Also, in the bankfull cross-section of the creek, bankfull width per bankfull depth ratio (W_{bkf}/d_{bkf}) is 27.3 with the slope of 0.0046, in which bankfull width and depth are the stream channel width and average depth at bankfull discharge level, respectively[73].

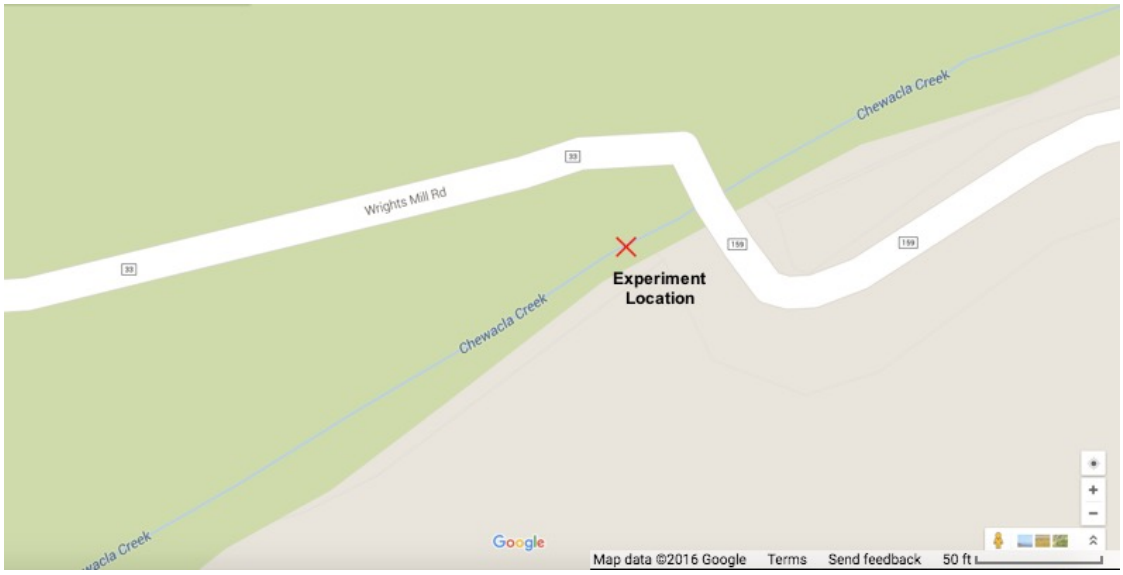

Figure 12: Aerial view of Chewacla Creek from about 150 m up and down stream of experiment location[74]

The screen mats were placed in the same creek cross-section of the stream at which there is USGS station that records information on water discharge and water level every fifteen minutes[75]. The average gage height during experiment period was 1.85 ±0.13 ft., while water discharge during same time was 18.23±11.77 ft^3/s (Figure 13).

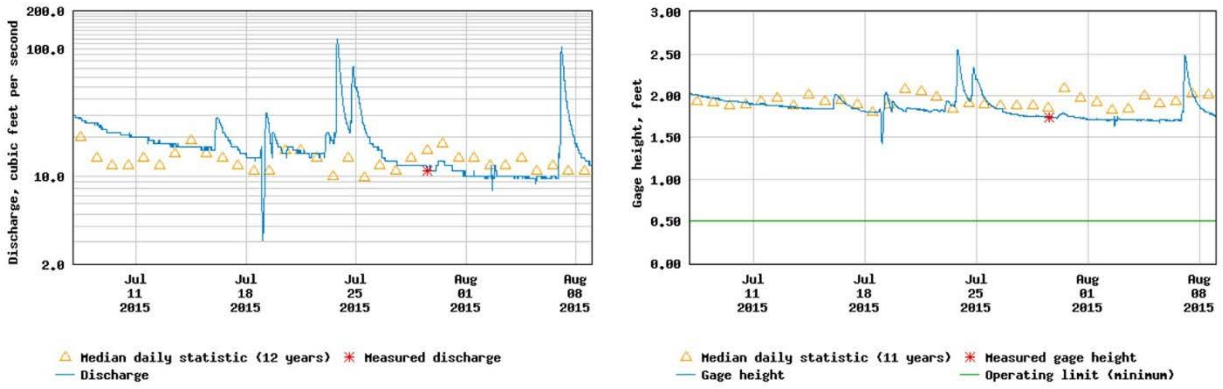

Figure 13: Chewacla creek discharge (left) and gage height (right) during experiment (source: USGS Chewacla website)

In addition, temperature and light intensity were recorded every 15 minutes using an in-situ data logger (HOBO Pendant, Onset Corp., Bourne, MA) installed at the depth of the mats. Over 3000 readings of temperature and light intensity were collected. The mean water temperature during experiment was 27.8 ±1.2 ^{o}C. The locations of deployment were partially shaded with a median daytime light intensity of 223 µmol/m^2/s. The pH and conductivity of the water were measured weekly with a handheld combination pH/EC probe (HI 98130, Hanna Instruments, Woonsocket, RI), and averaged 7.36 ±0.18 and 0.15 ±0.05 mS/cm, respectively. Local stream velocity was measured weekly with a Model 2100 current flow velocity meter (Swoffer Instruments, Inc., Tukwila, WA) at the locations of tile installation, and averaged 0.24 ±0.09 m/s. Both dissolved P and N concentrations were moderately low (PO_4-P: 0.080 ±0.020 mg l-1; NO_3-N: 0.52 ±0.19 mg l-1, n = 5), as measured with a YSI 9500 field photometer (YSI Inc., Yellow Springs, Ohio). The growth plates were placed in the stream on July 7th, 2015 and recovered on August 8th, 2015 for a total exposure of 33 days.

After removing the growth plates from screens, each section was imaged and documented at low magnification (10X to 40X) via digital microscopy. Each section within each plate was harvested with several methods, including vacuuming, mechanical scraping, and washing with low-pressure

distilled water, to recover as much biomass as possible. The biomass collected from each section was stored separately in vials containing 30 ml of mixed, harvested samples, DI water, and 0.15 ml of glutaraldehyde, 50% solution, for preservation. There were a total of 72 vials (one for each of the 6 topography sections across 12 growth plates).

The species identification effort was conducted via digital microscopy (400X to 1000X) using a Motic optical microscope (Motic Corp., Richmond, BC). The microscope sample preparation included a thorough mixing of the vial, which was then transferred onto a glass slide for observation. Three sub-samples, each with a volume of 0.063 ml, were drawn from each vial (representing the individual growth plate sections) and from which 30 micrographs were obtained from each sub-sample. A total of 216 sub-samples and 6480 micrographs resulted from this approach. The algae observation in the micrographs were keyed to at least the genus level using standard identification keys[76]. A preliminary observation on a subset of the micrographs resulted in the development of a custom species identification key containing those 12 most commonly found species. This key was used to train two laboratory analysts who each scanned the entire set of micrographs independently and recorded observations on presence/absence of each species in each micrograph. The independent observations from the two analysts were compared, showing a high degree of agreement between the two, with discrepancies on the observations found in only 2% of the micrographs. These micrographs were then revisited and jointly analyzed until a consensus on the species identification was reached.

The presence/absence data for the predominant 12 species were recorded and analyzed for patterns and distribution. The numbers of each species observed during the identifying process were counted for each topography section, and numbers of species were pooled for each of the 6 unique surface topographies.

The statistical analysis performed on the micrograph data were first analyzed for the underlying ANOVA assumptions, including a test for equal variance and an analysis of the residual plots. For those species data where the ANOVA assumptions were violated, non-parametric statistical tests were employed. This included the Kruskal-Wallis test on the medians followed by the Mann-Whitney test for pairwise comparison. These analyses were used to indicate species preferences towards surface topography.

In addition, Simpson's index[77] was calculated to represent the diversity of species per topographic section. This was calculated as $D = \sum n(n-1)/N(N-1)$, where D is the probability that two individuals randomly selected from a surface topographic section will belong to the same species, n is the total number of each individual species on each surface topographic section, and N is the total number of all species combined on each surface topographic section. Consequently, *1-D* shows the probability that two individuals randomly selected from each surface topographic section will belong to different species. With this information, the various surface topographies were ranked from the one presenting the most diverse community to the least.

5.2 Results

Every one of the 216 sub-samples was documented with 30 micrographs each via digital microscopy (Appendix I). Each of the 6480 micrographs was observed by two trained analysts. This yielded 12 conspicuous species of algae that were identified and occurred with relatively high frequency (Table 1). Figure 14 shows all species which were identified during identification process. A large number of diatoms (division *Bacillariophyta*) were observed in the samples, accounting for 56% of the observed species (Figure 15), both identified and unidentified. Identified species accounted for 46% of all species found and were distributed across 4 divisions. The most abundant alga identified was *Choleochate orbicularis*, the only species found within the division

Charophyta, which in turn was present on 20% of all the samples. Three species belonging to the division *Chlorophyta* were identified on 12% of the samples. The greatest number of species was identified in *Bacillariophyta* division, which appeared in 8% of all samples and where 5 distinct species were identified.

Micrograph					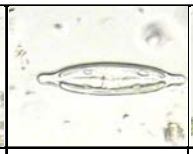	
Surface Features	*Gyrosigma sp.*	*Oscillatoria trichomes*	*Cymbella sp.*	*Stauroneis sp.*	*Caloneis amphisbaena*	*Microspora Willeana*
Smooth	0	12	18	17	2	27
100 µm	0	21	10	21	6	24
500 µm	0	14	15	20	0	17
1000 µm	2	19	16	17	7	4
1500 µm	0	22	8	19	5	4
2000 µm	3	22	15	22	4	14

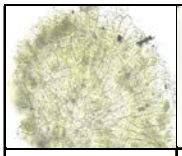	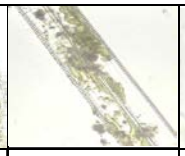	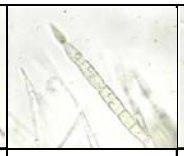		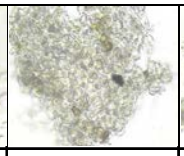	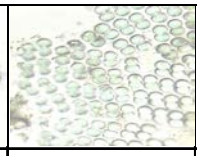
Coleochaete orbicularis	*Synedra ulna*	*Chaetophora sp.*	*Stigeoclonium tenue*	*Aphanothece clathrata*	*Aphanocapsa elachista*
111	2	0	45	10	1
109	0	8	53	5	0
71	4	2	22	6	1
95	5	4	23	10	1
103	0	2	37	13	1
93	3	1	64	7	0

Figure 14. Micrographs and number of all identified species

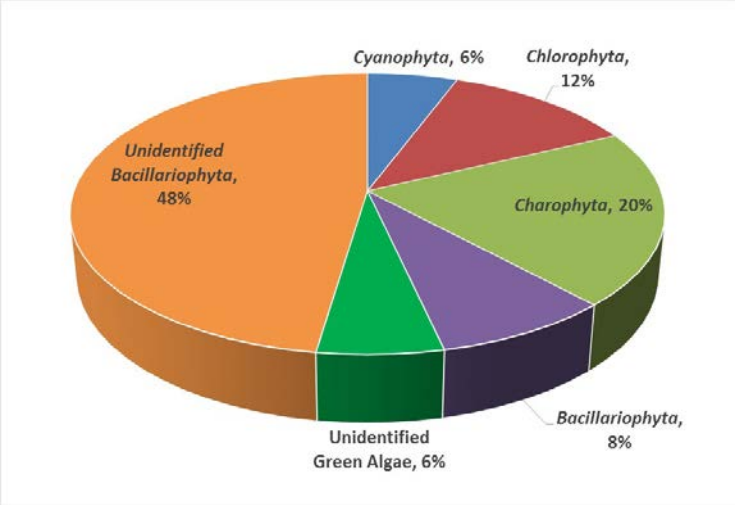

Figure 15. Percent distribution of the number of positive identification of individual algal species, according to division

Table 1. Division, genus and species of the identified algal species.

Division, Genus and species
Div. *Bacillariophyta*
Caloneis amphisbaena
Cymbella sp.
Gyrosigma sp.
Stauroneis sp.
Synedra ulna
Div. *Charophyta*
Coleochaete orbicularis
Div. *Chlorophyta*
Chaetophora sp.
Microspora willeana
Stigeoclonium tenue
Div. *Cyanophyta*
Aphanocapsa elachista
Aphanothece clathrata
Oscillatoria trichomes

The relative occurrence of the 12 major identified algae species varied as a function of topography section (Figure 16). The most abundant species identified on all sections was the charaophyte *Coleochaete orbicularis*, followed by the chlorophyte *Stigeoclonium tenue.* Species that were

identified but occurred rarely were *Aphanocapsa elachista*, *Chaetophora* sp., and *Gyrosigma* sp. Some species were observed on only a few topography sections. *Gyrosigma* sp. occurred only on 1000 and 2000 µm sections; *Synedra ulna* occurred on all but the 100 and 1500 µm sections; *Chaetophora* sp. occurred on all but the Smooth sections. The distribution of the relative abundance varied across all sections for all other species.

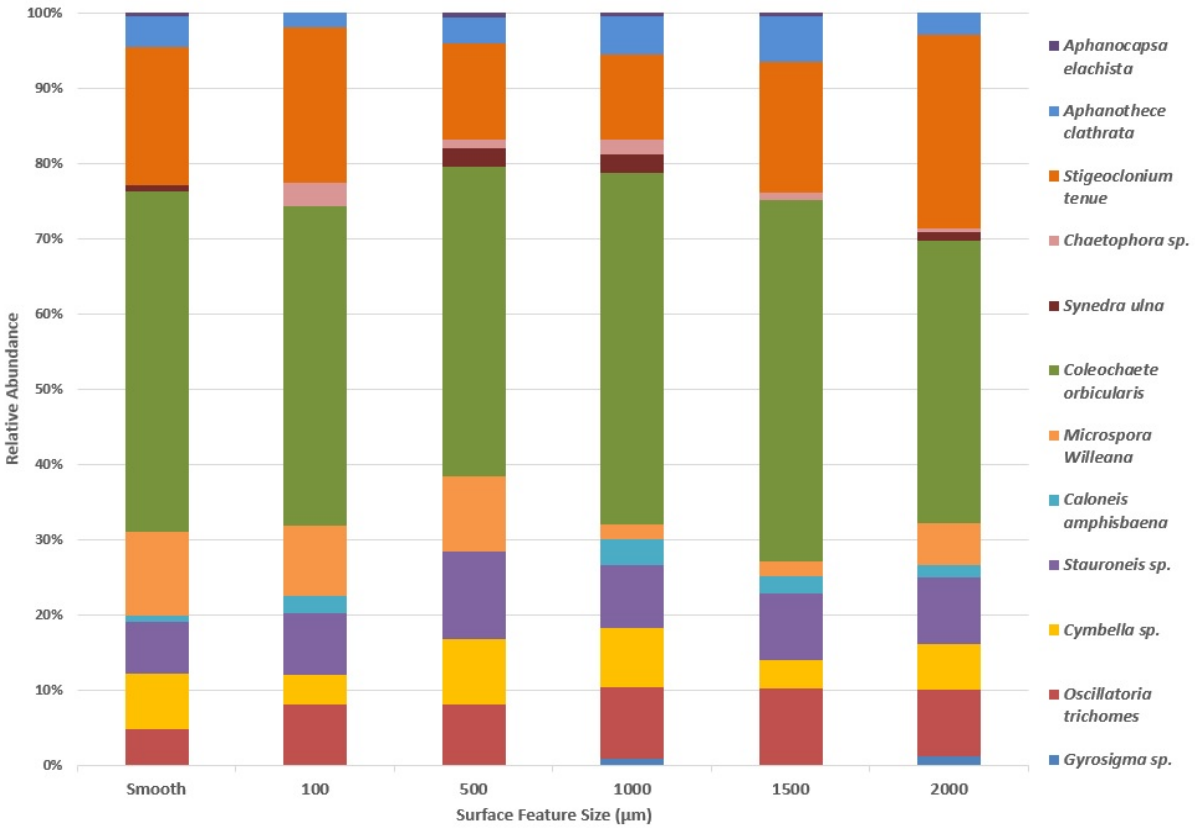

Figure 16. Relative abundance of those species identified as a function of surface topography treatment

Species diversity as measured by Simpson's index (SI) is reported for all topography sections in Table 2. The highest diversity index was observed in the 500 µm section (SI = 0.774), whereas the lowest diversity was observed in the 1500 µm section (SI = 0.714). The Simpson's diversity index was seen to vary over the range of roughness feature sizes (Figure 17), initially increasing from the smooth to the 500 µm section, decreasing from the 500 µm to the 1500 µm section, and

increasing again for the 2000 μm section.

Table 2. Total number of algal species identified and Simpson's diversity index calculated for each surface feature section.

Surface Topography (μm)	Total Number of Identified Algae (N)	$D = \frac{\sum n(n-1)}{N(N-1)}$	Simpson's Diversity Index $(1 - D)$
Smooth	245	0.266	0.734
100 μm	257	0.248	0.752
500 μm	172	0.226	0.774
1000 μm	203	0.259	0.741
1500 μm	214	0.286	0.714
2000 μm	248	0.231	0.769

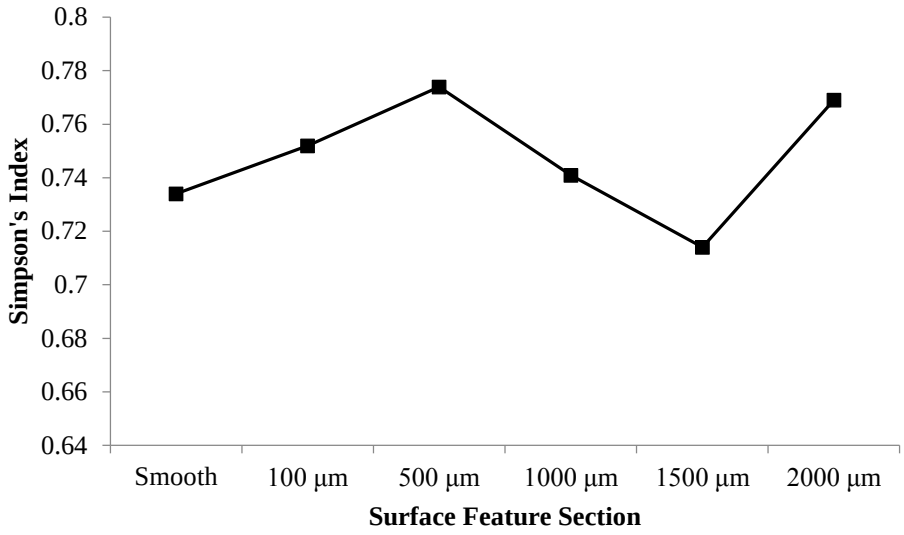

Figure 17. Simpson's diversity index versus surface feature section with increasing feature size.

Statistical analysis for the significance in differences of relative abundance for each identified species was performed. A test for equal-variances as well as an analysis on the normality of the residuals confirmed that the species data in this experiment violate the normality and homoscedasticity assumptions of the Analysis of Variance (Figure 18).

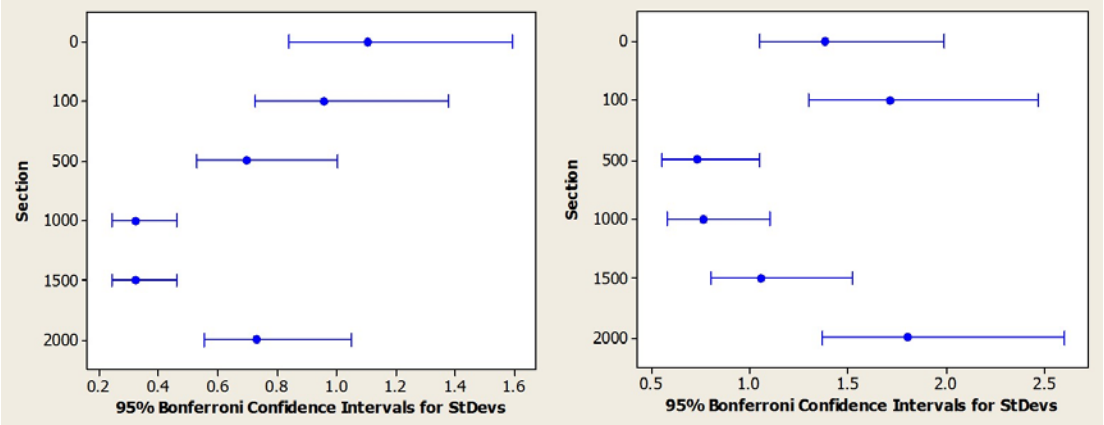

(a) **(b)**

Figure 18. Test for equal variances for (a) *Microspora willeana* and (b) *Stigeoclonium tenue*

Figure 19 shows normal probability plot for residual analysis for both species by Minitab which perfectly displays normality assumption of residuals are violated.

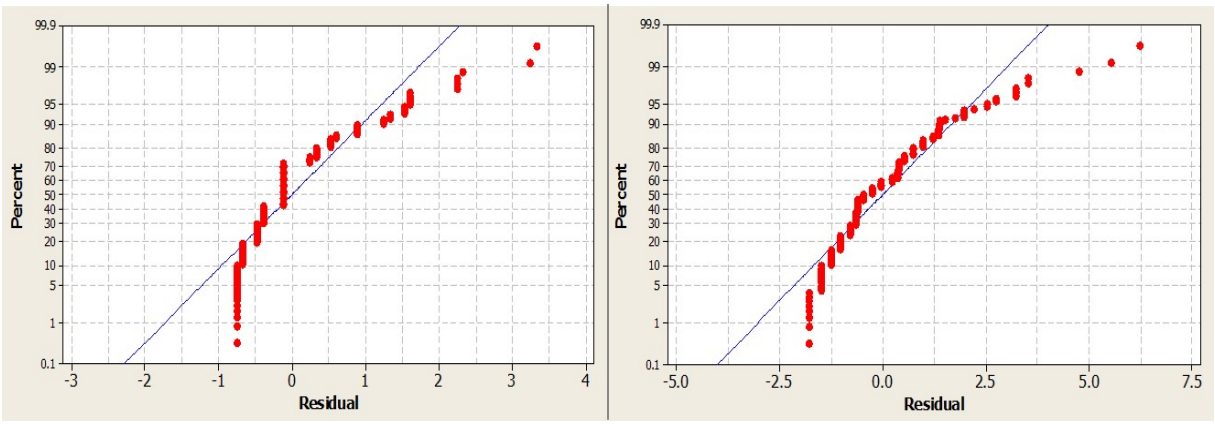

(a) **(b)**

Figure 19. Normal probability plot for (a) *Microspora willeana* and (b) *Stigeoclonium tenue*

Consequently, the species data was analyzed with the Kruskal-Wallis non-parametric test on the medians. Out of the twelve species that were identified, only two (*Microspora willeana* and *Stigeoclonium tenue*) presented a variation in relative abundance across sections that was statistically significant, thus the discussion is reduced to these two species.

With respect to *Microspora willeana*, the Kruskal-Wallis test suggests that the samples extracted from some of the topographic sections may come from populations that have different medians. In particular, the test clearly shows that the medians from the 1000 and 1500 μm conditions are substantially lower than those from the smooth, 100 and 500 μm, conditions (H = 20.88, *p*-value adjusted for ties = 0.001) (Table 3). In addition, a non-parametric Mann-Whitney paired test was used to determine the difference between two groups of topographical conditions: radius <=500 μm (i.e. smooth, 100 and 500 μm) versus radius > 500 μm (i.e. 1000, 1500 and 2000 μm). The W-statistic rejects the null-hypothesis of equal median and reports a significant difference ($\alpha = 0.001$) between the medians of *Microspora willeana* abundance in these two topographical sections. Specifically, the test reports that the median of the population of the group containing those topographical conditions that are <=500 μm is larger than the median of the population containing the topographical conditions that are >500 μm.

Table 3. Kruskal-Wallis test results for *Microspora willeana*

Topography	N	Median	Average Rank	Z
Smooth	36	0.000	125.1	1.75
100	36	0.000	125.8	1.82
500	36	0.000	116.3	0.82
1000	36	0.000	88.8	-2.07
1500	36	0.000	88.8	-2.07
2000	36	0.000	106.2	-0.24
Overall	216		108.5	

For *Stigeoclonium tenue*, the Kruskal-Wallis test also suggests that the samples from some of the topographic sections may come from populations that have different medians (H = 16.49, *p*-value = 0.006) (Table 4). Based on the results for medians of different topographic sections, three categories were created. In this way, the data from the smooth and the 100 μm sections categories

were pooled into a class called “Low”, the 500 and 1000 μm sections categories were pooled into a class called “Medium” while the 1500 and 2000 μm sections categories were pooled into a class called “High”. The Kruskal Wallis test shows differences at $\alpha = 0.05$ significance in which the *Stigeoclonium tenue* abundance versus class (3 categories) are significantly different (*p*-value = 0.001). The results strongly suggest that *Stigeoclonium tenue* is more abundant in the high and low categories, and less abundant in the medium category.

Table 4. Kruskal-Wallis test results for *Stigeoclonium tenue*

Topography	N	Median	Average Rank	Z
Smooth	36	1.00	114.8	0.67
100	36	1.00	118.5	1.05
500	36	0.00	86.8	-2.28
1000	36	0.00	88.3	-2.13
1500	36	1.00	109.8	0.14
2000	36	1.00	132.8	2.55
Overall	216		108.5	

5.3 Discussion

Although a common material for manufactured product development, the 3D-printed acrylic polymer has not been widely reported for use in attracting periphytic biofilms[70]. Although, there is some history of the use of acrylic material for colonization studies[78–80]. In these investigations, a diverse group of algae colonized the printed acrylic tiles. Species were identified from 4 known divisions of algae, and these were typical species common in freshwater periphyton communities of the southeastern United States. The morphology of the species identified was primarily prostrate, with some filamentous and branched filamentous forms observed as well, attesting to the moderate flow velocities observed at the site. A majority of the species identified on the printed tiles were diatoms, as might be expected for flowing freshwater environments in this region,

although many of this group were not identified in this study (Figure 15). Of those species identified, the most commonly observed was the charaphyte species *Coleochaete orbicularis*, with a prostrate sprawling disc morphology that occurs on most surfaces in flowing freshwaters. Filamentous green algae were observed as fairly common as well. As such, the diversity of the colonization of species appeared not to be limited by the nature of the printed material, and establishes the approach for using 3D printing for experimental surfaces as a viable option for periphyton sampling methodology where controlled surface textures and topographies are required.

The set of species that occurred on each surface area topography varied in ways that could only be seen as a result of the interaction between the local flow characteristics induced by the surface condition and the particular species in the community. The variation in abundance between different topographies for certain species was notable and significant. For example, *Microspora willeana* was seen to be significantly more abundant in surfaces with topographical features with a radius less than 500 μm, and the species *Stigeoclonium tenue* showed significantly more abundance in surfaces with topographical features with small radius (less than or equal to 100 μm) and large radius (greater than or equal to 1500 μm). As such, these two species showed a significant anti-preference for surfaces with feature sizes in the 500-1000 μm radius range, exhibiting statistically significantly lower abundance in these areas. The abundance characteristics of various species were also notable because of their absence from particular area topography. For example, the species *Gyrosigma* was observed to be present only on larger features (1000 to 2000 μm), and the species *Synedra ulna* was not present in areas with features of 100 and 1500 μm. These abundance observations demonstrate the preferences of species for particular surface conditions or interactions with surface topographical feature sizes.

The interaction of the various species in the community with the different surface topographical feature sizes is borne out by the metrics of diversity as well. With respect to Simpson's diversity index, the surface with the feature size of 500 μm presented the highest value, which indicates a more even distribution of numbers of observations over the total number of species. The lowest Simpson's index was observed on the areas with the smooth and 1500 μm feature sizes. The pattern of variation of Simpson's index over the range of surface features (Figure 17) shows first an increase from smooth to 500 μm, then a decrease from 500 to 1500 μm, and finally an increase at 2000 μm. This variation in species diversity suggests an optimum feature size somewhere in the range of 500 μm for maximizing diversity of the colonizing algal community in this environment. This information can also be used if the target substrata design aims at minimizing the diversity of species present in the community. Smooth surfaces and those with feature sizes in the neighborhood of 1500 μm appear to discourage species diversity but are, simultaneously, preferred by *Microspora willeana* and *Stigeoclonium tenue*, respectively.

The specific relationship between the colonized surface and a colonizing algal species in a community is complex, with various physical factors and processes involved in determining the success of that species' colonization. The interaction of these factors at different length scales, as determined by the dominant feature size of the surface, explains the complexity in colonization characteristics observed for individual species and for the algal community overall. Of primary importance is the basic relationship of the surface area versus diversity as a factor. In general, increasing surface roughness complexity results in an increasing interfacial area ratio (S_{dr}), where the textured surface area increases relative to the cross-sectional area as a fractal dimension[81]. Increased surface area provides more overall sites for attachment of individual cells, evoking the well-known species-area curve in which species number increases as a power function of the

area[82,83]. In this study, however, because of the close packing of the hemisphere roughness elements, the interfacial area ratio is effectively constant for all printed surfaces except the smooth condition. Thus all effects of surface roughness condition on diversity or on individual species variation is a result of interactions mediated by the surface itself, with the subsidy of increased area an equitable factor for all over the smooth condition itself. When surface roughness elements are present, the specific relationship between colonizing cells and the surface is mediated by the hydrodynamics at the surface. Different shape features and sizes will affect the velocity gradient at the boundary layer, affecting the turbulence of the overlying flow and establishing the pattern of quiescent zones at the surface. A colonizing cell must fit within the quiescent zones and have enough contact with the surface for attachment, so the size of the colonizing cell is a factor as well. For example, the size for colonizing zoospore cells of *Microspora willeana* is on the order of 10-15 μm[84]. At that scale, cells can find attachment on smooth surfaces and smaller features, where quiescent zones exist in the velocity boundary layer or in interstitial spaces of the features. Cells of this size, however, cannot find attachment in larger feature sizes, where perhaps more turbulence occurs in the boundary layer that induces drag forces on the cell to overwhelm attachment forces. The colonization pattern for *Stigeoclonium tenue* suggests a different colonizing cell configuration, in the form of asexual reproduction from filament fragments, with a diameter of 10-20 μm and a length many times that[85]. Such a cell geometry might have success at attachment at very small feature sizes, where sufficient contact area between the cell and surface roughness elements is made, and very large feature sizes, where quiescent zones in the boundary layer may be on the size order of these cell sizes, leaving surface features in the mid-range scale with lower attachment and colonization of this particular species. More study of these dynamics via cell attachment force and fluid dynamic modeling is warranted.

6. Experiment#2: Impact of surface roughness profile height and interstitial space on biomass under controlled bioreactor conditions

The primary objective of this study is to investigate the effect of different topographic height and interstitial spaces on benthic algae biomass in a laboratory-based bioreactor to explore whether optimal value of certain surface topography exists. The methodology consisted of designing and fabricating 24 growth plates, each with four sections with different surface topographies, using polyjet 3D printer, and the 3D-printed patterns were used to produce growth plates in clay. The clay plates were then placed in a laboratory-based pilot scale bio-cultivator and exposed to a mixed culture of benthic algae for three weeks. After collecting tiles, the biomass was carefully harvested in each section, oven dried and then weighed to find the exact amount of algae biomass per each section. Statistical analyses were conducted to confirm the effect of surface topography on biomass amount of benthic algae. Also, photographs were taken daily basis from tiles to find growth rate per sections.

Broadly, the methods in this experiment involved designing and 3D printing a growth plate to serve as a pattern to replicate plates with inert clay and then placing them in a laboratory cultivator for three replications. The reason for using clay plate in lieu of 3D-printed polymers in this experiment is that clay will act as more neutral material in interaction with algal biofilms than polymers, which will have some chemical material with it.

6.1 Materials and Methods

The pattern for plates were designed in Solidworks® and fabricated with acrylic polymer-based Stratasys® Objet30 3D printer with 28 µm layer thickness. A square plate (105 mm x 105 mm) with four equal sections (52 mm x 52 mm) and 1 mm space between each section was designed with hemispherical surface features of increasing scale. One section was ideally smooth (Sa=1.19

μm) while the remaining three sections had a pattern of adjacent hemispheres of average area peak to valley (R_z) of 500 μm, 1000 μm, and 2000 μm respectively. Figure 20 shows the computer model with the corresponding fabricated version of growth plate used in this experiment.

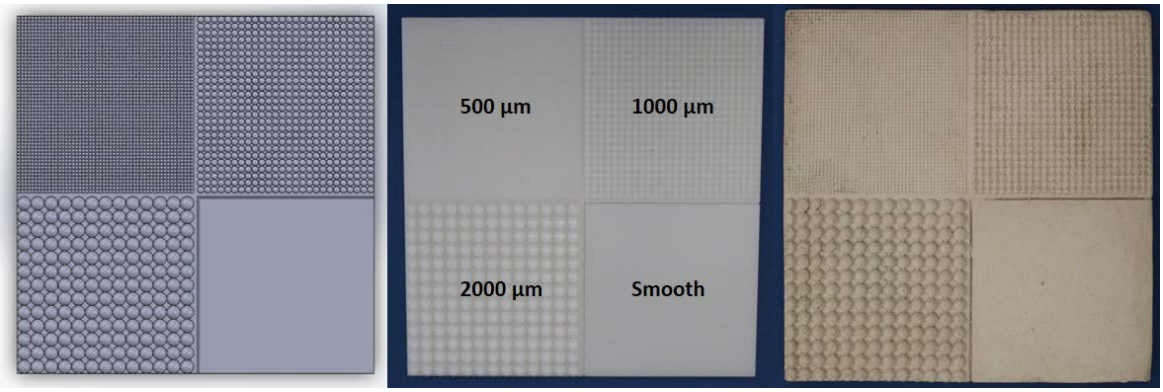

(a) **(b)** **(c)**

Figure 20. (a) Computer Model, (b) 3D-printed growth plate, and (c) fabricated clay plate

The surfaces of the plates were scanned with a 3D axial chromatic (non-contact) profilometer (Nanovea ST-400, Irvine, CA) with 20 nm resolution in the vertical direction. Figure 21 shows the 3D view and the 2D line scan of the surface topography of 500 μm section. The fabrication dimensional error was less than 1% for all the areas.

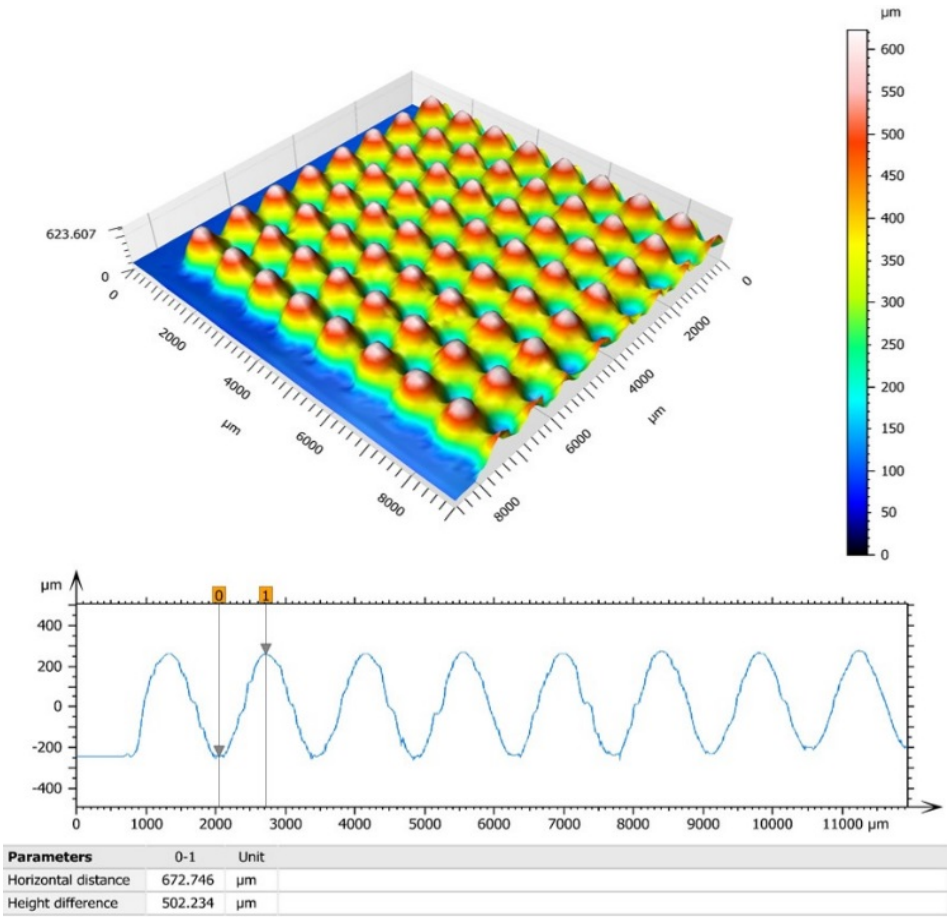

Figure 21. 3D view and 2D profile of the 500 µm section.

The pattern made with the 3D printer was then taken to the 3-D Arts Studio in the Department of Art at Auburn University for replication in clay. The clay formulation contained: Tile #6 clay 40%, Hawthorne fire clay 25%, OM4 ball clay 10%, Custer feldspar 15%, Talc 3%, and Silica 7%. The clay was formulated to have controlled porosity and molds were made by slurry hand-pressing. After that, 24 tiles were cast and fired in the kilns at this facility. The clay firing cycle lasted 12 hours per batch with a subsequent cooling cycle of 15 hour duration.

For each replication, eight plates were placed in a bench-scale benthic algal cultivator (Figure 5) in the laboratory[71] in two lines in which each line had 4 plates and each plate had different orientation than others (Figure 22). The cultivator is a shallow trough in which attached benthic

filamentous algae are typically grown on polypropylene screen substratum placed in the bottom of the trough. Water pumped from a reservoir continuously flows over the substratum in a thin layer (1-2 cm deep) and returns to the reservoir where a submersible pump recirculates it. A tipping bucket (wave surge bucket) mechanism provides a periodic wave surge that helps stimulate the growth of benthic algae and disperse the nutrients. The cultivator was operated continuously at a flow rate of 45 L min-1 with a tipping frequency of 4 min^{-1}. Light was provided continuously by two 400 W metal halide grow lamps (Virtual Sun®, La Verne, California) located directly above the center of the cultivator. Figure 23 shows lights illumination maps over the bio-cultivator before and after changing the height and location of lamps to get experimentally optimum light intensity for algal turf. The plates were fixed to the substratum screen with silicon and remained in place for 21 days per replication over three replications.

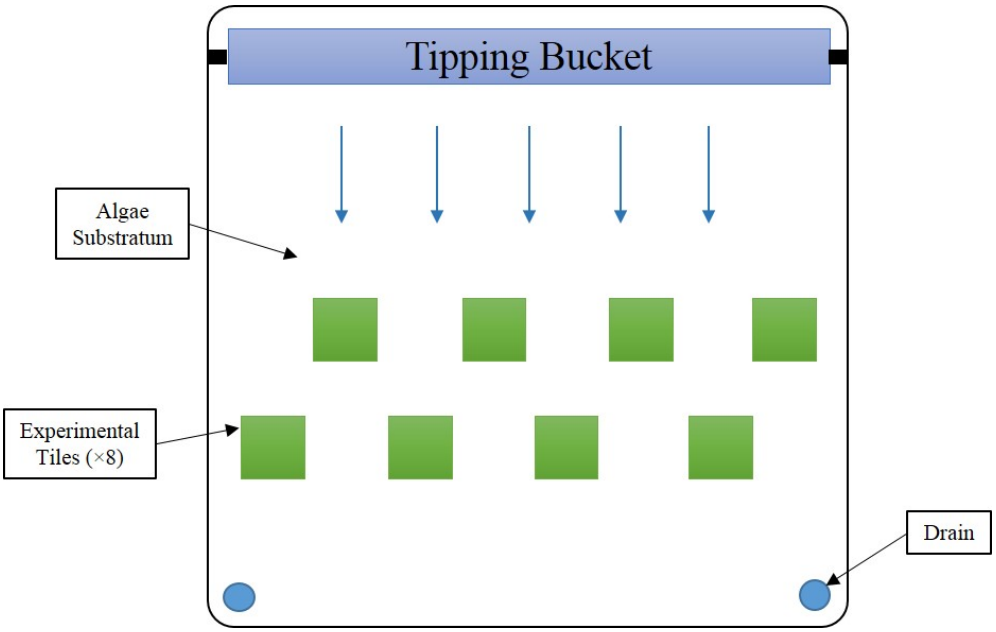

Figure 22. Schematic plan view of tiles location in bio-cultivator

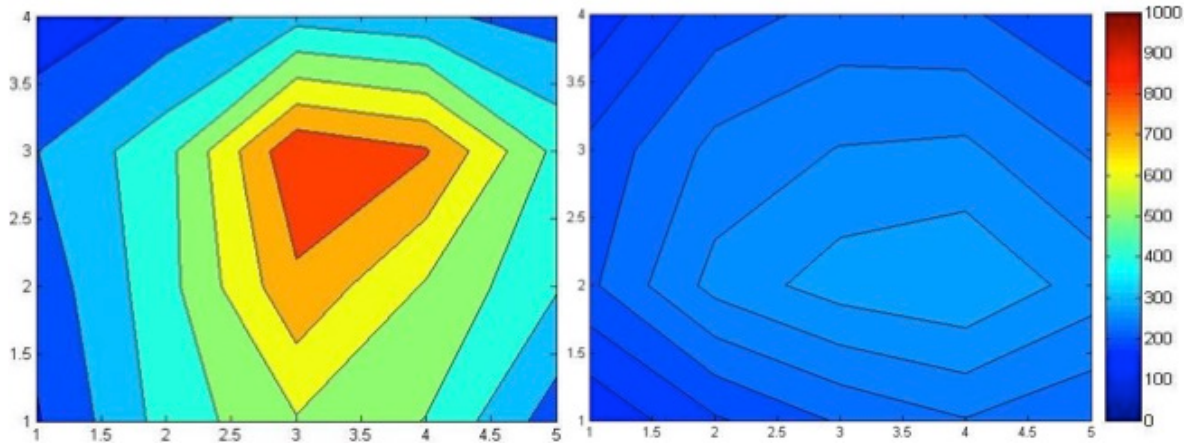

(a) **(b)**

Figure 23. Light illumination map for (a) before calibration and (b) after calibration of lights (lux)

The cultivator was inoculated with a mixed algal community sampled from local streams that was dominated by filamentous benthic algae. The cultivator was dosed daily with commercial F/2 media (Pentair Co., Apopka, FL) at the recommended loading concentration rate (1 ml nutrient per 1 gallon of water). In addition, pH, temperature, and conductivity of the water were measured daily basis with a handheld combination pH/EC probe (HI 98130, Hanna Instruments, Woonsocket, RI) and averaged 7.66 ±0.16, 74.49 ±0.89 ^{o}F, and 0.59 ±0.08 mS cm^{-1}, respectively. Both dissolved P and N concentrations were measured as PO_4-P: 258.33 ±63.36 ppb and NO_3-N: 2.42 ±0.99 ppm, respectively, using Insta-Test testing pads (LaMotte Co., Chestertown, MD).

For each replication, photographs were taken with a camera of each tile every other day during experiment (Figure 24). For each replication, tiles were removed after 21 days and each section within each plate was harvested separately with several methods. These included vacuuming, mechanical scraping, and washing with low-pressure distilled water. The biomass collected from each section was stored in vials after harvesting each section. Drying process was included first weighing aluminum containers and then pouring each vial's content in one container to oven dry

at 105°C and then weighing dried samples with containers to get biomass dry weight[72]. The biomass samples then analyzed with parametric tests to understand the impact of surface texture profile height and interstitial spacing on biomass.

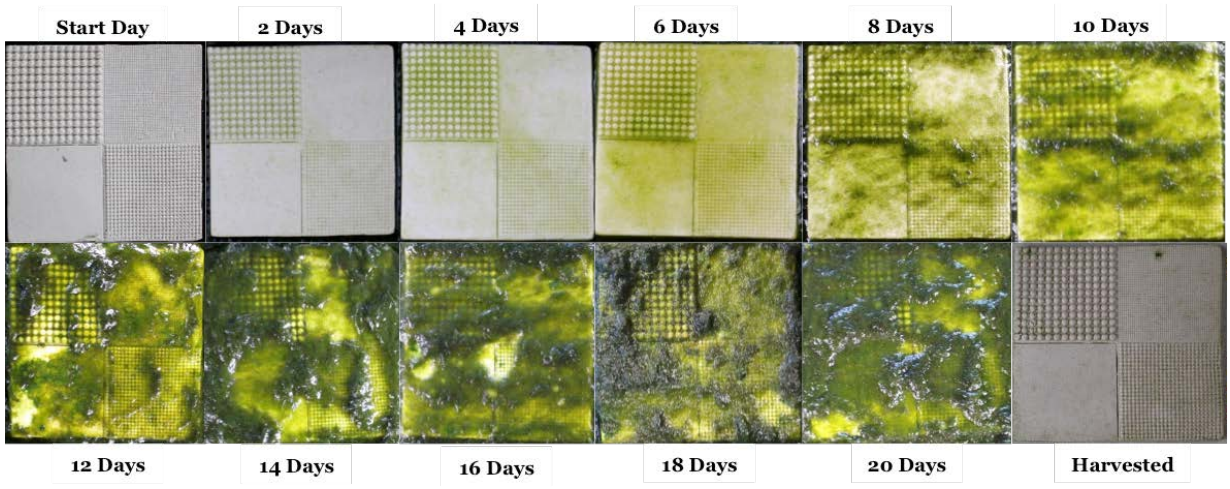

Figure 24. Photographs of one tile during one replication

The species identification was conducted via digital microscopy (400X to 1000X) using a Motic optical microscope (Motic Corp., Richmond, BC). Samples were taken and preserved in vials per weekly basis to analyze and identify algal species. The microscopic sample preparation included a thorough mixing of the vial, which was then transferred to a glass slide for observation. Three subsamples each with a volume of 0.063 ml were drawn from each vial and 20 micrographs were taken from each subsample. The algae observed in the micrographs were keyed to at least the genus level using standard identification keys[76]. The most dominant species in all subsamples from all samples was *Mougeotia* (Figure 25).

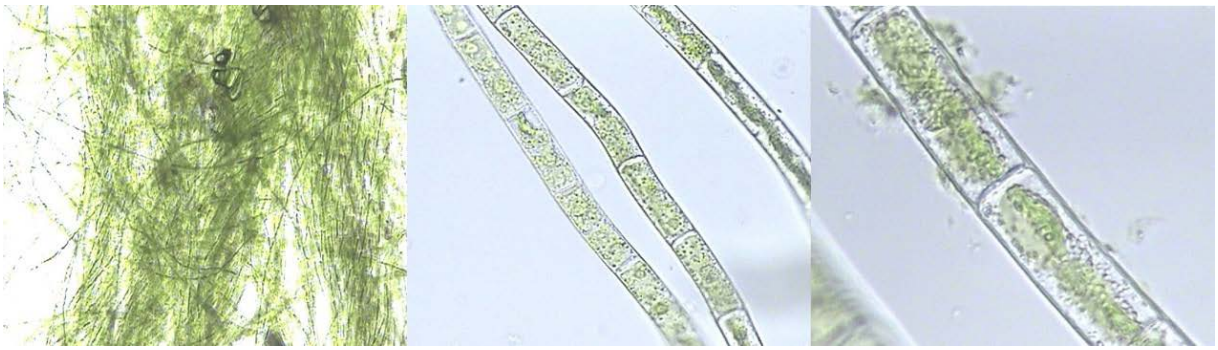

(a) **(b)** **(c)**

Figure 25. Microscopic view of Species *Mougeotia*, (a) 100X magnification, (b) 400X magnification, and (c) 1000X magnification

6.2 Results

The statistical analysis performed on algae biomass data per topographic sections were first analyzed for underlying ANOVA assumptions, including a test for equal variance and analysis of residual plots. After checking conformity of ANOVA assumptions, parametric statistical tests were employed. This included the two stage nested design using Minitab balanced ANOVA test followed by paired t-test for pairwise comparison. These analyses were used to indicate best surface topography for attachment and growth of benthic algal biofilms.

Harvested biomass from each section for each replication was measured after drying process (Appendix II). Figure 26 shows average biomass main effect per each section in each replication with a multiple data series graph.

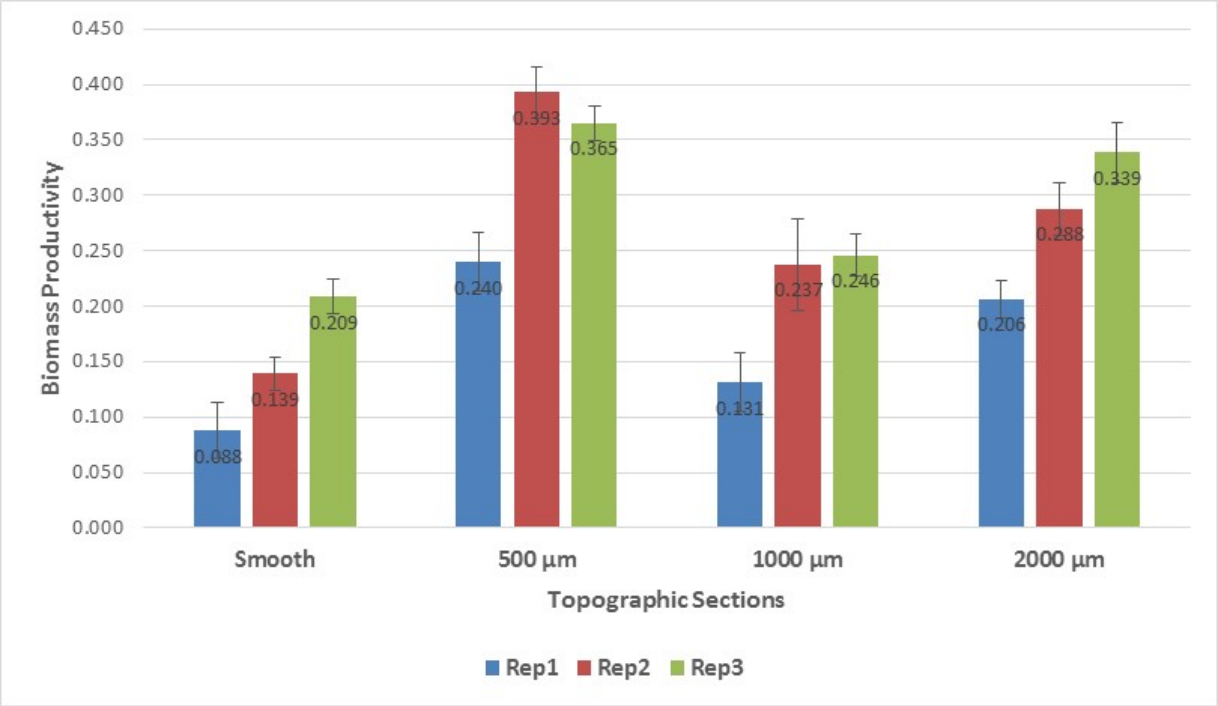

Figure 26. Biomass productivity for all replications

Statistical design for this experiment is two stage nested design, where there is generally four levels of topographic sections nested under replications and eight observations per each section (Figure 27). Both replication and topographic section are assumed fixed factors because they are not sampled randomly.

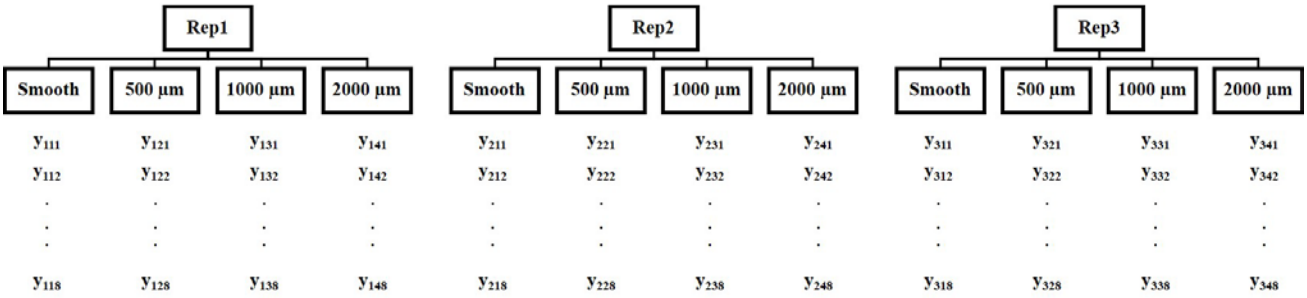

Figure 27. The two-stage nested design for the experiment[86]

The data were first analyzed for conformity of the ANOVA assumptions by a test for equal variance and analysis of residual plots. Figure 28 shows the result for equal variance test on total

biomass in Minitab, which does not show significant differences between variances for biomass. Thus, the hypothesis of equal variances cannot be rejected.

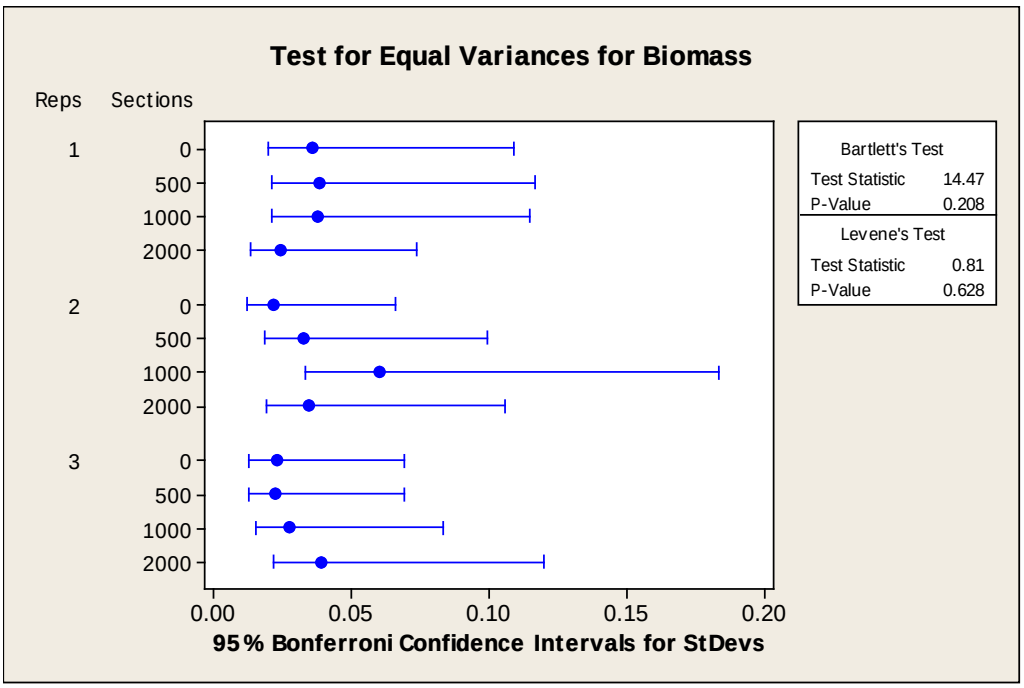

Figure 28. Test for equal variances between sections

Also a test for residuals for ANOVA analysis on biomass results shows normal results with only one outlier. Figure 29 shows all the plots and histograms for residual analysis on biomass results by Minitab. Further analysis of the biomass data showed that there is no significant difference between the three replications of this experiment (p-value = 0.149).

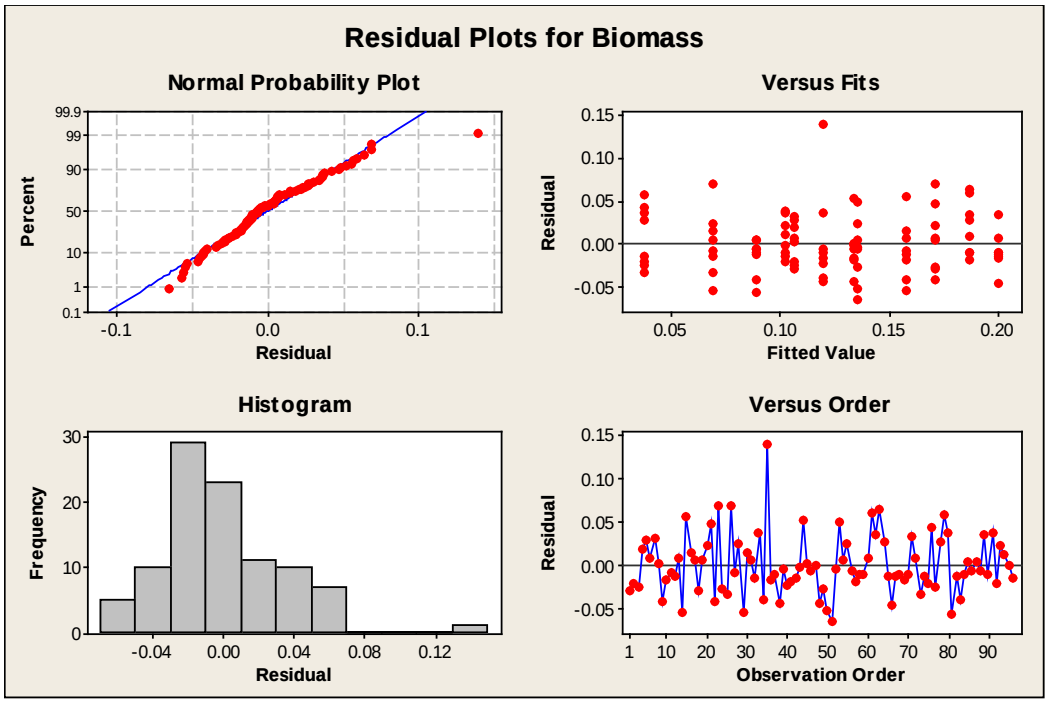

Figure 29. Residual plots for biomass data

After checking conformity of ANOVA assumptions, parametric statistical analysis employed to analyze the two-stage nested design for the experiment (Table 5). This relieve on the assumption of topographic designs nested within replications. Results of this analysis are listed in table 5 with the statistical significance level of $\alpha = 0.05$.

Table 5. Nested ANOVA results for algae biomass

Source	DF	SS	MS	F	P
Replications	2	0.0749	0.0374	2.374	0.149
Topographic Sections	9	0.1419	0.0158	13.175	0.000
Error	84	0.1006	0.0012	-	-
Total	95	0.3174	-	-	-

Results of statistical analysis for algae biomass shows significant difference between topographical sections used in the experiment. Paired t-test were employed for all possible combinations of two sections (six separate tests) to find the most effective topographic section for benthic algal spores to attach and colonize. Results of paired t-test with 95% of confidence interval for mean difference

between all topographic sections showed that section with average peak-to-valley (R_z) of 500 µm has the best attachment and growth of benthic algae between all sections. Figure 30 shows the main effect plots of algae biomass for all three replicates.

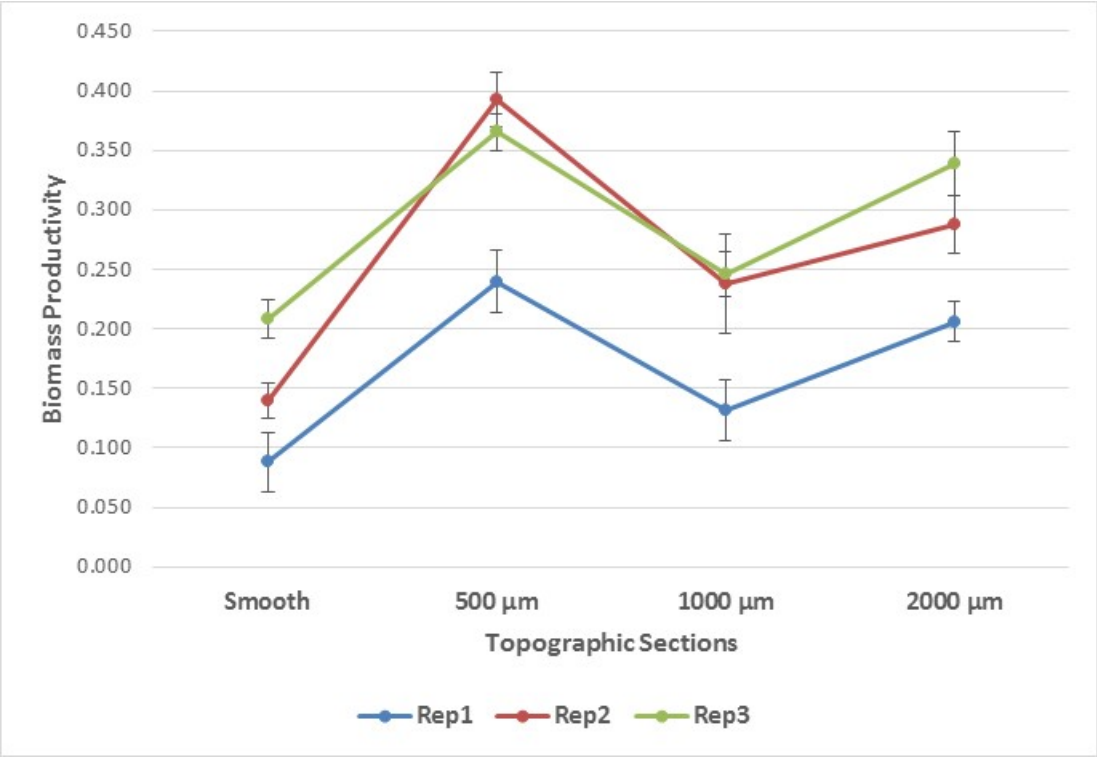

Figure 30. Main effect plots of algae biomass productivity

6.3 Discussion

In this investigation the laboratory-based algal turf scrubber system had a community of mostly filamentous benthic algae (most commonly *Mougeotia sp.*). Results showed a notable effect of surface topography on attachment and colonization of filamentous benthic algae in this system which was not a trend from smoothest to roughest topography, generally. These benthic algal species showed significantly more abundance in surfaces on 500 µm section and after that in 2000 µm than others. The interaction of the various species in the community with the different surface topographical feature size is not related to different section's surface area. Figure 31 perfectly shows that surface area for all different topographic sections is the same. That means the difference

between amount of benthic algae attached and colonized is not related to difference between surface areas.

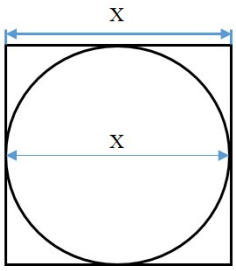

$$X^2 - \pi\left(\frac{X^2}{4}\right) + 2\pi\left(\frac{X^2}{4}\right) = X^2\left(1 + \frac{\pi}{4}\right)$$

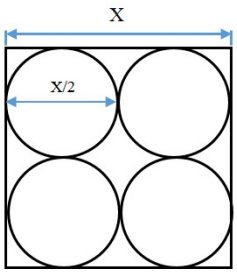

$$X^2 - 4\pi\left(\frac{X^2}{16}\right) + 4\left(2\pi\left(\frac{X^2}{16}\right)\right) = X^2\left(1 + \frac{\pi}{4}\right)$$

Figure 31. Surface area comparison

As it was mentioned before, the specific relationship between the colonized surface and algal species colonizing them in laboratory-based algal turf scrubber is a complex process with so many factors. Also, just similar to previous study, because of close packing of hemispheres in all topographic sections, except smooth surface section, interfacial ratio (S_{dr}) is effectively fixed. The size for colonizing zoospore cells of *Mougeotia sp.* is on the order of 10-15 μm[87], which at this scale, cells can find attachment on smooth surfaces and smaller features where inactive and more inert zones at boundary layers are existing. The cell size is also in the order of *Microspora willeana*, mentioned in previous experiment, which means boundary layer effect, caused by different feature sizes, could be an important factor for colonizing cells to find inert zones for attachment and colonization. This study showed that 500 μm sections is statistically the best feature size for colonizing of benthic filamentous algal community (mostly *Mougeotia sp.*) which could happen because of velocity in boundary layer or interstitial spaces of 500 μm features. For

larger filament parts of filamentous algae community, the colonization pattern would be different than colonizing cells because of the considerable difference in length. Bigger surface feature area such as 2000 μm section could be a better environment for such a broken filament parts for reproduction at boundary layer with quiescent zones in their size order. These analyses needs further experimentation on isolated reactors with fluid dynamic modeling and matched nutrients and other situation as a future study.

7. Experiment#3: Study on 3D-printed polymers under collision

Based on the application of 3D-printed polymer surfaces, there is always a chance of collisions with other objects. Therefore, it is necessary to have an understanding of the effect of such collisions on the integrity of the surface as it may affect the productivity of the algal system. Behavior of these materials under dynamic contacts especially the history of contact force during collision can help with more efficient mechanical designs. However, mechanical properties of the rapidly evolving material set available for 3D printing is somewhat limited and quickly rendered obsolete.

In this effort, the focus is on the dynamic behavior of traditional polymer material (e.g. PLA, ABS, and acrylic) used in additive manufacturing during collision with a rigid body. This includes both the motion of objects before and after the impact and permanent plastic deformations on the weaker materials, which is the 3D printed material in this case. Both dynamic and static behavior of the material were accounted in the contact force. Due to ease of implementation, the Stronge formulation[67] for the contact force is used for the static phase of the force. For the dynamic behavior of the force, a nonlinear simple damper[62] has been incorporated to the Stronge's formulation.

7.1 Materials and Methods

In order to conduct this experiment, a square-shaped part with four anchor points in corners was designed in Solidworks® with dimensions of 76 x 76 x 15 mm. The equipment used to fabricate the parts included BigRep ONE® for Industrial PLA and Ultra PLA with FDM technology, Makerbot® for PLA with FDM technology, Stratasys® Objet30 using Verowhite® acrylic with Poly-jet technology, and Cube® using ABS with FDM technology. The same printing orientation pattern with 100% infill rate has been used for all of the methods.

The experiments have been designed in order to measure permanent deformation of the plastic surface after each impact and motion of the rod. A rounded end stainless steel rod with length L = 304 mm, diameter D = 8.8 mm, and mass m = 0.567 kg modulus of elasticity of E_s = 212 GPa and yield strength of S_{ys} = 750 MPa was used. Flat surfaces were 3D-printed and then finished with abrasive papers to the smoothest possible surface (R_a between 0.2 to 0.4 μm). The material properties of 3D-printed materials are listed in Table 6.

Table 6: Properties of materials used in experiment

Type	Trade name	E (GPa)	S_y (MPa)	Poisson Ratio (ν)
PLA	Industrial	3.2	37	0.360
PLA	Ultra	2.3	31	0.360
Acrylic	Vero White	2.0	60	0.375
PLA	Makerbot	3.4	48	0.360
ABS	Cube Tough	1.8	28	0.350

The schematic of the experimental setup is shown in Figure 32. The 3D-printed part was fixed on a massive metal flat, which itself is fixed to the table. A magnet device is used to drop the rod vertically from different heights, H, between 25 mm to 520 mm. A four-head flexible microscopy illumination light with a 1000 W projector were used to capture clear videos with minimal noise during the impact.

Each impact was analyzed with two techniques: optical profilometry and image processing. To capture motion of the rod before, during, and after the impact, a high-speed camera capable of recording up to 200,000 frames per second (fps) was used. The profile of each deformation was measured with an optical profilometer after each impact. The maximum depth in the deformed region was defined as permanent deformation.

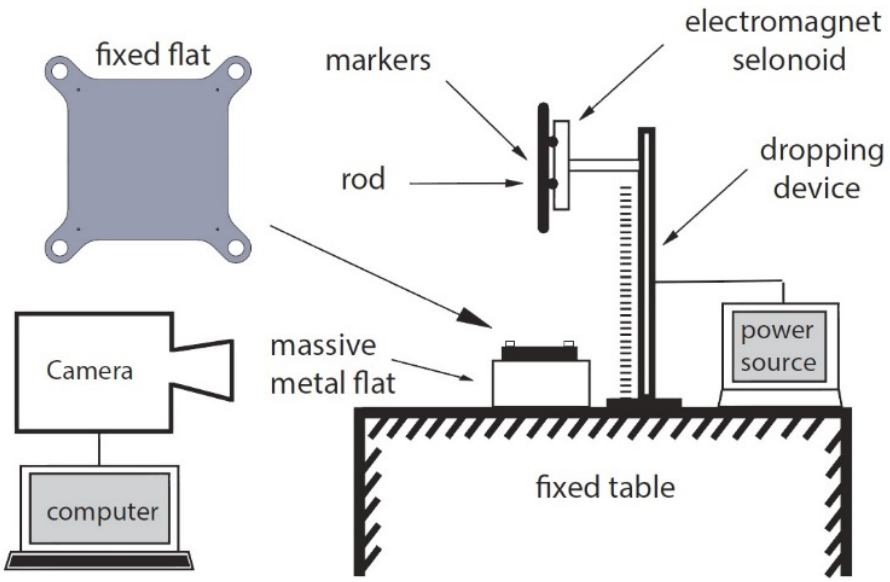

Figure 32: Schematic view of the normal impact

7.1.1 Surface measurement

3D-printed parts and rod samples were polished so that the average roughness of the 3D-printed surfaces ranged between 0.2 to 0.4 µm. After each impact test, parts were scanned by optical profilometer to get 3D images and 2D profiles from deformed regions (Figure 33). The average of three cross sections of the deepest points in deformed region was used to measure the permanent deformation. Distance between scanned points in X direction and profiles in Y direction was 3 µm.

In this study, for each 3D-printed part, 36 experiments for 3 specimens were done at 12 different initial velocities from 0.5 m/s to 4.0 m/s. The coefficient of restitution and the permanent deformation are calculated for each initial velocity by averaging data from three experiments.

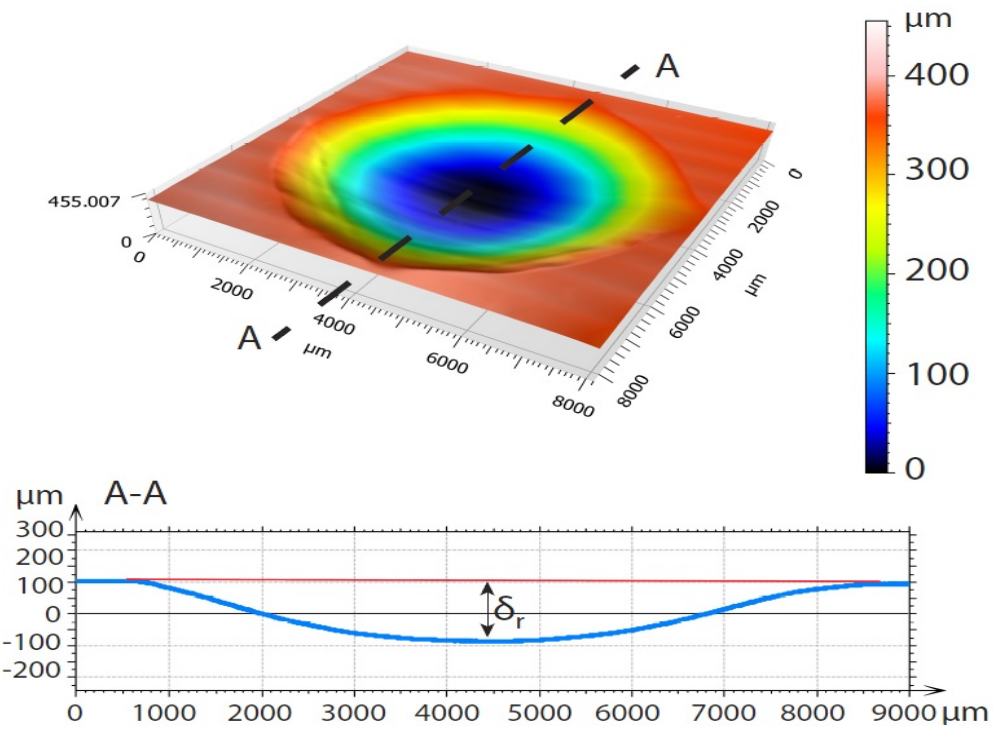

Figure 33: Aerial height map and 2D profile of permanent deformation of one impact

7.1.2 Image processing

The motion of the rod and the radius of curvature of the tip of the rod have been calculated using image-processing techniques. The radius of the curvature is needed in the contact force formulation while the motion of the rod is required to calculate the coefficient of restitution. The following subsections are explaining the process in detail.

7.1.2.1 Radius of curvature of the rod

Radius of curvature of the tip of the rod is an important factor in our contact force formulation. Therefore to measure this parameter accurately image-processing technique has been used. A 12 mega pixel image from the tip of the rod has been used for the measurements. Figure 34(a) shows the picture from the tip of the rod. The boundary of the rod has been identified and an eight-order polynomial has been fitted on the boundary (Figure 34(b)). The radius of the curvature of the rod has been derived from the polynomial as, R = 9.7 mm.

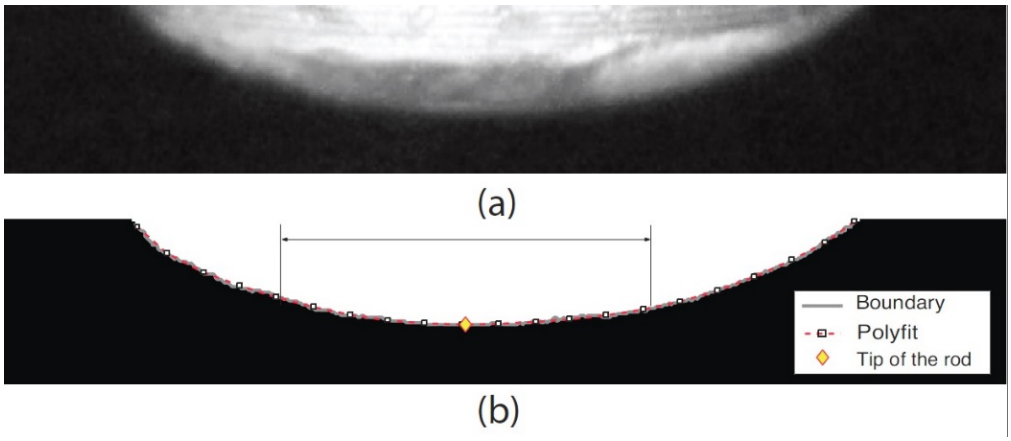

Figure 34: The original picture (a), and processing image (b) for the tip of the rod

7.1.2.2 Motion of the rod

The velocity of the rod during the tests is required for the model. Each impact collision has been recorded using a high speed camera at 10,000 frames per second. Every part of the rod but the tip has been painted in black. Two white adhesive strips have been attached to the rod for use in image processing (Figure 35(a)). In the image processing each frame has been threshold to pure white and pure black (Figure 35(b)). In order to track the motion of the rod, the positions of the three edges from the white strips can be calculated. To find the position of the edges, the first derivative of the vertical direction can be used. Each pixel has a gray value, $g(x, y)$, which is an 8-bit number with x and y as the horizontal and vertical axis respectively. Let the frame size be $m \times n$ where m and n are the number of rows and columns respectively and the $\chi(y)$ be a coefficient that we defined as:

$$\chi(y) = \sum_{x=1}^{n} \frac{\partial g(x,y)}{\partial y} \tag{2}$$

$\chi(y)$ is the sum of vertical first derivation of $g(x, y)$ for all pixels in each row. Figure 35(c) shows $\chi(y)$ for the same frame as Figure 35(a). The three large peaks show the position of the edges shown in Figure 35(b), three horizontal lines. The average positions of these three peaks have been used

to calculate the position of the rod.

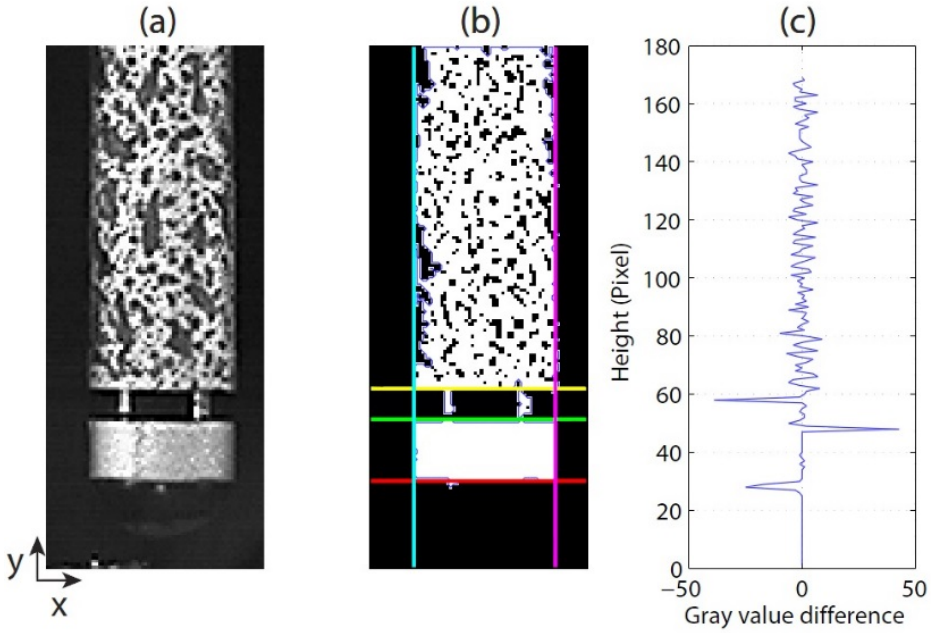

Figure 35: (a) the image processing procedure of the rod during one of the impacts. (a) The original frame. (b) Pure black and white image. (c) χ(y) for (b), sum of the first order vertical derivation.

Figure 36 shows the vertical position of the rod during an impact test. The minimum point shows the instant the impact happens. To find the velocity before and after the impact two lines have been fitted on the data after and before the collision (Figure 36). The slopes of the lines show the velocities. For this specific experiment the initial vertical velocity is, v_i = -3.258 m/s, the final vertical velocity is, v_f = 1.794 m/s and coefficient of restitution, e = 0.550.

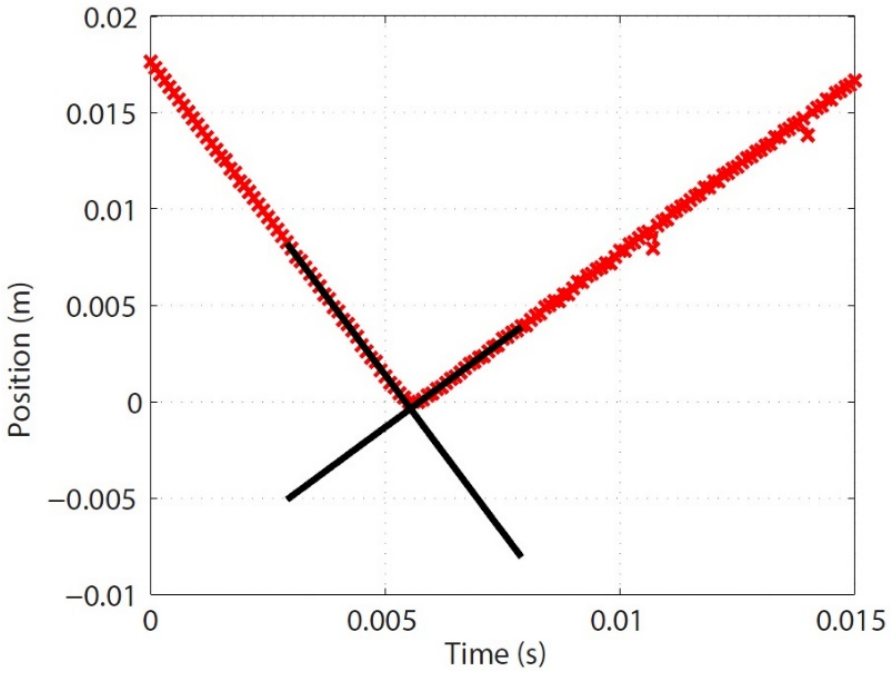

Figure 36: Vertical position of the rod during a test for industrial PLA (initial velocity, vi = -3.258 m/s)

Conventionally, the coefficient of restitution is defined as the ratio between the rebound and initial velocities (i.e. Newton's definition) or as the ratio between the restitution and compression impulses (i.e. Poisson's definition[57]) has been used to account for the energy loss during the impact. The coefficient of restitution is easy to measure experimentally but has the lack of information for the history of the contact force during impact. Recently it was shown that permanent deformations after the impact can be used to achieve a better understanding of the history of the contact force during impact[61,88].

7.1.3 Theoretical Modeling

Figure 37 shows schematic of the normal impact of a rod with a flat. The contact force is applied on the tip of the rod in the Y-direction. The equation of motion for the rod is:

$$m\ddot{\delta} = F_n - mg \tag{3}$$

Where δ is the displacement of the tip of the rod, which is equal to the deformation on the flat, m

is the mass of the rod and g is the gravitational acceleration. The equation of motion can be solved numerically to simulate the motion of the rod during the impact.

The contact force F_n can be written as:

$$F_n = F_s(\delta) + F_d(\dot{\delta}) \tag{4}$$

Where F_s and F_d are accounting for the static and dynamic behavior of the material, respectively. For F_d during the compression phase we propose the simple nonlinear damper equation:

$$F_d(\dot{\delta}) = b\dot{\delta}^{1.5}\frac{\dot{\delta}}{|\dot{\delta}|}. \tag{5}$$

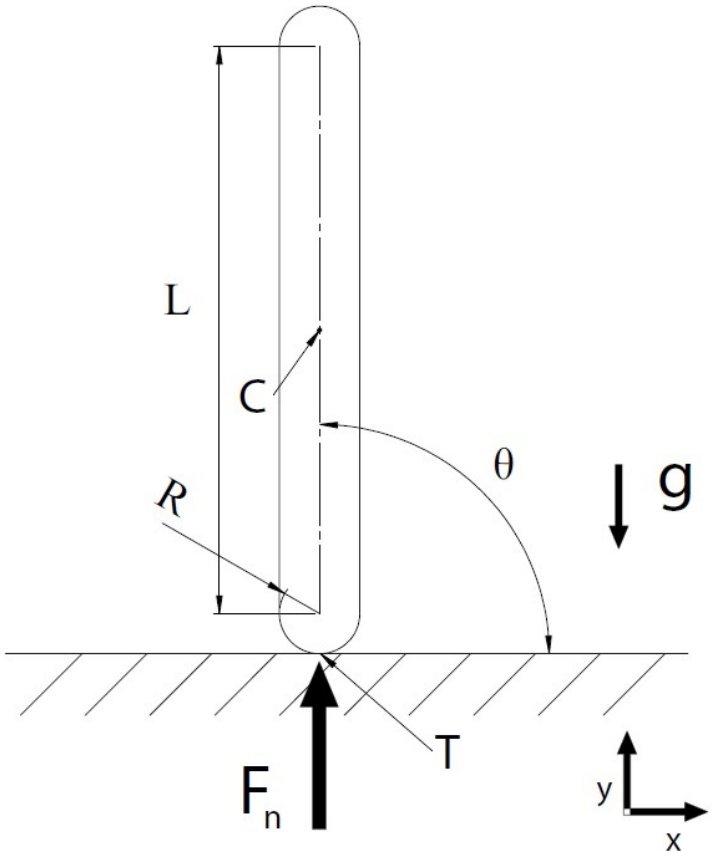

Figure 37: Schematic of the normal impact

For the F_s, the Stronge's formulation has been used[67]. The static contact force is divided into two main phases, the compression and the restitution. The compression phase starts when the collision starts and continues until the relative normal velocity of the objects is zero. At this instant the

restitution phases starts and continues until the displacement of the tip, δ gets to permanent deformation, δ_r.

7.1.3.1 Compression phase

The compression phase divides into three sub-phases, fully elastic, elastic-plastic and fully plastic phase. For the fully elastic phase Hertzian theory[89] has been used as following:

$$F_s = \frac{4}{3} E^* R^{*0.5} \delta^{1.5} , \tag{6}$$

where E^* is the effective modulus of elasticity and R^* is the effective radius of curvature and can be calculated as:

$$E^{*-1} = \frac{\left(1-v_r^2\right)}{E_r} + \frac{\left(1-v_f^2\right)}{E_f} \ , \ R^{*-1} = \frac{1}{R} + \frac{1}{R_f} , \tag{7}$$

Where v_r and v_f, R_r and R_f, and E_r and E_f are the Poisson's ratio, radius of curvature and modulus of elasticity of the rod and the flat, respectively. For our case $R_f = \infty$ and $E_r = \infty$, therefore $R^* = R_r$ and $E^* = E_f/(1 - v^2)$. The elastic phase continues until $\delta = \delta_y$, where δ_y is the deformation in which the yield starts:

$$\delta_y = R^* \left(\frac{3\pi v_y S_y}{4E^*}\right)^2 , \tag{8}$$

Where the S_y is the yield strength of the flat.

The elastic-plastic phase starts at $\delta = \delta_y$. The contact force is calculated from Stronge's[67] as:

$$F_s = F_y \left(\frac{a}{a_y}\right)^2 \left[1 + 0.67 v_y^{-1} ln\left(\frac{a}{a_y}\right)\right], \tag{9}$$

Where a/a_y and F_y can be calculated as:

$$\frac{a}{a_y} = \left(\frac{2\delta}{\delta_y} - 1\right)^{0.5} \ , \ F_y = v_y S_y R^{*2} \pi \left(\frac{3\pi v_y S_y}{4E^*}\right)^2 \tag{10}$$

The fully plastic phase starts at $\delta = \delta_p = 84\delta_y$, and δ_p is the instant in which the fully plastic phase starts. The fully plastic contact force is:

$$F_s = \frac{2.8F_y}{v_y}\left(\frac{2\delta}{\delta_y} - 1\right) \tag{11}$$

7.1.3.2 Restitution phase

The restitution starts at $\dot{\delta} = 0$, at this instant $\delta = \delta_m$ and $F_s = F_m$. The restitution phase continues until $\delta = \delta_r$, and δ_r is the permanent deformation. The contact force for the restitution phase follows the Hertzian theory and can be calculated as:

$$F_s = \frac{4}{3}E^* R_r^{*0.5}(\delta - \delta_r)^{1.5}\,, \tag{12}$$

And

$$R_r^* = \left(\frac{4}{3}E^* F_m\right)^2 \frac{1}{(\delta_m \delta_r)^3}\,. \tag{13}$$

The permanent deformation has been measured from the experimental results for each material presented in the following section. The general empirical equation for the permanent deformation is proposed as:

$$\frac{\delta_r}{\delta_m} = \lambda_1 \left(\frac{\delta_m}{\delta_y}\right)^{\lambda_2}\,, \tag{14}$$

Where λ_1 and λ_2 have been found from the experiments for each material. For the dynamic force, $F_d(\dot{\delta})$ during the restitution phase we propose the following formula:

$$F_d(\dot{\delta}) = b\left|\dot{\delta}\right|^{1.5}\left(\frac{\delta - \delta_r}{\delta_m - \delta_r}\right)\frac{\dot{\delta}}{|\dot{\delta}|}\,, \tag{15}$$

Which satisfies the boundary conditions during the restitution phase at maximum deformation and at permanent deformation.

7.2 Results and discussion

Figure 38 shows the experimental results for the coefficient of restitution as a function of initial velocity for different 3D-printed materials. Initial velocity for all experiments ranged from 0.5 to 4 m/s. Industrial PLA and VeroWhite Polyjet showed the largest and Ultra PLA shows smallest

coefficients of restitution for most initial velocities. Coefficients of restitution appear to be decreasing with increase in initial velocity. Also it can be seen that the coefficient of restitution is converging to a constant value for higher initial velocities which matches the previous studies in the field of mechanical impact[62,69]. For low velocities, part of the contact region deforms elastically and a part is deforming plastically while for higher velocities almost whole impact regime is under plastic deformation, therefore, more energy will be lost during impact and COR decreases. The same trend could be approximately predicted for COR of each material. The material that can go under higher deformations and stay elastic such as Polyjet should yield higher values for COR, while weaker materials such as ABS and Ultra PLA should result in smaller COR[61,63,65,69].

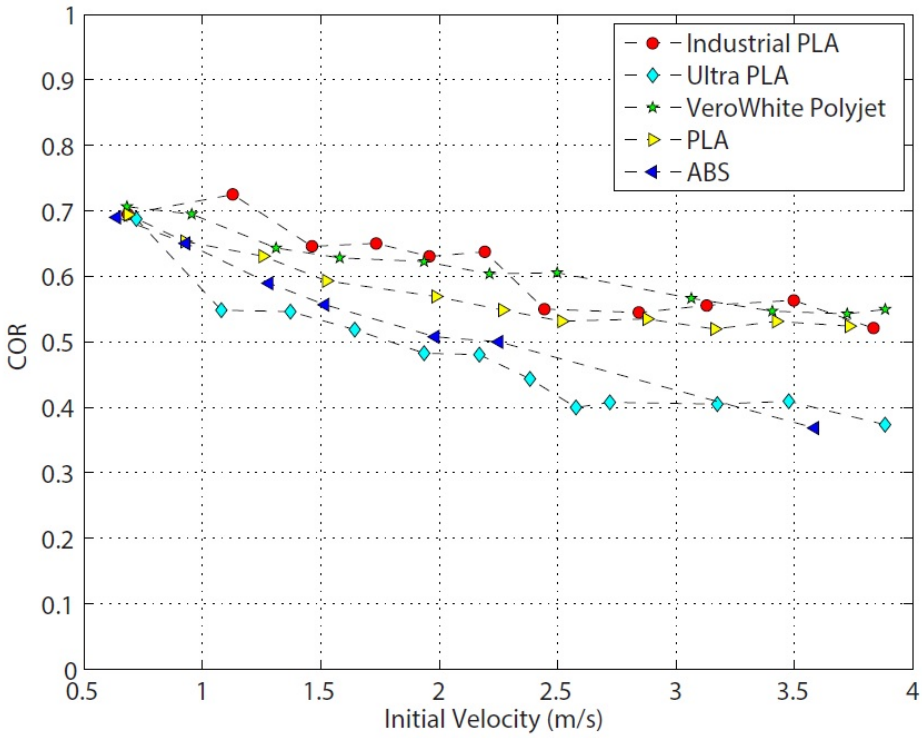

Figure 38. Coefficient of restitution vs. an initial impact velocity.

Figure 39 represents the permanent deformation after the impact as a function of the initial velocity. The permanent deformation increases with the increase of the initial velocity. Cube ABS

and then Ultra PLA show larger permanent deformations with significant difference compare to other materials. It could also be predicted from the material properties that the Cube ABS with the smallest yield strength deforms more than the other materials. Makerbot PLA and then Industrial PLA show shallower permanent deformations. Same as COR, materials that can be on elastic phase for higher velocities such as Industrial PLA and Makerbot PLA would have less deformation than weaker materials such as ABS and Ultra PLA which for higher velocities their impact regime is mostly under plastic deformation[64,88].

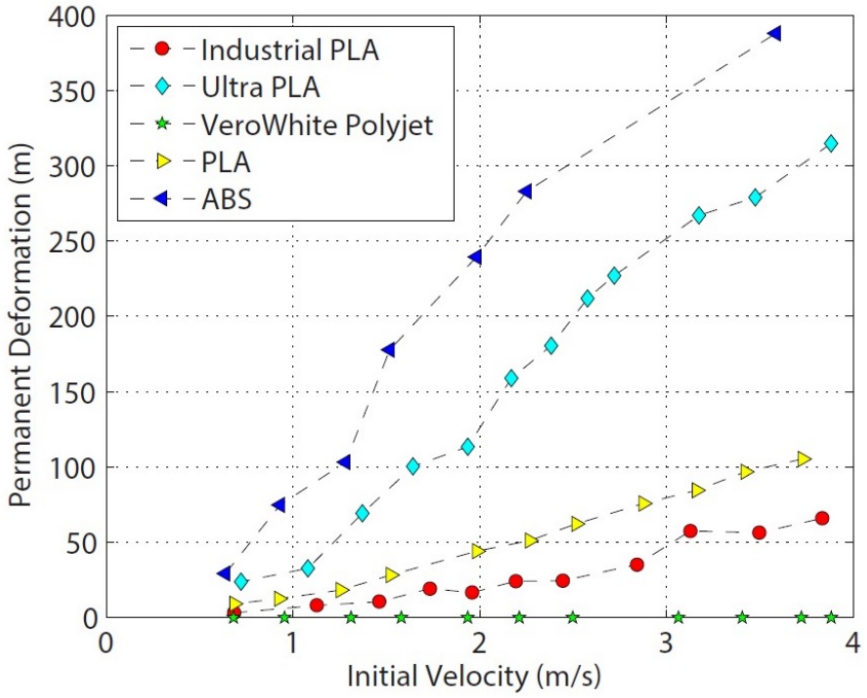

Figure 39. Permanent deformation vs. an initial impact velocity

Permanent deformation for VeroWhite Polyjet were as measured as 10 times smaller than the average roughness (R_a) of the surface, therefore the deformations for this material has been assumed negligible. This would be mostly because of the difference between technologies for printing polymers of Polyjet system and extrusion-based FDM systems for other materials tested in this experiment. In Polyjet, an acrylic photopolymer is projected over the printed object and

curing to its succeeding by ultraviolet (UV) radiation. When the layer has been cured, the tray goes downhill a layer (28 μm) along the Z axis, and this procedure is repeating until the part is accomplished[90,91]. But in extrusion based systems, the part is made by extruding small strings of molten materials to form layers as the material (150-200 μm thickness) becomes hard immediately after extrusion from the nozzle[92]. Based on the nature of the processes it can be concluded that, polyjet based materials would have much stronger bonding between layers than extrusion based materials which have thicker layers with no UV curing process, and then very stronger structure under impact in the range of this experiment's initial velocities. This could make difference between elastic and plastic phase of Polyjet Verowhite with other material in this study, which is almost totally elastic for Polyjet in the range of initial velocities of this experiment. Figure 40 shows a micrograph of a printed part with polyjet system using Keyence VHX-1000 digital microscope with 100x magnification which still does not show the printed layers clearly versus extrusion-based printed part, using same microscope and magnification, which clearly shows the printed layers with less than 4x magnification picture.

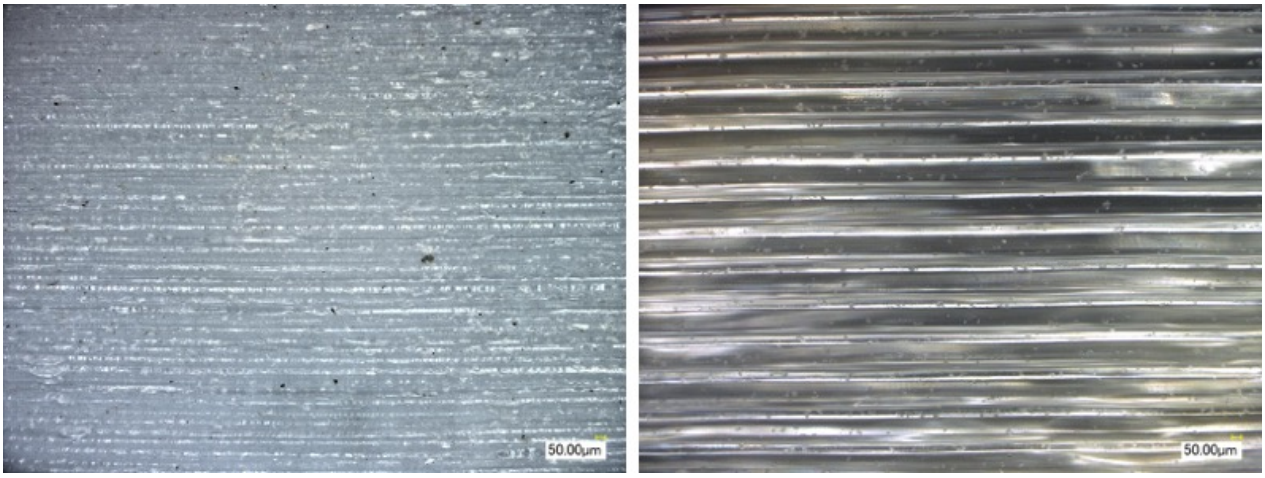

(a) **(b)**

Figure 40. Polyjet printed part (a), extrusion based (FDM) printed part

Using the numerical simulations and the experimental results an empirical equation, Eq. (14) has been fitted for the permanent deformation of each of the materials. First, the experimental results for the permanent deformation, Figure 39, has been used to find λ_1 and λ_2 in Eq. (14). The results for each of the materials is presented in Table 7. Second, the damping coefficient in Eq. (5) for each of the materials has been found, Table 7.

Table 7. Damping coefficient, *b*, (Eq. 5), λ_1 and λ_2 (Eq. 14)

Material	*b* (kg/s)	λ_1	λ_2
Industrial PLA	365	0.000393	1.219
Ultra PLA	550	0.008766	0.817
Polyjet Vero White	496	-	-
Makerbot PLA	535	0.004606	0.786
Cube Tough ABS	410	0.049270	0.514

To calculate the damping coefficient, b, for each of the materials the experimental results of coefficient of restitution for different initial velocities have been used. For each material the nonlinear differential equation of motion for a range of damping coefficient has been solved using the Runge-Kutta numerical integration method. The numerical results then have been compared with the experimental values of COR for all of the initial velocities. The average error between the experiments and the theory has been calculated for each value of the damping coefficient, b, of the corresponding material. The damping coefficient, b, with the least error has been chosen for each of the materials.

Now this will give only one damping coefficient for each material; however, it should be considered that this damping coefficient takes both the value and the curvature of the COR as a function of initial velocity. The damping coefficient cannot be solved for each of the experimental results, because the nonlinear differential equations are irreversible in time.

The results presented in Table 7 along with Equations (3-15) can be used to simulate the impact

for each of these materials. Figure 41 shows the comparison between the results from Table 7 with the experimental data for coefficient of restitution for each of the materials. As it can be seen the proposed model matches the experimental results for all of the materials. The average error between the experiments and the model is less than 5%.

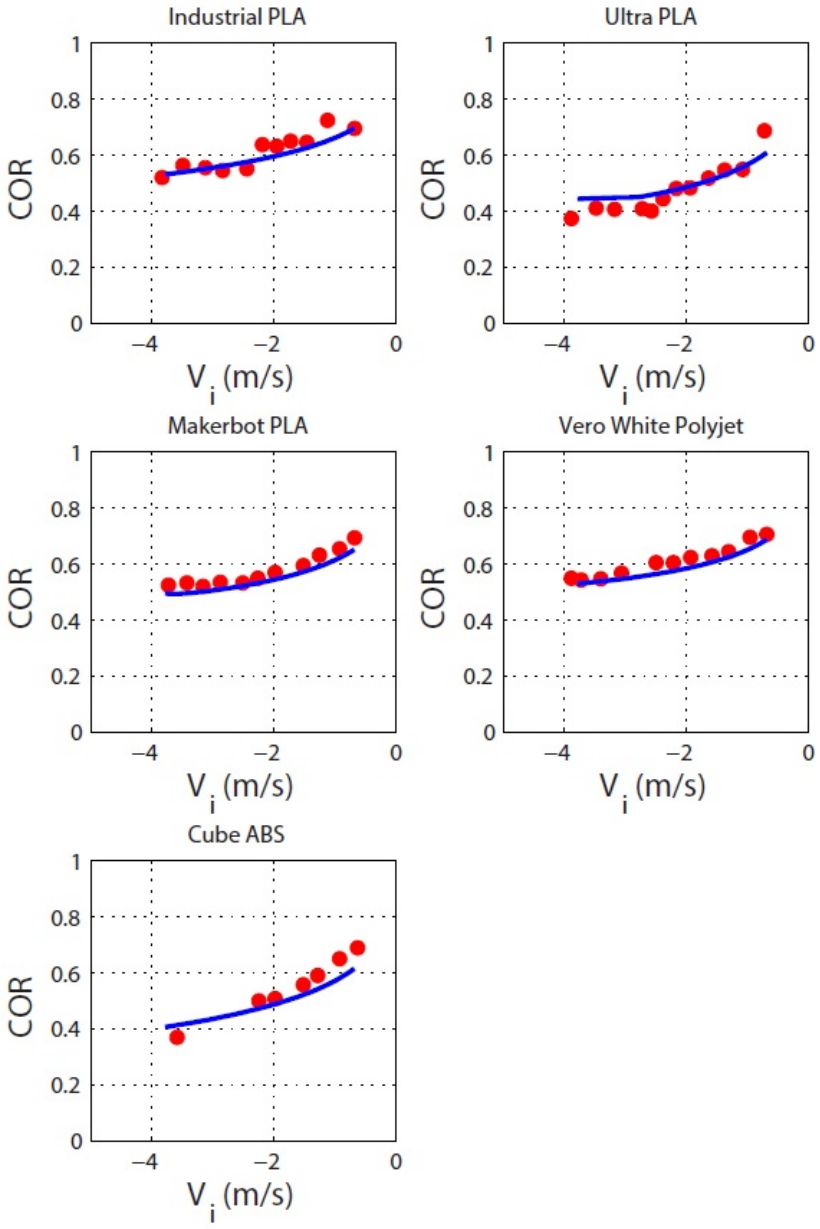

Figure 41. Verification of the formulation for coefficient of restitution of each of the materials.

Figure 42 shows the comparison between the model and the experimental data for the permanent

deformation. The models show a good agreement with average error less than 5% compare to the experiments. Results for the VeroWhite polyjet material is not presented because for the initial velocity range in our experiments the permanent deformations were negligible.

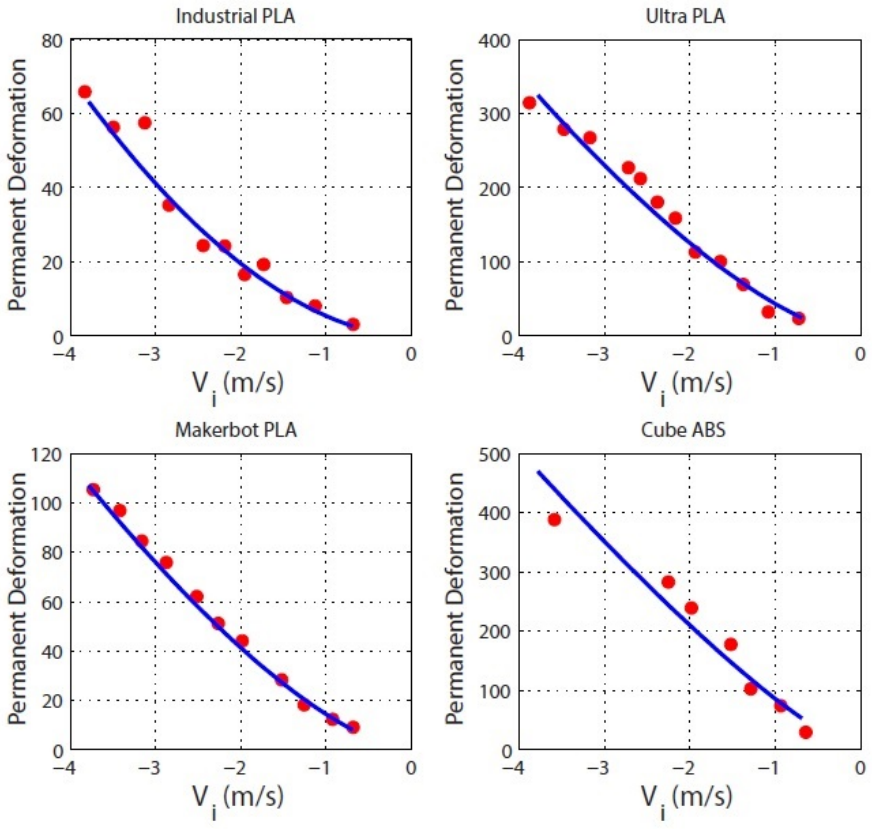

Figure 42. Verification of the formulation for permanent deformation of each of the materials.

To match the model to the experiments for the permanent deformation and the coefficient of restitution, both the history of the contact force and the impulse during the impact should follow the material behavior. This would show that the proposed model matches the behavior of the materials.

Finally the material behavior during impact can be simulated using the proposed formulation. Figure 43 shows the contact force as a function of deformation for all of the materials. The initial velocity of the impact is v_i = 0.68 (m/s) for all materials. The force starts with a positive value at

$\delta = 0$ because of the existence of a damper in the model. With the increase of the deformation the contact force increases until reaches the maximum value. At this instant the velocity is zero and the restitution phase starts. The difference between the maximum force and deformation of different materials is because of elastic phase of stronger materials such as Industrial PLA and Makerbot PLA than weaker ones which have less elastic phase and will get more maximum and permanent deformation, as it was mentioned before. During the restitution phase the contact force decreases until the deformation reaches the permanent deformation, $\delta = \delta_r$. The impact ends at this instant and the contact force is zero.

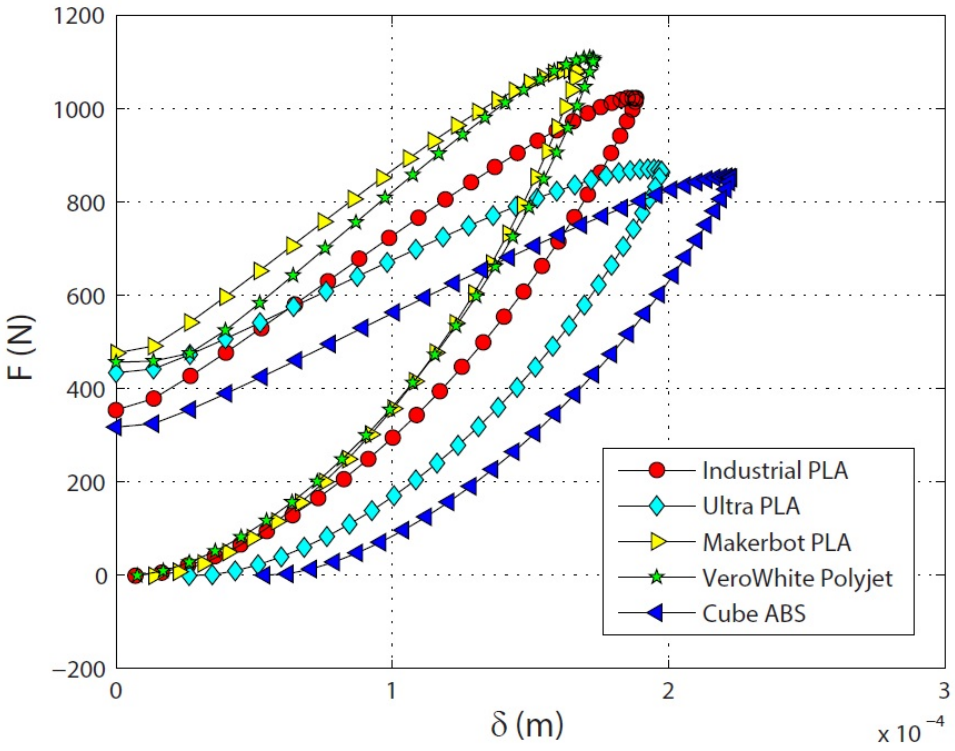

Figure 43. Contact force during the impact vs. deformation of the flat

The experimental and theoretical methods used in this research could be applied for other polymers to find same parameters for predicting permanent deformation and coefficient of restitution of these materials.

8. Sources of uncertainty

There are some sources for uncertainty in this study which could be considered for future similar experiments or follow-up researches. In the first experiment uncertainty would come from multiple sources. All growth plates were printed by Stratasys® Objet30 3D-printer with 28 µm layer thickness resolution. Since the research was done in the Chewacla creek bed and it is not perfectly flat, there would be chances of unequal light intensity getting to the tiles. In the harvesting process, because it was done manually, there would be very low percentage chance of attached biofilm remaining between features of surfaces. In the sampling for identifying algal species, there is always certain chances of not sampling all harvested biofilms to identify, since it is, almost, not possible to identify all harvested bios. In identifying process, two trained technicians were used to do the process to get the least chance of uncertainty, but still there would be chances to not identifying right species from micrographs.

In second experiment sources of uncertainty would come from several actions as well. Same would happen during harvesting tiles which is not completely harvesting in textures areas. There would be chances of uncertainty during weighing process for aluminum containers for both before and after oven drying. However, there was a proper cooling process before weighing containers after oven drying, still, there would be little chances of changing the weight of containers. All surfaces were scanned by Nanovia® ST-400 optical profilometer with lateral resolution of 1.55 µm and Z resolution of 20 nm. For taking micrographs during identification process, Motic B1-220 binocular microscope with 40x, 100x, 400x, and 1000x magnifications was used. Also, Acculab® ALC scale with 0.1 mg accuracy was used for weighing samples.

In the third experiment, the difference between additive manufacturing technologies would be a source of uncertainty where polyjet has different printing system and pattern than other FDM

machines. Experimental parts were tried to be smooth as possible (average roughness between 0.2 to 0.4 μm), but all parts do not have exact same surface roughness necessarily. During scanning impacted surfaces to find deepest point as permanent deformation, average of three deepest 2-D profiles was used, which may not be the exact deepest point for each impact. Also, to find initial and final velocity of rod during each impact, position of the tip of the rod has been found with finding the average of three horizontal lines from image processing for every moment which may not be the exact position. To find theoretical coefficient of restitution and maximum deformation (δ_m) numerical simulation with ordinary differential equation (ODE) in Matlab® was employed which would not be exact method for finding the parameters.

9. Conclusions

Improving algal cell density attached to surface by knowing different species attachment preferences and understand surface characterization to increase algal biomass has been investigated because of their application in aquatic pollution recovery, water quality improvements, as well as biomass production for various economic uses including protein production and biofuels.

Additive manufacturing, or 3D printing, was shown to be effective in making surface feature elements for experimentation into colonization dynamics of periphyton communities. Printed surface features of scales ranging from 100 to 2000 μm were successfully deployed to expose scale preferences for colonization for various species of a mixed periphyton community. Some species showed significant preferences for surface feature sizes of a particular scale range. *Microspora wileana* displayed a preference for surfaces with topographic feature sizes less than 500 μm, and *Stigeoclonium tenue* displayed a preference for surfaces with topographic feature sizes less than or equal to 100 μm and greater than or equal to 1500 μm. In other attempt for biomass analysis, clay tiles with different surface features deployed in laboratory-based bio-reactor. The dominant species in filamentous benthic algal community of this study was *Mougeotia sp,* which showed more attachment and colonization in 500 μm topographic section among others.

Through demonstrating the effect of surface topographic feature size on colonization dynamics of individual species, the surface feature size was shown to have an effect on the overall species diversity and amount of biomass of the colonizing periphyton community. These results suggest that surface design using additive manufacturing or other technologies may be used to affect species composition and dominance relationships in a mixed community in engineered systems for algal cultivation.

These research efforts aim to demonstrate important role of surface texture in algal attachment by changing area of contact between the algal cells and solid carrier surface as well as the potential for increasing the yield and productivity of algal biosystems. Surface characteristics, such as texture, are key factors in attachment of algal cells and maintaining integrity of growth surface topography. Several theories are applied to examine interaction between algal cells and surfaces, also to understand behavior of these solid carrier surfaces under dynamic contact forces.

In other effort, to investigate an important mechanical property of 3D-printed polymers which are using in different applications, five different 3D-printed materials have been analyzed during the impact. The contact force during the impact for each of the materials has been modeled. A damping force has been added to the Stronge's formulation for the impact. Behavior of each of the materials during the impact has been analyzed experimentally for both the coefficient of restitution and the permanent deformations. Experimental results have been used to find the needed coefficients in the formulation for each of the materials. Model were proposed to predict the behavior of these 3D-printed polymers under low speed collision. Proposed formulation showed very good agreement with experimental results with minimum error. This achievement means mechanical designs for future applications of these 3D-printed polymers could be more efficient and effective.

The potential contributions of this work will include:

- Fundamental knowledge of species selectivity by substrata topography that will aid in bioreactor designs for exclusion/inclusion of species that would increase efficiencies in water treatment or biomass applications.
- Fundamental knowledge of the relationship between growth rates and surface topography that would increase the biomass yield and regeneration cycles, thus improving the economics of such systems.

- A better understanding of the behavior of materials used in polymer 3D printing under low velocity collision to aid in the design and selection for natural environment applications.

As future study, bioreactors can be designed with more controlled and isolated situations for every species studied in this research, with changing only one factor, such as light intensity, nutrient level or type, and temperature at a time. Also, for every algal cell investigated in this study, cell attachment patterns can be investigated in detail, as well as fluid dynamic models for different bioreactors.

For mechanical impact study, there are several parameters in 3D-printed machines that can affect the permanent deformations and coefficient of restitution of printed polymers investigated in this study. Parameters such as porosity of printed part, average roughness of impacted surfaces, printing pattern and layer thickness of 3D-printing machines, and layer (film) of lubricant on surface can be changed for each experiment and be studied in future research.

10. References

1. Melchels, F. P. W. *et al.* Additive manufacturing of tissues and organs. *Prog. Polym. Sci.* **37,** 1079–1104 (2012).
2. *Algal Ecology: Freshwater Benthic Ecosystem*. (Academic Press, 1996).
3. Roeselers, G., Loosdrecht, M. C. M. van & Muyzer, G. Phototrophic biofilms and their potential applications. *J. Appl. Phycol.* **20,** 227–235 (2008).
4. Craggs, R. J., Adey, W. H., Jessup, B. K. & Oswald, W. J. A controlled stream mesocosm for tertiary treatment of sewage. *Ecol. Eng.* **6,** 149–169 (1996).
5. Adey, W. H., Luckett, C. & Smith, M. Purification of industrially contaminated groundwaters using controlled ecosystems. *Ecol. Eng.* **7,** 191–212 (1996).
6. Adey, W. H., Kangas, P. C. & Mulbry, W. Algal Turf Scrubbing: Cleaning Surface Waters with Solar Energy while Producing a Biofuel. *BioScience* **61,** 434–441 (2011).
7. Craggs, R. J. *et al.* Phosphorus removal from wastewater using an algal turf scrubber. *Water Sci. Technol.* **33,** 191–198 (1996).
8. 2. Kelp | Encyclopedia of Puget Sound. Available at: https://www.eopugetsound.org/science-review/2-kelp. (Accessed: 9th June 2016)
9. Adey, W. H. & Mulbry, W. W. Algal Turf Scrubber. Available at: http://www.chesapeake.org/stac/presentations/63_kangas.pdf. (Accessed: 14th June 2016)
10. Clarens, A. F., Resurreccion, E. P., White, M. A. & Colosi, L. M. Environmental Life Cycle Comparison of Algae to Other Bioenergy Feedstocks. *Environ. Sci. Technol.* **44,** 1813–1819 (2010).
11. Sandefur, H. N. *et al.* Hydrodynamic regime considerations for the cultivation of periphytic biofilms in two tertiary wastewater treatment systems. *Ecol. Eng.* **71,** 527–532 (2014).

12. Kangas, P. & Mulbry, W. Nutrient removal from agricultural drainage water using algal turf scrubbers and solar power. *Bioresour. Technol.* **152,** 484–489 (2014).
13. Mulbry, W., Kangas, P. & Kondrad, S. Toward scrubbing the bay: Nutrient removal using small algal turf scrubbers on Chesapeake Bay tributaries. *Ecol. Eng.* **36,** 536–541 (2010).
14. Mulbry, W., Kondrad, S., Pizarro, C. & Kebede-Westhead, E. Treatment of dairy manure effluent using freshwater algae: Algal productivity and recovery of manure nutrients using pilot-scale algal turf scrubbers. *Bioresour. Technol.* **99,** 8137–8142 (2008).
15. Ellwood, N. T. W., Di Pippo, F. & Albertano, P. Phosphatase activities of cultured phototrophic biofilms. *Water Res.* **46,** 378–386 (2012).
16. Mulbry, W., Kondrad, S. & Buyer, J. Treatment of dairy and swine manure effluents using freshwater algae: fatty acid content and composition of algal biomass at different manure loading rates. *J. Appl. Phycol.* **20,** 1079–1085 (2008).
17. Adey, W. H. *et al.* Algal turf scrubber (ATS) floways on the Great Wicomico River, Chesapeake Bay: productivity, algal community structure, substrate and chemistry1. *J. Phycol.* **49,** 489–501 (2013).
18. Miller, A. R., Lowe, R. L. & Rotenberry, J. T. Succession of Diatom Communities on Sand Grains. *J. Ecol.* **75,** 693–709 (1987).
19. Burkholder, J. M. & Wetzel, R. G. Microbial Colonization on Natural and Artificial Macrophytes in a Phosphorus-Limited, Hardwater Lake1. *J. Phycol.* **25,** 55–65 (1989).
20. Vadeboncoeur, Y., Kalff, J., Christoffersen, K. & Jeppesen, E. Substratum as a driver of variation in periphyton chlorophyll and productivity in lakes. *J. North Am. Benthol. Soc.* **25,** 379–392 (2006).

21. Whitehead, K. A. & Verran, J. The Effect of Surface Topography on the Retention of Microorganisms. *Food Bioprod. Process.* **84,** 253–259 (2006).
22. Crawford, R. J., Webb, H. K., Truong, V. K., Hasan, J. & Ivanova, E. P. Surface topographical factors influencing bacterial attachment. *Adv. Colloid Interface Sci.* **179–182,** 142–149 (2012).
23. Norton, T. A. & Fetter, R. The Settlement of Sargassum Muticum Propagules in Stationary and Flowing Water. *J. Mar. Biol. Assoc. U. K.* **61,** 929–940 (1981).
24. Burkholder, J. M. & Sheath, R. G. The Seasonal Distribution, Abundance and Diversity of Desmids (chlorophyta) in a Softwater, North Temperate Stream1. *J. Phycol.* **20,** 159–172 (1984).
25. Harlin, M. M. & Lindbergh, J. M. Selection of substrata by seaweeds: Optimal surface relief. *Mar. Biol.* **40,** 33–40 (1977).
26. Reed, D. C., Laur, D. R. & Ebeling, A. W. Variation in Algal Dispersal and Recruitment: The Importance of Episodic Events. *Ecol. Monogr.* **58,** 321–335 (1988).
27. Granhag, L., Finlay, J., Jonsson, P., Callow, J. & Callow, M. Roughness-dependent Removal of Settled Spores of the Green Alga Ulva (syn. Enteromorpha) Exposed to Hydrodynamic Forces from a Water Jet. *Biofouling* **20,** 117–122 (2004).
28. Cao, J. *et al.* A Preliminary Study of the Effect of Surface Texture on Algae Cell Attachment for a Mechanical-Biological Energy Manufacturing System. *J. Manuf. Sci. Eng.* **131,** 064505–064505 (2009).
29. Hassan, M. F., Lee, H. P. & Lim, S. P. Effects of Shear and Surface Roughness on Reducing the Attachment of Oscillatoria sp. Filaments on Substrates. *Water Environ. Res.* **84,** 744–752 (2012).

30. Cui, Y., Yuan, W. & Cao, J. Effects of surface texturing on microalgal cell attachment to solid carriers. *Int. J. Agric. Biol. Eng.* **6,** 44–54 (2013).
31. Dulieu-Barton, J. m. & Fulton, M. c. Mechanical Properties of a Typical Stereolithography Resin. *Strain* **36,** 81–87 (2000).
32. Caulfield, B., McHugh, P. E. & Lohfeld, S. Dependence of mechanical properties of polyamide components on build parameters in the SLS process. *J. Mater. Process. Technol.* **182,** 477–488 (2007).
33. Park, S.-I., Rosen, D. W., Choi, S. & Duty, C. E. Effective mechanical properties of lattice material fabricated by material extrusion additive manufacturing. *Addit. Manuf.* **1–4,** 12–23 (2014).
34. Karina Puebla, Karina Arcaute, Rolando Quintana & Ryan B. Wicker. Effects of environmental conditions, aging, and build orientations on the mechanical properties of ASTM type I specimens manufactured via stereolithography. *Rapid Prototyp. J.* **18,** 374–388 (2012).
35. Tymrak, B. M., Kreiger, M. & Pearce, J. M. Mechanical properties of components fabricated with open-source 3-D printers under realistic environmental conditions. *Mater. Des.* **58,** 242–246 (2014).
36. Giordano, R. A. *et al.* Mechanical properties of dense polylactic acid structures fabricated by three dimensional printing. *J. Biomater. Sci. Polym. Ed.* **8,** 63–75 (1997).
37. Ellis, A., Noble, C. J. & Hopkinson, N. High Speed Sintering: Assessing the influence of print density on microstructure and mechanical properties of nylon parts. *Addit. Manuf.* **1–4,** 48–51 (2014).

38. Sung-Hoon Ahn, Michael Montero, Dan Odell, Shad Roundy & Paul K. Wright. Anisotropic material properties of fused deposition modeling ABS. *Rapid Prototyp. J.* **8,** 248–257 (2002).

39. Kim, G. D. & Oh, Y. T. A benchmark study on rapid prototyping processes and machines: Quantitative comparisons of mechanical properties, accuracy, roughness, speed, and material cost. *Proc. Inst. Mech. Eng. Part B J. Eng. Manuf.* **222,** 201–215 (2008).

40. Javier Munguia & Kenny Dalgarno. Fatigue behaviour of laser-sintered PA12 specimens under four-point rotating bending. *Rapid Prototyp. J.* **20,** 291–300 (2014).

41. K. Chockalingam, N. Jawahar & U. Chandrasekhar. Influence of layer thickness on mechanical properties in stereolithography. *Rapid Prototyp. J.* **12,** 106–113 (2006).

42. N. Saleh, N. Hopkinson, R.J.M. Hague & S. Wise. Effects of electroplating on the mechanical properties of stereolithography and laser sintered parts. *Rapid Prototyp. J.* **10,** 305–315 (2004).

43. Fang, Z., Starly, B. & Sun, W. Computer-aided characterization for effective mechanical properties of porous tissue scaffolds. *Comput.-Aided Des.* **37,** 65–72 (2005).

44. Brandl, E., Baufeld, B., Leyens, C. & Gault, R. Additive manufactured Ti-6Al-4V using welding wire: comparison of laser and arc beam deposition and evaluation with respect to aerospace material specifications. *Phys. Procedia* **5, Part B,** 595–606 (2010).

45. Delgado, J., Ciurana, J. & Rodríguez, C. A. Influence of process parameters on part quality and mechanical properties for DMLS and SLM with iron-based materials. *Int. J. Adv. Manuf. Technol.* **60,** 601–610 (2011).

46. Fielding, G. A., Bandyopadhyay, A. & Bose, S. Effects of silica and zinc oxide doping on mechanical and biological properties of 3D printed tricalcium phosphate tissue engineering scaffolds. *Dent. Mater.* **28,** 113–122 (2012).
47. J.P. Kruth, X. Wang, T. Laoui & L. Froyen. Lasers and materials in selective laser sintering. *Assem. Autom.* **23,** 357–371 (2003).
48. Prashanth, K. G. *et al.* Production of high strength Al85Nd8Ni5Co2 alloy by selective laser melting. *Addit. Manuf.* **6,** 1–5 (2015).
49. Shamsaei, N., Yadollahi, A., Bian, L. & Thompson, S. M. An overview of Direct Laser Deposition for additive manufacturing; Part II: Mechanical behavior, process parameter optimization and control. *Addit. Manuf.* **8,** 12–35 (2015).
50. Spierings, A. B., Herres, N. & Levy, G. Influence of the particle size distribution on surface quality and mechanical properties in AM steel parts. *Rapid Prototyp. J.* **17,** 195–202 (2011).
51. Ben Vandenbroucke & Jean-Pierre Kruth. Selective laser melting of biocompatible metals for rapid manufacturing of medical parts. *Rapid Prototyp. J.* **13,** 196–203 (2007).
52. Delgado, J., Ciurana, J. & Serenó, L. Comparison of forming manufacturing processes and selective laser melting technology based on the mechanical properties of products. *Virtual Phys. Prototyp.* **6,** 167–178 (2011).
53. Brandl, E., Heckenberger, U., Holzinger, V. & Buchbinder, D. Additive manufactured AlSi10Mg samples using Selective Laser Melting (SLM): Microstructure, high cycle fatigue, and fracture behavior. *Mater. Des.* **34,** 159–169 (2012).
54. Horn, T. J. *et al.* Flexural properties of Ti6Al4V rhombic dodecahedron open cellular structures fabricated with electron beam melting. *Addit. Manuf.* **1–4,** 2–11 (2014).

55. Wauthle, R. *et al.* Effects of build orientation and heat treatment on the microstructure and mechanical properties of selective laser melted Ti6Al4V lattice structures. *Addit. Manuf.* **5,** 77–84 (2015).

56. J-P. Kruth, P. Mercelis, J. Van Vaerenbergh, L. Froyen & M. Rombouts. Binding mechanisms in selective laser sintering and selective laser melting. *Rapid Prototyp. J.* **11,** 26–36 (2005).

57. Poisson, S. D. & Garnier, J. G. *Traite de mecanique*. (Societe Belge de Librairie, 1838).

58. Johnson, K. L. *Contact mechanics*. (Cambridge university press, 1987).

59. Jackson, R. L., Ghaednia, H. & Pope, S. A Solution of Rigid–Perfectly Plastic Deep Spherical Indentation Based on Slip-Line Theory. *Tribol. Lett.* **58,** 1–7 (2015).

60. Kogut, L. & Etsion, I. Elastic-Plastic Contact Analysis of a Sphere and a Rigid Flat. *J. Appl. Mech.* **69,** 657–662 (2002).

61. Ghaednia, H., Pope, S. A., Jackson, R. L. & Marghitu, D. B. A comprehensive study of the elasto-plastic contact of a sphere and a flat. *Tribol. Int.* **93, Part A,** 78–90 (2016).

62. Ghaednia, H., Cermik, O. & Marghitu, D. B. Experimental and theoretical study of the oblique impact of a tennis ball with a racket. *Proc. Inst. Mech. Eng. Part P J. Sports Eng. Technol.* 1754337114567490 (2015). doi:10.1177/1754337114567490

63. Stronge, W. J. Rigid Body Collisions with Friction. *Proc. R. Soc. Lond. Math. Phys. Eng. Sci.* **431,** 169–181 (1990).

64. Stronge, W. J. Unraveling Paradoxical Theories for Rigid Body Collisions. *J. Appl. Mech.* **58,** 1049–1055 (1991).

65. Stronge, W. J. Energy Dissipated in Planar Collision. *J. Appl. Mech.* **59,** 681–682 (1992).

66. Stronge, W. J. Planar impact of rough compliant bodies. *Int. J. Impact Eng.* **15,** 435–450 (1994).

67. Stronge, W. J. in *Impacts in Mechanical Systems* (ed. Brogliato, B.) 189–234 (Springer Berlin Heidelberg, 2000).

68. Marghitu, D. B., Cojocaru, D. & Jackson, R. L. Elasto-plastic impact of a rotating link with a massive surface. *Int. J. Mech. Sci.* **53,** 309–315 (2011).

69. Jackson, R. L., Green, I. & Marghitu, D. B. Predicting the coefficient of restitution of impacting elastic-perfectly plastic spheres. *Nonlinear Dyn.* **60,** 217–229 (2009).

70. Kardel, K., Carrano, A. L., Blersch, D. M. & Kaur, M. Preliminary Development of 3D-Printed Custom Substrata for Benthic Algal Biofilms. *3D Print. Addit. Manuf.* **2,** 12–19 (2015).

71. Mulbry, W. W. & Wilkie, A. C. Growth of benthic freshwater algae on dairy manures. *J. Appl. Phycol.* **13,** 301–306 (2001).

72. Standard Methods for the Examination of Water and Wastewater 22nd ed. (2012).

73. Helms, B. *et al.* Development of Ecogeomorphological (EGM) Stream Design and Assessment Tools for the Piedmont of Alabama, USA. *Water* **8,** 161 (2016).

74. Google Maps. *Google Maps* Available at: https://www.google.com/maps/@32.5479459,-85.4808761,19.56z. (Accessed: 17th June 2016)

75. USGS CHEWACLA CREEK AT CHEWACLA STATE PARK NR AUBURN. *USGS Chewacla Creek, Auburn, Alabama*

76. Prescott, G. W. *How to know the freshwater algae*. (WC Brown, 1984).

77. Simpson, E.H. Measurement of diversity. *Nature* **163,** 688 (1949).

78. Lowe, R. L. & Gale, W. F. Monitoring river periphyton with artificial benthic substrates. *Hydrobiologia* **69,** 235–244 (1980).

79. McCormick, P. V., Shuford III, R. B. E. & Chimney, M. J. Periphyton as a potential phosphorus sink in the Everglades Nutrient Removal Project. *Ecol. Eng.* **27,** 279–289 (2006).

80. Larned, S. T., Nikora, V. I. & Biggs, B. J. Mass-transfer-limited nitrogen and phosphorus uptake by stream periphyton: A conceptual model and experimental evidence. *Limnol. Oceanogr.* **49,** 1992–2000 (2004).

81. Blunt, L. & Jiang, X. *Advanced Techniques for Assessment Surface Topography: Development of a Basis for 3D Surface Texture Standards 'Surfstand'*. (Elsevier, 2003).

82. Arrhenius, O. Species and Area. *J. Ecol.* **9,** 95–99 (1921).

83. Connor, E. F. & McCoy, E. D. The Statistics and Biology of the Species-Area Relationship. *Am. Nat.* **113,** 791–833 (1979).

84. Lokhorst, G. M. Taxonomic study of the genus Microspora THURET (Chlorophyceae) an integrated field, culture and herbarium analysis. *Arch. Für Hydrobiol. Suppl. Algol. Stud.* **128,** 1–38 (1999).

85. Francke, J. A. Morphological plasticity and ecological range in three Stigeoclonium species (Chlorophyceae, Chaetophorales). *Br. Phycol. J.* **17,** 117–133 (1982).

86. Montgomery, D. C. *Design and Analysis of Experiments*. (John Wiley & Sons, 2008).

87. Cooke, M. C. *British Fresh-water Algae, Exclusive of Desmidieae and Diatomaceae*. (Williams and Norgate, 1882).

88. Ghaednia, H., Marghitu, D. B. & Jackson, R. L. Predicting the Permanent Deformation After the Impact of a Rod With a Flat Surface. *J. Tribol.* **137,** 011403–011403 (2014).

89. Hertz, H. Ueber die Berührung fester elastischer Körper. *J. Für Reine Angew. Math.* **92,** 156–171 (1882).
90. Singh, R. Process capability study of polyjet printing for plastic components. *J. Mech. Sci. Technol.* **25,** 1011–1015 (2011).
91. Minguella Canela, J. *et al.* MESIC Manufacturing Engineering Society International Conference 2015.Characterization of Factors Influencing Dimensional and Geometric Errors in PolyJet Manufacturing of Cylindrical Features. *Procedia Eng.* **132,** 62–69 (2015).
92. Fused deposition modeling. *Wikipedia, the free encyclopedia* (2016).

Appendix I: Raw data of all identified and unidentified algal species (Experiment #1)

Down 1-1	Sub-1	Sub-2	Sub-3	Sub-1	Sub-2	Sub-3	Sub-1	Sub-2	Sub-3	Sub-1	Sub-2	Sub-3	Sub-1	Sub-2	Sub-3	Sub-1	Sub-2	Sub-3	Sub-1	Sub-2	Sub-3
100					2	1		1	1	2	3	1				1		1	3	3	4
500						1	2				1					1		2	5	1	5
1000				4	1	2						1	1						2	3	3
1500				2	1		2			1									4	1	2
2000			2	1		3	2		1	1	4						1	2	2	3	2
Smooth				1			1	1	2	2	1	1					3	1	1	5	6

Down 1-2	Sub-1	Sub-2	Sub-3	Sub-1	Sub-2	Sub-3	Sub-1	Sub-2	Sub-3	Sub-1	Sub-2	Sub-3	Sub-1	Sub-2	Sub-3	Sub-1	Sub-2	Sub-3	Sub-1	Sub-2	Sub-3
100					1					2		1			1			1		2	1
500					3	1	3	1	1	2	2								1	2	
1000						1		1	1	2	2						1		1	1	1
1500				1			1		1	1	2								1		2
2000				2	1	2	2	1	2	2	1	2				1	1			1	1
Smooth				1	1	1	1	1	1							1		1	3	5	5

Down 1-3	Sub-1	Sub-2	Sub-3	Sub-1	Sub-2	Sub-3	Sub-1	Sub-2	Sub-3	Sub-1	Sub-2	Sub-3	Sub-1	Sub-2	Sub-3	Sub-1	Sub-2	Sub-3	Sub-1	Sub-2	Sub-3
100					2		1		1	1		2				1			1		2
500				1				1			2	2						1		1	2
1000			1			2				1				1							
1500					2				1										1	2	
2000						1		1	1	2	1						2		1	2	
Smooth					1		1	2		3	2	2	1		1				1		2

Down 2-1	Sub-1	Sub-2	Sub-3	Sub-1	Sub-2	Sub-3	Sub-1	Sub-2	Sub-3	Sub-1	Sub-2	Sub-3	Sub-1	Sub-2	Sub-3	Sub-1	Sub-2	Sub-3	Sub-1	Sub-2	Sub-3
100					2							1	2	1				2	5		1
500								2		1									1	4	3
1000				1				1				1		1				1	3	4	
1500					1						2						1		4	1	8
2000					1	2			1				1							5	4
Smooth																			1	5	9

Down 2-2	Sub-1	Sub-2	Sub-3	Sub-1	Sub-2	Sub-3	Sub-1	Sub-2	Sub-3	Sub-1	Sub-2	Sub-3	Sub-1	Sub-2	Sub-3	Sub-1	Sub-2	Sub-3	Sub-1	Sub-2	Sub-3
100				1	1	2	2			1	3			1			1		5	3	1
500				2	2						1					1			1		
1000				1	1	1	2	1			1	1				1			1		2
1500				1	5	1	1				2	1					1		2	3	3
2000				1	2					2	1								1	2	1
Smooth				1						1										1	

Down 2-3	Sub-1	Sub-2	Sub-3	Sub-1	Sub-2	Sub-3	Sub-1	Sub-2	Sub-3	Sub-1	Sub-2	Sub-3	Sub-1	Sub-2	Sub-3	Sub-1	Sub-2	Sub-3	Sub-1	Sub-2	Sub-3
100				2		2										1		3	2	2	1
500												1				2					1
1000				1		1			4	2	1	2							3	3	1
1500					1	1		1			1		1					1	3		
2000			1		1			1			1							2		2	
Smooth						2	2	2	1		3								2	1	

UP 1-1	Sub-1	Sub-2	Sub-3	Sub-1	Sub-2	Sub-3	Sub-1	Sub-2	Sub-3	Sub-1	Sub-2	Sub-3	Sub-1	Sub-2	Sub-3	Sub-1	Sub-2	Sub-3	Sub-1	Sub-2	Sub-3
100																			3	7	3
500																			3	1	
1000																			3	3	4
1500															1	1			6	5	6
2000												1							5	3	3
Smooth																2	1		4	4	

UP 1-2	Sub-1	Sub-2	Sub-3	Sub-1	Sub-2	Sub-3	Sub-1	Sub-2	Sub-3	Sub-1	Sub-2	Sub-3	Sub-1	Sub-2	Sub-3	Sub-1	Sub-2	Sub-3	Sub-1	Sub-2	Sub-3
100							1		1									1	6	4	6
500						1	1			1		1					1	1	8	3	4
1000							1	1											3	3	2
1500																			3	3	3
2000											1								3	4	3
Smooth																1			6	5	7

UP 1-3	Sub-1	Sub-2	Sub-3	Sub-1	Sub-2	Sub-3	Sub-1	Sub-2	Sub-3	Sub-1	Sub-2	Sub-3	Sub-1	Sub-2	Sub-3	Sub-1	Sub-2	Sub-3	Sub-1	Sub-2	Sub-3
100																4	1		7	10	3
500				1	1			1		1	1						1		7	5	4
1000		1									2				1				5	9	9
1500						1				1		1							3	5	1
2000						1	1		1										3	3	5
Smooth						2			2	1						2	2		7	3	2

UP 2-1	Sub-1	Sub-2	Sub-3	Sub-1	Sub-2	Sub-3	Sub-1	Sub-2	Sub-3	Sub-1	Sub-2	Sub-3	Sub-1	Sub-2	Sub-3	Sub-1	Sub-2	Sub-3	Sub-1	Sub-2	Sub-3
100					1	3												1	6		5
500									1		1					1			1		
1000				1									1				1		1	4	4
1500						1						1							3	3	5
2000					1											1			2	3	2
Smooth						1	1										1		2	3	7

UP 2-2	Sub-1	Sub-2	Sub-3	Sub-1	Sub-2	Sub-3	Sub-1	Sub-2	Sub-3	Sub-1	Sub-2	Sub-3	Sub-1	Sub-2	Sub-3	Sub-1	Sub-2	Sub-3	Sub-1	Sub-2	Sub-3
100								1	1			2				2			1	3	1
500					1			1		2						1		1	2	2	1
1000					1	1					1		2							1	3
1500				1	1		1				2								4	2	6
2000					1						1	2			2				4	6	2
Smooth																	1	1	5	2	3

UP 2-3	Sub-1	Sub-2	Sub-3	Sub-1	Sub-2	Sub-3	Sub-1	Sub-2	Sub-3	Sub-1	Sub-2	Sub-3	Sub-1	Sub-2	Sub-3	Sub-1	Sub-2	Sub-3	Sub-1	Sub-2	Sub-3
100					1						1	1		1		1	2	1	1	5	2
500								1				1				2		2	1	1	1
1000							2	1	1										6	4	3
1500				1	1					1	1	2	1	2					4	3	1
2000					1	1			1				1				2	2	5	7	3
Smooth						1						1				3	3	4	2	1	1

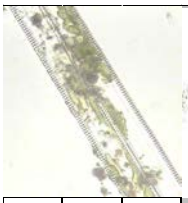												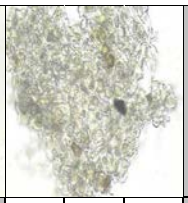			**Unidentified Diatoms**			**Unidentified Algae**		
Sub-1	Sub-2	Sub-3	Sub-1	Sub-2	Sub-3	Sub-1	Sub-2	Sub-3	Sub-1	Sub-2	Sub-3	Sub-1	Sub-2	Sub-3	Sub-1	Sub-2	Sub-3	Sub-1	Sub-2	Sub-3
						3			2	2	1				10	8	7	1	2	1
															6	3	7	1	1	2
									1	2			1		13	4	9	2	3	1
			1.33			1	1			1				1	7	7	7	2	1	0
		1							2	1		1	1		8	13	12	0	0	1
										2			1	1	13	5	10	0	1	1

Sub-1	Sub-2	Sub-3	Sub-1	Sub-2	Sub-3	Sub-1	Sub-2	Sub-3	Sub-1	Sub-2	Sub-3	Sub-1	Sub-2	Sub-3	Sub-1	Sub-2	Sub-3	Sub-1	Sub-2	Sub-3
						1		1	1	1				1	7	8	7	0	1	0
		1					1			1	1		1	1	5	9	11	2	1	0
							1		2	1	1			1	10	4	4	0	0	0
									3	2	1				10	12	6	0	0	1
										2	1	1			14	17	11	2	2	1
									3	2	1		1	1	9	4	11	4	3	1

Sub-1	Sub-2	Sub-3	Sub-1	Sub-2	Sub-3	Sub-1	Sub-2	Sub-3	Sub-1	Sub-2	Sub-3	Sub-1	Sub-2	Sub-3	Sub-1	Sub-2	Sub-3	Sub-1	Sub-2	Sub-3
											1	1		1	8	11	9	1	1	
														1	8	4	6	1		
	1								2	2		1		1	7	4	7			
									2	2	1	1		1	10	11	11			
									1						7	7	10			1
		1									1	1			13	8	7	1	1	1

Sub-1	Sub-2	Sub-3	Sub-1	Sub-2	Sub-3	Sub-1	Sub-2	Sub-3	Sub-1	Sub-2	Sub-3	Sub-1	Sub-2	Sub-3	Sub-1	Sub-2	Sub-3	Sub-1	Sub-2	Sub-3
									2		2			1	5	6	5		1	1
										1	1		1	1	7	7	6	1		1
	1					1	1		1	1	1	1	1	2	4	6	6	1		2
												2			6	8	7			1
											5	1			7	6	5	1	1	1
									4	1	1	3			3	4	2		2	

Sub-1	Sub-2	Sub-3	Sub-1	Sub-2	Sub-3	Sub-1	Sub-2	Sub-3	Sub-1	Sub-2	Sub-3	Sub-1	Sub-2	Sub-3	Sub-1	Sub-2	Sub-3	Sub-1	Sub-2	Sub-3
									7	5	4			1	10	5	4	4	2	
		1							1	1	2				6	6	10			
									1	1	1				9	7	6	1	2	
											1	1	1		7	5	6	1	1	
									2	1					5	7	3		1	
									2		6				9	15	4			

Sub-1	Sub-2	Sub-3	Sub-1	Sub-2	Sub-3	Sub-1	Sub-2	Sub-3	Sub-1	Sub-2	Sub-3	Sub-1	Sub-2	Sub-3	Sub-1	Sub-2	Sub-3	Sub-1	Sub-2	Sub-3
										2	1				5	1	3	1	1	
							1		1	1	2				14	9	8	1	2	
						1								1	7	6	5		2	
									2	2	1	2		2	2	8	10			
1						1			2	5	2				1	4	6	1	1	1
1										2	1				6	7	8			

Sub-1	Sub-2	Sub-3	Sub-1	Sub-2	Sub-3	Sub-1	Sub-2	Sub-3	Sub-1	Sub-2	Sub-3	Sub-1	Sub-2	Sub-3	Sub-1	Sub-2	Sub-3	Sub-1	Sub-2	Sub-3
									1	1					2		2	1		2
		1													2	1				
												1			2	3	1	1		
									1		3				5		7			
									1	1	4				3	4	4			
									1						1	2			1	

Sub-1	Sub-2	Sub-3	Sub-1	Sub-2	Sub-3	Sub-1	Sub-2	Sub-3	Sub-1	Sub-2	Sub-3	Sub-1	Sub-2	Sub-3	Sub-1	Sub-2	Sub-3	Sub-1	Sub-2	Sub-3
						3				2					5	6	2			1
											1				4	4	8	2		
											2				3	2	9		2	
															2	4	6		1	
										1	1				1	3	3			
									2	1	2				4	4	3			2

Sub-1	Sub-2	Sub-3	Sub-1	Sub-2	Sub-3	Sub-1	Sub-2	Sub-3	Sub-1	Sub-2	Sub-3	Sub-1	Sub-2	Sub-3	Sub-1	Sub-2	Sub-3	Sub-1	Sub-2	Sub-3
															12	6	5	1		2
											1		1		9	11	14	3	1	3
2															10	9	4	1		
											2				10	4	6	3		
1									1	3	1				3	7	8	1	2	2
										2				1	4	6	5		1	1

Sub-1	Sub-2	Sub-3	Sub-1	Sub-2	Sub-3	Sub-1	Sub-2	Sub-3	Sub-1	Sub-2	Sub-3	Sub-1	Sub-2	Sub-3	Sub-1	Sub-2	Sub-3	Sub-1	Sub-2	Sub-3
									1	3	2				3	9	4		3	3
		1								1					4	7	4			2
										1					5	6	12		1	
									1	1	2				5	10	5		2	
									8	1	5				5	3	4	3	1	2
									2	1	2				4	1	5	2	1	

Sub-1	Sub-2	Sub-3	Sub-1	Sub-2	Sub-3	Sub-1	Sub-2	Sub-3	Sub-1	Sub-2	Sub-3	Sub-1	Sub-2	Sub-3	Sub-1	Sub-2	Sub-3	Sub-1	Sub-2	Sub-3
									5	4	1				14	11	13		2	1
									2	2					7	7	7	1	1	1
										2					8	5	10	3		1
									2		1				5	10	4	1		3
									1	3	2				13	7	7	2	2	
									1				1		2	1	6	1		

Sub-1	Sub-2	Sub-3	Sub-1	Sub-2	Sub-3	Sub-1	Sub-2	Sub-3	Sub-1	Sub-2	Sub-3	Sub-1	Sub-2	Sub-3	Sub-1	Sub-2	Sub-3	Sub-1	Sub-2	Sub-3
											2				3	4	4	1	1	1
										1	2				2	7	9			1
1									1						5	6	5	2	1	
									3		3		1	1	9	5	4	1	2	1
									1	3	3		2	1	12	9	5	1	2	
									1		4				8	5	3		1	2

Appendix II: Raw data of all replications (Experiment #2)

Replication 1 results:

Weights in Grams		Before Heating	After Heating	Biomass
1	2000	3.9346	4.0123	0.0777
	1000	3.9319	3.9677	0.0358
	500	3.9141	4.022	0.1079
	Plain	3.8978	3.9012	0.0034
2	2000	3.9187	4.0049	0.0862
	1000	3.8268	3.9644	0.1376
	500	3.9149	3.9976	0.0827
	Plain	3.9249	3.9487	0.0238
3	2000	3.8803	3.9615	0.0812
	1000	3.9163	3.9765	0.0602
	500	3.8819	3.9521	0.0702
	Plain	3.885	3.9018	0.0168
4	2000	3.9139	4.0391	0.1252
	1000	3.9058	3.9985	0.0927
	500	3.949	4.0804	0.1314
	Plain	3.8748	3.9549	0.0801
5	2000	3.8953	4.0304	0.1351
	1000	3.9182	3.9328	0.0146
	500	3.8999	4.0848	0.1849
	Plain	3.9033	3.9154	0.0121
6	2000	3.8863	4.0001	0.1138
	1000	3.9034	3.9871	0.0837
	500	3.9051	4.0458	0.1407
	Plain	3.9087	3.9728	0.0641
7	2000	3.9387	4.0767	0.138
	1000	3.9084	3.9819	0.0735
	500	3.9254	4.0855	0.1601
	Plain	3.9078	4.0023	0.0945
8	2000	3.901	4.0097	0.1087
	1000	3.9417	3.9953	0.0536
	500	3.9367	4.0656	0.1289
	Plain	3.8956	3.9698	0.0742

Replication 2 results:

Weights in Grams		Before Heating	After Heating	Biomass
1	2000	3.9946	4.1105	0.1159
	1000	3.9489	4.1061	0.1572
	500	3.9076	4.0752	0.1676
	Plain	3.9912	4.0237	0.0325
2	2000	3.9621	4.1026	0.1405
	1000	3.8721	3.9519	0.0798
	500	3.9309	4.1071	0.1762
	Plain	3.9782	4.0548	0.0766
3	2000	3.9021	4.0525	0.1504
	1000	3.8953	4.1549	0.2596
	500	3.9433	4.12	0.1767
	Plain	3.958	4.0058	0.0478
4	2000	3.9264	4.0721	0.1457
	1000	3.9171	4.0203	0.1032
	500	3.8838	4.0791	0.1953
	Plain	3.8721	3.9508	0.0787
5	2000	3.8869	4.0525	0.1656
	1000	3.8995	4.0096	0.1101
	500	3.911	4.158	0.247
	Plain	3.9044	3.9971	0.0927
6	2000	3.8657	3.9684	0.1027
	1000	3.8635	3.9396	0.0761
	500	3.8897	4.111	0.2213
	Plain	3.8871	3.969	0.0819
7	2000	3.8986	4.113	0.2144
	1000	3.9253	4.0399	0.1146
	500	3.9069	4.1585	0.2516
	Plain	3.8868	3.9797	0.0929
8	2000	3.9056	4.0787	0.1731
	1000	3.9342	4.0306	0.0964
	500	3.8847	4.0986	0.2139
	Plain	3.8946	3.9766	0.082

Replication 3 results:

Weights in Grams		Before Heating	After Heating	Biomass
1	2000	3.8807	4.0589	0.1782
	1000	3.9565	4.0713	0.1148
	500	3.9704	4.1575	0.1871
	Plain	3.9505	4.088	0.1375
2	2000	3.9121	4.0538	0.1417
	1000	3.9489	4.0667	0.1178
	500	3.8739	4.0285	0.1546
	Plain	3.894	3.9859	0.0919
3	2000	3.9409	4.1179	0.177
	1000	3.9987	4.1294	0.1307
	500	3.8619	4.0484	0.1865
	Plain	3.9975	4.1371	0.1396
4	2000	3.9651	4.1583	0.1932
	1000	3.9652	4.1508	0.1856
	500	3.982	4.1716	0.1896
	Plain	4.0034	4.0846	0.0812
5	2000	3.9969	4.2161	0.2192
	1000	3.9547	4.0891	0.1344
	500	4.0003	4.1845	0.1842
	Plain	4.0018	4.1259	0.1241
6	2000	3.983	4.1116	0.1286
	1000	3.9768	4.1044	0.1276
	500	3.9923	4.1827	0.1904
	Plain	3.9949	4.1084	0.1135
7	2000	3.9675	4.2081	0.2406
	1000	3.9698	4.1037	0.1339
	500	3.9694	4.2038	0.2344
	Plain	3.9573	4.0581	0.1008
8	2000	3.998	4.142	0.144
	1000	3.9481	4.0366	0.0885
	500	3.9627	4.1704	0.2077
	Plain	3.9896	4.0767	0.0871

Appendix III: Log data from bioreactor (experiment #2)

Date	pH	Temp (F)	Conductivity (mS/cm)	Total water (G)	Water addition (g)	Nutrient addition (ml)	Comments
10/15/15	7.46	73.8	0.66	27.0	3.0	3.0	Starting rep1
10/16/15	7.40	74.9	0.69	28.0	2.0	2.0	
10/17/15	7.59	73.0	0.71	28.0	2.0	2.0	
10/18/15	7.87	73.3	0.75	26.0	4.0	4.0	
10/19/15	7.83	73.2	0.73	27.5	2.5	2.5	
10/20/15	7.86	73.7	0.74	27.5	2.5	2.5	
10/21/15	7.82	74.4	0.69	28.0	2.0	2.0	
10/22/15	7.82	75.2	0.67	28.0	2.0	2.0	
10/23/15	7.80	75.1	0.66	28.0	2.0	2.0	
10/24/15	7.74	75.4	0.66	27.0	3.0	3.0	
10/25/15	7.82	75.3	0.65	28.0	2.0	2.0	
10/26/15	7.82	74.9	0.65	21.0	9.0	9.0	
10/27/15	7.83	75.3	0.58	28.0	2.0	2.0	
10/28/15	7.83	75.5	0.60	27.5	2.5	2.5	
10/29/15	7.74	75.4	0.59	28.0	2.0	2.0	
10/30/15	8.03	73.4	0.59	27.0	3.0	3.0	
10/31/15							
11/1/15	7.65	75.5	0.59	26.5	3.5	3.5	
11/2/15	7.69	75.4	0.57	28.0	2.0	2.0	
11/3/15	7.62	75.1	0.58	27.0	3.0	3.0	
11/4/15	7.92	75.1	0.55	20.0	10.0	10.0	Harvest rep1
11/5/15	7.67	75.2	0.57	28.0	2.0	2.0	
11/6/15	7.68	75.1	0.56	27.0	3.0	3.0	
11/7/15	7.69	75.0	0.55	28.0	2.0	2.0	Starting rep2
11/8/15	7.64	74.6	0.57	27.5	2.5	2.5	
11/9/15	7.66	74.4	0.58	28.0	2.0	2.0	
11/10/15	7.76	74.4	0.58	28.0	2.0	2.0	
11/11/15	7.59	74.3	0.52	28.0	2.0	2.0	
11/12/15	7.51	74.8	0.48	28.0	2.0	2.0	
11/13/15	7.63	72.9	0.45	27.0	3.0	3.0	
11/14/15							
11/15/15	7.52	73.8	0.45	26.0	4.0	4.0	
11/16/15	7.39	74.8	0.42	28.0	2.0	2.0	
11/17/15	7.44	75.2	0.43	29.0	1.0	1.0	
11/18/15	7.53	74.5	0.44	28.0	2.0	2.0	
11/19/15	7.78	72.8	0.43	28.5	1.5	1.5	
11/20/15	7.85	73.2	0.46	27.5	2.5	2.5	
11/21/15							
11/22/15	7.62	73.2	0.48	27.0	3.0	3.0	

Log data for experiment #2:

Date	pH	Temp (F)	Conductivity (mS/cm)	Total water (G)	Water addition (g)	Nutrient addition (ml)	Comments
11/23/15	7.62	73.3	0.48	27.5	2.5	2.5	
11/24/15	7.54	73.4	0.49	28.5	1.5	1.5	
11/25/15	7.66	73.2	0.52	28.5	1.5	1.5	
11/26/15	7.53	74.4	0.53	29.0	1.0	1.0	
11/27/15	7.48	75.2	0.53	20.0	10.0	10.0	Harvest rep2
11/28/15							
11/29/15	7.40	75.1	0.55	27.0	3.0	3.0	
11/30/15	7.47	75.4	0.59	28.0	2.0	2.0	Starting rep3
12/1/15	7.45	75.5	0.53	28.0	2.0	2.0	
12/2/15	7.12	75.2	0.47	29.0	1.0	1.0	
12/3/15	7.38	73.6	0.50	28.0	2.0	2.0	
12/4/15	7.44	73.2	0.55	29.0	1.0	1.0	
12/5/15	7.22	73.5	0.56	27.0	3.0	3.0	
12/6/15	7.69	73.5	0.58	28.0	2.0	2.0	
12/7/15	7.55	74.5	0.60	28.0	2.0	2.0	
12/8/15	7.55	73.6	0.61	28.0	2.0	2.0	
12/9/15	7.58	74.8	0.63	28.0	2.0	2.0	
12/10/15	7.66	75.6	0.63	28.0	2.0	2.0	
12/11/15	7.98	75.4	0.66	28.0	2.0	2.0	
12/12/15	7.82	75.2	0.65	28.0	2.0	2.0	
12/13/15	7.70	75.4	0.67	29.0	1.0	1.0	
12/14/15	7.84	75.5	0.67	28.5	1.5	1.5	
12/15/15	7.77	74.4	0.70	29.0	1.0	1.0	
12/16/15	7.79	75.0	0.68	28.0	2.0	2.0	
12/17/15	7.64	75.4	0.68	28.0	2.0	2.0	
12/18/15	7.87	73.7	0.68	28.5	1.5	1.5	
12/19/15	7.83	73.4	0.71	28.5	1.5	1.5	
12/20/15	7.88	73.9	0.74	28.0	2.0	2.0	Harvest rep3

Appendix IV: Raw data for experiment #3

Industrial PLA:

e	sf	ef	th
0.647	500	750	50
0.705	450	700	90
0.734	450	700	90
0.707	800	1100	80
0.55	800	1000	40
0.7432	950	1150	90
0.747	350	550	70
0.6354	400	600	70
0.6563	400	600	70
0.6462	200	450	70
0.6558	200	450	70
0.6493	200	450	70
0.61107	250	400	70
0.631	200	400	70
0.64974	200	400	70
0.6449	150	400	70
0.633	150	400	70
0.6349	150	400	70
0.4856	100	350	70
0.6148	100	350	70
0.549	100	300	70
0.54323	100	300	70
0.5419	100	300	70
0.56	100	300	70
0.5652	100	300	70
0.5421	100	300	70
0.559	100	300	70
0.5657	100	300	70
0.5661	100	300	70
0.5175	20	250	70
0.5242	20	250	70

Vi	Vf	e	PD
0.684367	0.475133	0.695333	12.12333
1.128533	0.75193	0.666733	8.06
1.462673	0.993933	0.679567	10.47
1.732977	1.127433	0.650433	19.24333
1.958767	1.234103	0.630603	16.56
2.192633	1.398433	0.6376	24.18667
2.44445	1.34247	0.5502	24.45333
2.8433	1.549367	0.54471	35.26333
3.128133	1.73882	0.555767	57.55667
3.496467	1.970833	0.5636	56.31667
3.83255	1.99555	0.52085	65.87667

Industrial PLA (continue)

EXP#	W1	W2	PD
1	1689.12	1236.96	3.1
2	4243.14	4429.35	18.67
3	4314.39	4310.59	14.6
4	3055.98	2579.02	9.26
5	3002.01	4615.79	4.25
6	3219.22	3191.63	10.67
7	3647.89	4061.88	8.77
8	3764.12	3252.23	11.37
9	3666.44	3866.82	11.27
10	4120.7	4266.82	16.33
11	4119.85	4148.64	18.78
12	4164.59	4164.79	22.62
13	4293.97	4324.88	16.41
14	4253.14	4429.35	18.67
15	4314.39	4300.59	14.6
16	4365.42	4613.99	29.31
17	4498.12	4634.88	22.59
18	4508.33	4530.42	20.66
19	4814.55	4770.69	23.22
20	4838.28	4781.13	24
21	4773.72	4896.05	26.14
22	5222.84	5136.32	33.64
23	5324.91	5296.41	37.11
24	5273.88	5240.78	35.04
25	5620.92	5595.97	56.3
26	5656.85	5558.04	57.56
27	5634.29	5615.86	58.81
28	5758.24	5743.05	55.71
29	5780.88	5731.49	50.24
30	5859.81	5881.81	63
31	5950.02	5928.06	64.36
32	6040.23	6043.69	63.66
33	6096.61	6124.63	69.61

Ultra PLA:

EXP#	vi	vf	e	sf	ef	th
1	-3.8065	1.56802	0.4119	50	200	80
2	-4.007	1.2899	0.3218	50	250	70
3	-3.8318	1.4845	0.3874	50	250	60
4	-3.4526	1.4622	0.4235	50	250	60
5	-3.4835	1.41405	0.40592	50	250	60
6	-3.4905	1.3919	0.3987	50	250	60
7	-3.2028	1.30313	0.4069	50	250	60
8	-3.1453	1.26499	0.4021	50	250	60
9	-3.1742	1.2896	0.4062	50	250	60
10	-2.73	1.067	0.3909	50	250	60
11	-2.72	1.1052	0.4062	50	250	70
12	-2.7117	1.1562	0.4263	50	250	70
13	-2.5527	1.10844	0.4342	100	280	70
14	-2.561	0.9786	0.38198	100	280	70
15	-2.6178	1.0038	0.38347	100	280	70
16	-2.4112	1.067	0.4425	150	320	70
17	-2.404	1.0603	0.441	150	320	70
18	-2.334	1.04315	0.4469	150	320	70
19	-2.17643	0.95993	0.44106	150	320	70
20	-2.1096	1.1211	0.5314	150	320	70
21	-2.2228	1.04224	0.4688	150	320	80
22	-1.9046	0.9454	0.49	150	320	80
23	-1.94751	0.94548	0.4854	150	320	80
24	-1.9575	0.92	0.4725	150	320	80
25	-1.5428	0.81	0.525	210	410	70
26	-1.6771	0.9293	0.5541	210	410	60
27	-1.70932	0.816	0.4774	210	410	70
28	-1.3931	0.7489	0.5376	310	450	70
30	-1.35074	0.7497	0.555	320	490	70
31	-1.1004	0.5753	0.523	520	790	70
32	-1.097	0.589	0.5366	520	790	70
33	-1.044	0.61143	0.5854	520	790	70
34	-0.6713	0.4808	0.7162	520	790	70
35	-0.75726	0.5071	0.66971	520	790	70
36	-0.73642	0.498784	0.677305	520	790	70

Vi	Vf	e	PD
3.881767	1.447473	0.3737	314.9033
3.475533	1.422717	0.409373	278.9967
3.1741	1.285907	0.405067	267.12
2.720567	1.109467	0.4078	227.0733
2.577167	1.03028	0.399883	211.9133
2.383067	1.056817	0.443467	180.5767
2.16961	1.04109	0.48042	158.99
1.936537	0.93696	0.482633	113.48
1.643073	0.851767	0.518833	100.3933
1.37192	0.7493	0.5463	69.21
1.080467	0.59191	0.548333	32.70333
0.721658	0.495561	0.687738	23.80333

Ultra PLA (continue):

EXP#	W1	W2	PD
1	6982.57	7566.83	302.32
2	7182.47	7163.11	322.1
3	7880.23	7471.24	320.29
4	6619.11	7029.14	279.61
5	6782.92	6456.25	263.42
6	6984.96	7221.05	293.96
7	6379.41	6988.95	240.38
8	7266.2	7284.69	281.33
9	6861.49	6965.18	279.65
10	6580.39	6428.88	230.01
11	6247.46	6045.17	196.18
12	6707.98	6535.14	255.03
13	6121.86	6270.55	202.13
14	6400.97	6333.54	217.31
15	6721.94	6560.34	216.3
16	5870.66	6144.55	170.19
17	6219.55	6207.56	183.12
18	6163.73	6144.83	188.42
19	5689.24	5690.96	169.21
20	5675.29	5716.16	149.26
21	5884.62	5728.76	158.5
22	5294.29	6144.55	110.87
23	5513.6	5213.57	131.83
24	5030.76	5112.37	97.74
25	5203.97	5224.81	116.21
26	5034.51	4902.39	94.25
27	4949.93	4808.79	90.72
28	4740.91	4820.03	74.63
29	4571.88	4707.59	71.84
30	4270.05	4538.93	61.16
31	3772.53	3902.05	31.2
32	3752.66	3845.59	32.85
33	3772.35	3836.18	34.06
34	3199.46	4005.55	25.16
35	3549.3	3537.65	22.17
36	3291.56	3467.32	24.08

Vero White Polyjet:

EXP#	vi	vf	e	sf	ef	th		Vi	Vf	e
1	-0.7022	0.4949	0.7047	520	790	100				
2	-0.649	0.4388	0.6762	520	790	100		0.681767	0.482167	0.706565
3	-0.6941	0.5128	0.738796	520	790	100				
4	-0.94433	0.67157	0.7111	520	790	90				
5	-0.9622	0.6644	0.6904	520	790	90		0.95551	0.66199	0.694933
6	-0.96	0.65	0.6833	520	790	90				
7	-1.33	0.86	0.6519	200	500	90				
8	-1.308	0.8517	0.650775	200	500	90		1.311147	0.841467	0.643358
9	-1.29544	0.8127	0.6274	300	600	90				
10	-1.308	0.8517	0.650775	200	500	90				
11	-1.58	0.9902	0.6267	200	500	140		1.489333	0.9457	0.635758
12	-1.58	0.9952	0.6298	200	500	140				
13	-1.9582	1.1931	0.60927	100	500	140				
14	-1.91345	1.1919	0.6229	100	500	140		1.936087	1.2052	0.622757
15	-1.93661	1.2306	0.6361	150	450	140				
16	-2.9909	1.73966	0.581644	100	350	140				
17	-2.2149	1.3371	0.603667	150	450	140		2.471867	5.47052	0.596454
18	-2.2098	13.3348	0.60405	150	450	140				
19	-2.4865	1.51334	0.6086	100	350	140				
20	-2.48626	1.49934	0.603	100	350	140		2.497947	1.512993	0.605677
21	-2.52108	1.5263	0.60543	100	350	140				
22	-2.9909	1.73966	0.581644	100	350	140				
23	-3.08861	1.76724	0.5721	100	350	140		3.064487	1.735437	0.566481
24	-3.11395	1.69941	0.5457	100	350	140				
25	-3.35593	1.9059	0.5679	100	350	140				
26	-3.409	1.85735	0.54482	50	250	140		3.406577	1.862383	0.546879
27	-3.4548	1.8239	0.527918	50	250	120				
28	-3.74371	2.0293	0.542038	50	250	120				
29	-3.7165	2.0039	0.5382	50	250	100		3.722403	2.021753	0.542746
30	-3.707	2.03206	0.548	50	250	100				
31	-3.87906	2.1503	0.5543	50	250	100				
32	-3.87186	2.1374	0.552	50	250	100		3.882707	2.1339	0.549567
33	-3.8972	2.114	0.5424	50	250	100				

Makerbot PLA:

EXP#	vi	vf	e	sf	ef	th	Vi	Vf	e	PD
1	-3.7156	1.9602	0.52757	50	250	100	3.7299	1.9547	0.524084	105.38
2	-3.72	1.963	0.527682	50	250	100				
3	-3.7541	1.9409	0.517	50	250	100				
4	-3.4063	1.7788	0.5222	50	250	100	3.423137	1.818667	0.531333	96.78
5	-3.4	1.825	0.537	50	250	100				
6	-3.46311	1.8522	0.5348	50	250	100				
7	-3.2132	1.7039	0.53027	50	250	100	3.162267	1.643567	0.51969	84.52333
8	-3.1	1.6391	0.5286	50	250	100				
9	-3.1736	1.5877	0.5002	50	250	100				
10	-2.8253	1.5003	0.531	50	250	100	2.87699	1.539533	0.535137	75.81
11	-2.86507	1.5633	0.5456	50	250	100				
12	-2.9406	1.555	0.52881	50	250	100				
13	-2.556	1.354	0.5295	50	250	100	2.51705	1.338567	0.531733	62.18667
14	-2.48715	1.3407	0.539	50	250	100				
15	-2.508	1.321	0.5267	50	250	100				
16	-2.3212	1.2483	0.53779	100	300	100	2.267467	1.2436	0.548659	51.09333
17	-2.2557	1.2151	0.5387	100	300	100				
18	-2.2255	1.2674	0.569487	100	300	100				
19	-1.9783	1.1249	0.5686	100	300	100	1.98493	1.1302	0.5693	44.17
20	-1.994	1.1183	0.5606	100	300	100				
21	-1.98249	1.1474	0.5787	100	300	100				
22	-1.5311	0.91043	0.5946	100	300	100	1.5237	0.905977	0.593357	28.30667
23	-1.4958	0.8812	0.5891	100	300	100				
24	-1.5442	0.9263	0.59637	100	300	100				
25	-1.2581	0.8034	0.6385	300	500	100	1.501867	0.901043	0.60749	18.28667
26	-1.994	1.1183	0.5606	100	300	100				
27	-1.2535	0.78143	0.62337	300	500	100				
28	-0.94137	0.6072	0.64509	300	500	100	0.925343	0.604667	0.653497	12.44333
29	-0.91736	0.6034	0.6577	300	500	100				
30	-0.9173	0.6034	0.6577	300	500	100				
31	-0.69	0.457	0.6623	300	500	100	0.685267	0.481667	0.704567	9.166667
32	-0.6819	0.4939	0.7263	300	500	100				
33	-0.6839	0.4941	0.7251	300	500	100				

Makerbot PLA (continue)

EXP#	W1	W2	PD
1	5860.33	5488.72	103.82
2	5845.48	5862.11	107.14
3	5954.39	5642.05	105.18
4	5673.68	5725.78	100.62
5	5622.65	5630.08	99.18
6	5686.44	5713.82	90.54
7	5444.02	5307.12	84.24
8	5845.48	5862.11	75.77
9	5238.99	5669	93.56
10	5117.08	5358.95	79.68
11	5188.2	5106.32	72.45
12	5271.23	5140.77	75.3
13	4652	4865.17	61.68
14	4789.61	4773.3	59.46
15	4801.07	4738.85	65.42
16	4422.65	4486.22	51.89
17	4479.99	4463.25	50.06
18	4560.26	4440.29	51.33
19	4325.59	4290.72	49.93
20	4104.3	4126.69	38.65
21	4378.7	4232.83	43.93
22	3874.16	3885.46	25.41
23	3821.05	3981.95	29.33
24	3930.92	3810.85	30.18
25	3512.16	3351.59	17.83
26	3394.61	3497.05	19.79
27	3405.3	3560.68	17.24
28	2849.64	3224.32	9.24
29	2828.27	2933.41	13.79
30	2871.01	2924.32	14.3
31	2304.66	2406.14	10.17
32	2293.98	2278.86	8.9
33	2447.05	2360.68	8.43

Cube Tough ABS:

EXP#	vi	vf	e	sf	ef	th
1	-0.7764	0.4175	0.5377	550	900	100
2	-0.76402	0.4116	0.5388	450	800	100
3	-0.74663	0.38804	0.5202	550	900	100
4	-1.0212	0.503	0.4928	550	900	100
5	-1.03	0.525	0.5105	550	900	100
6	-1.05	0.55236	0.5259	550	900	100
7	-1.42856	0.6268	0.4387	250	700	100
8	-1.4324	0.6498	0.4536	250	700	100
9	-1.444	0.6157	0.4262	250	700	100
10	-1.7532	0.667	0.38046	250	600	100
11	-1.7259	0.6789	0.39336	250	600	100
12	-1.79665	0.73183	0.4073	250	600	100
13	-2.2057	0.827	0.3749	100	500	100
14	-2.091	0.7313	0.349	100	500	100
15	-2.20526	0.8627	0.39121	100	500	100
16	-2.4311	0.8945	0.3679	100	500	100
17	-2.4171	0.8558	0.354	100	500	100
18	-2.5234	0.938119	0.3717	100	500	100

Vi	Vf	e	PD
0.76235	0.405713	0.532233	141.4667
1.033733	0.526787	0.509733	183.5967
1.434987	0.630767	0.4395	338.79
1.758583	0.692577	0.393707	505.7467
2.16732	0.807	0.371703	628.8633
2.4572	0.89614	0.364533	716.79

EXP#	W1	W2	PD
1	4973.31	5487	146.71
2	5289.15	5162.12	125.88
3	5650.1	5765.47	151.81
4	5620.02	5873.76	207.06
5	7788.13	5997.52	175.91
6	5691.79	5703.58	167.82
7	6959.74	7374.4	335.68
8	6739.96	7581.54	307.16
9	7357.57	7635.61	373.53
10	7551.44	7996.06	500.28
11	9289.2	7797.81	501.19
12	7755.23	7653.63	515.77
13	8540.48	10339.63	625.48
14	8248.29	8361.37	624.88
15	8102.2	7941.91	636.23
16	8618.19	8466.23	729.44
17	9167.03	8948.61	737.53
18	8537.76	8782.72	683.4